

OPTICAL AND MAGNETIC EFFECTS ON ELECTRONIC TRANSPORT IN NANOSCALE SYSTEMS

A Dissertation

Presented to the Faculty of the Graduate School
of Cornell University

in Partial Fulfillment of the Requirements for the Degree of
Doctor of Philosophy

by

Eugenia Siu Ning Tam

January 2013

© 2013 Eugenia Siu Ning Tam

ALL RIGHTS RESERVED

OPTICAL AND MAGNETIC EFFECTS ON ELECTRONIC TRANSPORT IN
NANOSCALE SYSTEMS

Eugenia Siu Ning Tam, Ph.D.

Cornell University 2013

The understanding of the electronic properties of nanoscale systems such as a single molecule is both of fundamental interest and important for the development of applications for these units. In my doctoral research, I have developed fabrication and measurement techniques and applied them to the study of single molecule conductance and nanoscale graphene devices. Using electro-migrated breakjunctions to form nanometer-scale gaps, we measured the spin-dependent transport properties of individual N@C₆₀ endofullerene molecules and observed a spin state transition as a function of magnetic field. In another system, we used the technique of repeatedly-formed breakjunctions to determine the conductance of the on and off isomers of individual photochromic dithienylethene molecules. Finally, in this thesis I also describe our current work-in-progress related to spin current injection into graphene using nanoscale non-magnetic electrodes.

BIOGRAPHICAL SKETCH

Eugenia Tam was born in Hong Kong on December 6, 1984. From her early years she has fond memories of hot and humid weather, an obsession with playgrounds and bookstores, travelling, and fun times in primary school. In 1993, she immigrated with her parents to Markham, Ontario, Canada. Over the next nine years, it was a steady progression towards focusing on science in school; outside of academics, she played around with the piano and equestrian riding for several years. She spent a memorable and character-building summer in Sleeping Giant Provincial Park as a junior ranger in 2001. For college applications, thinking she wanted to be a vet, she applied to two life sciences programs and one engineering program. Shortly after, she realized she in fact did not like biology that much, and with this “Engineering Science” program, she could postpone specialization for another two years, so the choice was clear. The first year at the University of Toronto was full of experimentation, the second spent being a dilettante activist while managing her heaviest workload yet. Entering third year, in choosing among eight majors, she again seriously considered the bio option, but the lure of physics was too strong. Two years of physics with time spent in the labs of Professors John Wei and Amr Helmy were not quite enough, so off to Cornell she went for more, preceded by a brief stint at Professor Joshua Folk’s lab, which solidified her interest in condensed matter physics. As an Applied Physics student, she joined the group of Professor Dan Ralph to pursue research in nanoscale electronics. Outside the lab, she has found a passion for running and cycling, thanks to Ithaca’s community and convenient geography. She looks forward to running new routes in beautiful Portland, OR, where she will work as an engineer in Intel’s Portland Technology Development unit after graduation.

To my parents.

ACKNOWLEDGEMENTS

First and foremost, I would like to thank my advisor Dan Ralph for his support and guidance throughout the years. I feel very privileged to have been able to work in the Ralph group, where Dan makes every effort to allow his students to focus on the science and pursue their research interests. He is always encouraging and available for discussions. My respect for Dan as a scientist has continued to grow since my first year when I decided to join his group.

Professor Abruña adopted me as an honorary member of his group, and I have benefited so much from his mentorship, both in the matters of chemistry and in life. His wealth of knowledge never ceases to amaze me and his dedication to and enthusiasm for research is hugely inspiring. Thank you, Professor Abruña.

I am grateful to Paul McEuen for being on my committee and for his scientific guidance. His sharp insight and pure passion for beautiful things in life are inspirational.

Jacob was the first student of the Ralph group with whom I worked. Over the most part of a year, he taught me a tremendous amount about experimental physics. Jacob's generosity in helping others continues to this day, always being available to provide feedback and advice when I have questions about life and careers.

After Jacob left, Josh became my go-to person for research help in the group. His generally ebullient character, extreme breadth of knowledge and amazing memory and attention to detail made working together immensely enjoyable. One can always count on Josh to look at a complex situation and present a coherent analysis with strategic recommendations (with accent and embellishment upon request). I am deeply grateful for this friendship and for his support

through times good and bad.

Working with Wan in the past year has been a wonderful experience. Her thoughtfulness in research, skill in fabrication and great humor make her a fantastic partner to work with. I wish we had begun working together earlier.

I thank everyone in Ralph group for their help in research and for many interesting conversations. Ferdinand helped me early on in the cleanroom when I was just getting started in the group. Yongtao was a great source of distilled scientific wisdom and hilarious one-liners. Sufei was so welcoming and helpful when I was new in the group and I have had many fun chats with him in G-3 and H-5. I have a great deal of respect for Chen's dedication to physics and ability to balance work and life. Saikat taught me a lot about optics and it was always a pleasure to talk to him about life in general. Besides being the resident material science expert, Colin Heikes also provided great group gatherings at his place. Alex is the master of "fun stuff" of all kinds while being a model lab citizen. Lin provided informed insight on the latest technology and international relations. Ted was an excellent officemate and, as it turns out, a great intramurals captain, always positive and super athletic. It was also through sports that I got to know Greg, whose "gentle encouragement" in soccer and in running I truly appreciate, as well as his passion for and knowledge of music, food, and drink. I am happy to have been labmates with Taka, Dave, Jen, Peter and Colin Jermain and I wish them all the best.

The members of the Abruña have generously given me their time and assistance. I have learned much from this talented group of chemists. Many thanks to Yu-Wu, Mitk'El, Joaquin, Joanna, Nikki, Hualei, Sean and Michelle.

A big thank you to Eric Smith, Nate Ellis, Jon Shu, Steve Kriske and the staff of CCMR and CNF, who have provided valuable technical help and made my

life much easier.

I would like to thank others in the physical science complex for fruitful discussions: Praveen, Arend, Rob Barton, Chi-Feng, Jonathan Alden, Nathan Gabor, Isaac Storch, Hsin-wei and Luqiao. Outside Cornell, I am grateful to our collaborators and others for their helpful scientific advice: Will Shum, Garnet Chan, the Venkataraman group, Weitao Yang and Xiao Zheng.

Thanks to Laura and Darryl for fantastic times on and off campus. Some of the most memorable elements of the past two years have been with you guys, often revolving around our common interest in things like cycling, trail running, the outdoors, food (by which I mean chips) and wine. Brian has been a great friend since first year, and I thank him for always being there for me. Our trip to Glacier was amazing. I thank Will Yuen for being one of my closest friends and a mentor in many parts of life. Special thanks to Jun for being by my side in the last few months while I wrote and prepared for my defense.

Finally, my sincerest thanks to my parents for their love and support, without which I would be nothing.

TABLE OF CONTENTS

1	Introduction	1
1.1	Perspective	1
1.1.1	Molecular electronics	2
1.1.2	Spintronics	6
1.2	Overview of this thesis	7
2	Single molecule transistors	9
2.1	Introduction	9
2.2	Spectroscopy by SET	10
2.2.1	Relevant energy scales	11
2.2.2	Coulomb blockade in the sequential-tunneling regime	13
2.2.3	Co-tunneling	18
2.2.4	Coherent tunneling	20
2.3	Device fabrication	21
2.3.1	The trouble with Pt	24
2.3.2	Device preparation for measurement	26
2.4	Break-junctions, 2012 edition	27
2.5	Electromigration	30
2.6	Measurement techniques	31
2.7	Control samples	33
2.8	Summary	33
3	Magnetic effects on the electronic properties of N@C₆₀	34
3.1	Scope of this chapter	34
3.2	Introduction	34
3.3	The endofullerene N@C ₆₀	36
3.4	Theoretical background	38
3.5	Results and discussion	39
3.5.1	Charge state	42
3.5.2	Comparison to calculations	44
3.6	Conclusion and further developments elsewhere	49
3.6.1	Cotunneling in N@C ₆₀	50
3.6.2	Quantum phase transition in C ₆₀	50
3.6.3	Electronic read-out of the nuclear spin of an SMM	52
4	Statistical measurements of single molecule conductance	54
4.1	Introduction	54
4.2	Conductance of atomic-sized contacts	55
4.2.1	Length scales — bulk, mesoscopic, nanoscale	55
4.2.2	Quantum transport — the scattering approach	57
4.3	Transport through single molecules	59

4.3.1	Physical understanding	59
4.3.2	Theoretical efforts	62
4.4	The “sewing machine”	64
4.4.1	First version	65
4.4.2	Upgraded version	65
4.5	Sample preparation	67
4.6	The measurement	67
4.7	Capability check	70
4.8	Optical switch molecules – dithienylethenes	75
4.8.1	Introduction	75
4.8.2	Sample preparation	77
4.8.3	One-dimensional histograms	79
4.8.4	Comparison to past results	83
4.8.5	Two-dimensional histograms	84
4.8.6	Total-displacement histograms	87
4.8.7	Comparison to theory	89
4.9	Summary of the sewing machine experiments	92
5	Spin Injection in Graphene by the Spin Hall Effect	94
5.1	Introduction	94
5.2	Graphene	94
5.2.1	Graphene in spintronics	96
5.3	Spin Hall effect	100
5.4	Device geometry	103
5.5	Device Fabrication	106
5.5.1	Graphene growth and processing	106
5.5.2	Lithography steps	108
5.6	Results to-date	110
5.7	Next steps	116
A	JEOL6300 script for break-junction fabrication	117
	Bibliography	119

LIST OF FIGURES

1.1	Examples of past work in molecular electronics: modified-AFM, mechanical break-junction, STM.	2
1.2	Statistical measurements of single molecule conductance. Figures from literature.	5
1.3	Roots of spintronics — Giant magnetoresistance	7
2.1	Energy levels of an SET. Experimental data from Park <i>et al.</i>	10
2.2	Interpretation of dI/dV vs. bias and gate voltages, adapted from Pasupathy's thesis. Schematic of SET "circuit."	14
2.3	Energy level diagrams with excited states and the corresponding interpretation of dI/dV characteristics.	17
2.4	Cotunneling — figures from De Franceschi <i>et al.</i> with energy level diagrams and dI/dV data as a function of bias and gate voltages.	19
2.5	Picture and SEM image of a break-junction.	21
2.6	SEM images of PMMA/copolymer bilayer resist profile with and without methanol dip after development.	24
2.7	Optical and SEM images of actual devices — electrode cluster, electromigrated break-junction, wire-bonded chip, whole wafer.	25
2.8	SEM image of break-junction with PbSe nanocrystals.	27
2.9	Electrode design for electromigrated break-junctions. Images from mask CAD file.	28
2.10	SEM images of good and bad metal lift-off.	29
2.11	Current-voltage trace of electromigration of an Au wire with feedback.	31
2.12	Current as a function of gate voltage at a fixed source-drain voltage, $V_{sd} = 5$ mV for an N@C ₆₀ device.	32
3.1	Molecular structure diagram and spin states of N@C ₆₀ and its anions.	36
3.2	SEM image of an electromigrated breakjunction from one of the chips we used in the experiments described in this chapter	36
3.3	Conductance as a function of bias voltage and gate voltage for two N@C ₆₀ devices and one control C ₆₀ device.	40
3.4	Conductance as a function of bias voltage and magnetic field for two N@C ₆₀ devices and one control C ₆₀ device.	41
3.5	Spin states for 3 possible charge couplets of N@C ₆₀ . Energy levels of spin multiplets as a function of magnetic field.	42
3.6	Numerical calculations by Dr. Carsten Timm to qualitatively reproduce experimental dI/dV data and the energy levels incorporated in the theoretical model showing the ground state and ETE transitions observed.	45

3.7	Effect of linewidth on peak resolution; comparison between experiment and calculation.	49
3.8	Figures from Roch <i>et al.</i> for N@C ₆₀ . dI/dV in the weakly-coupled regime and in the cotunneling regime.	51
4.1	Illustration of a molecular junction with diamine linker group.	60
4.2	The tip holder and the Nano-HSZ stage mounted on an aluminum base.	66
4.3	Pictorial representation of each measurement cycle	68
4.4	Conductance histogram of bare Au contacts. Inset: Sample traces, as a function of electrode displacement.	70
4.5	Conductance histograms for several diaminoalkanes. Conductance as a function of carbon chain length.	72
4.6	Conductance histograms for (a) 4,4'-bipyridine and (b) 1,2-bis(4-pyridyl)ethane.	73
4.7	Two-dimensional histogram for 4,4-bipyridine.	74
4.8	Molecular structure and UV-vis absorbance of our dithienylethene molecules.	78
4.9	Conductance histograms and sample traces for molecules 1o/c and 2o/c	80
4.10	Examples of individual conductance traces measured for the molecule species as labeled.	82
4.11	Comparison of logarithmically-binned (in conductance) 2-dimensional histograms for bare Au junctions in pure solvent, 1o and 1c	85
4.12	Histograms showing the distributions of the total displacement distance Δd for Au, 1o and 1c junctions.	87
4.13	Conductance as a function of junction geometry obtained by density functional calculations on 182 relaxed molecular junctions for 1o and 1c , with pictorial renditions of examples of molecular junctions generated from the calculations.	90
4.14	Simplified molecule-junction configuration used for geometry optimization.	91
5.1	Graphene: Dirac cone $E(k)$, lattice structure; quantum Hall effect, gate-dependence of resistance, carrier density and mobility from literature.	95
5.2	Non-local spin injection and spin detection geometry.	99
5.3	Non-local resistance measurements of spin transport in graphene, from literature.	100
5.4	Illustrations of spin Hall effect, from J. E. Hirsch, 1999.	101
5.5	Device concept and chemical potential diagram for spin injection into graphene by spin Hall effect.	104
5.6	ISHE detection scheme.	105

5.7	Raman spectra and optical image of transferred CVD graphene on SiO ₂ /Si substrate.	107
5.8	Graphene growth and transfer process steps.	107
5.9	Outline of steps in the fabrication process.	108
5.10	Device design and an optical image of one particular device that we measured.	111
5.11	Measurement configuration for the data shown in Figs. 5.12 and 5.13, respectively.	113
5.12	Magneto-resistance measurement for Py-graphene-Pt, for different temperatures.	114
5.13	Non-local voltage measurement as a function of field for the configuration shown in Fig. 5.11b.	115

CHAPTER 1

INTRODUCTION

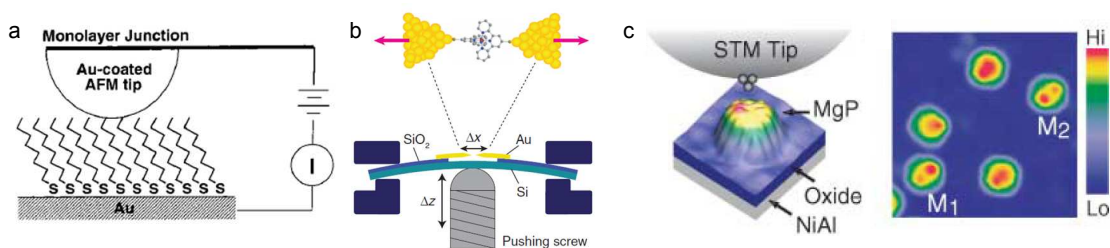
1.1 Perspective

As industry continues to improve techniques to reliably manufacture smaller and faster components and to find ways to overcome obstacles of scaling down (stability, heat, *etc.*), one can imagine, as the ultimate limit for a well-defined component, a single molecule junction. The ability to precisely design a molecule leads to various possible functionalities, such as gate voltage control, optical activity, and magnetic response. Molecular components can conceivably be far cheaper to produce from a bottom-up approach. Nevertheless, the challenges to realizing this vision are numerous and complex. While this goal of functional electronics based on molecules motivates our research at the nanoscale, we are also interested in furthering the understanding of the physics in these highly quantum mechanical systems. My doctoral work has largely focused on the electronic transport through single molecules and its dependence on external “knobs” such as applied bias, optical excitation and magnetic field. This interest in magnetic properties of nanoscale systems has also brought me to investigating the spin transport properties of graphene. Due to the rather diverse range of topics included in this thesis, I intend in this chapter to highlight some of the past work in molecular electronics and spintronics that are examples of research that has led to the projects described in this thesis.

1.1.1 Molecular electronics

Since the proposal of a molecular rectifier in 1974 by Aviram and Ratner [1], there has been a great deal of progress in our understanding of the transport properties through single molecules, although the realization of useful circuitry involving single molecule junctions is still arguably a distant goal. One fundamental difficulty is in the uncertainty of the junction geometry. The progress in nanoscale research has led to atomic resolution being now commonly achievable in well-designed scanned probe experiments, allowing direct probing of single molecules. On the other hand, some research has chosen to focus on studying distinctive molecular characteristics without requiring atomic-level control or on performing statistical measurements. In the following, I briefly discuss several areas of research in molecular electronics.

Figure 1.1: a) From Wold and Frisbie [2], measuring conductance of self-assembled organic monolayers with a c-AFM. b) From Parks *et al.* [3], measurement of $S = 1$ Kondo effect in a Co complex as a function of stretching. c) From Wu *et al.* [4], STM of Mg porphine molecules with laser excitation.



Scanned probe experiments

Scanned probe techniques that have been used to study the electronic properties of molecules include scanning tunneling microscopy (STM) and atomic force microscopy (AFM). Operated in high vacuum, STM offers atomic-level spatial

resolution and an unparalleled degree of control in probing the transport characteristics of single atoms and molecules [5]. Pioneering work by Wilson Ho *et al.* showed the ability to locate a single molecule on a surface and probe its vibrational excitations [6]. Such STM measurements, a two-probe technique, have been combined with optical excitation/gating (Fig. 1.1c) and external magnetic field [4,7] to study the conductance dependence on these parameters.

In atomic force microscopy (AFM) also, strikingly high resolution has been achieved by functionalizing the tip with a chemically well-defined termination, such as a single CO molecule [8] — Gross *et al.* were able to image the individual atoms of a pentacene molecule. In fact, comparing the STM and AFM images on the same system (individual pentacene molecules on a metallic Cu(111) substrate), we see that AFM imaging offers superior resolution on conducting substrates because the electronic wavefunction of the molecules is coupled (and therefore smeared) too strongly to the substrate for transport-based imaging. Transport measurements can be made with an AFM as well, in the conducting-AFM (c-AFM) configuration. A popular type of measurement for both STM and c-AFM in molecular electronics is to embed the molecule species of interest (a semiconductor or molecular wire) in an otherwise insulating self-assembled monolayer (SAM) [2,9]. Figure 1.1a shows an illustration from one of the earliest such measurements on thiol-terminated alkyl molecules.

Single molecule transistors

By adding a third terminal — a gate electrode — to the measurement of single molecule conductance, we get what is essentially a transistor geometry. To exhibit transistor-like on/off states, the molecule must have a gap, which is

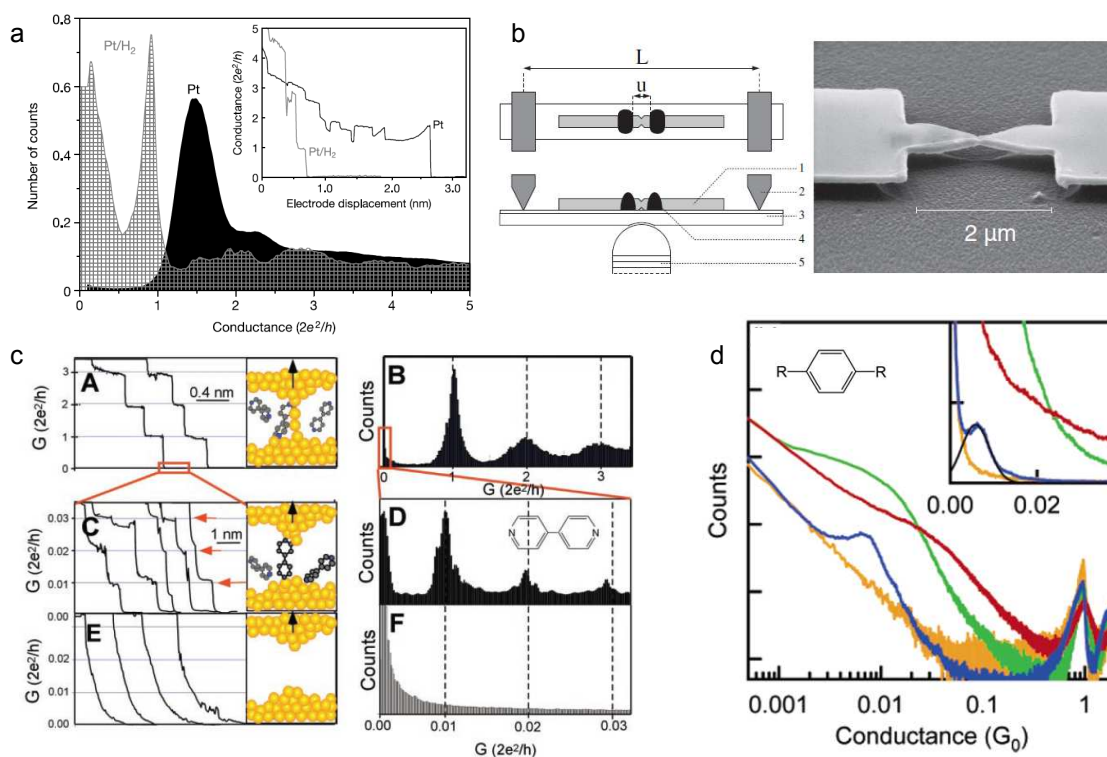
a requirement that is not difficult to satisfy in organic molecules. A room-temperature transistor was fabricated by contacting a single semiconducting nanotube with three terminals which demonstrated gate-tunable on-off states [10]. Going further into molecular regime, much more interesting physics can be accessed when the molecule not only has a gap in the density of states, but also maintains its discrete energy levels, which requires weak hybridization with the metallic electrodes. A single molecule transistor with discrete charge states was realized in 2000 by Park *et al.* using electromigrated break-junctions to contact individual C₆₀ molecules [11], where they observed mechanical oscillations in the conductance spectra. The SMT is a very useful tool to study the low-energy characteristics of single molecules and is discussed in more detail in Chapters 2 and 3 [3, 12].

Statistical measurements

Given the range and uncertainty in the geometry of single molecule junctions, an obvious strategy to study such systems is to make statistical measurements by sampling a large number of geometries. This can be achieved by, for example, adapting one of two aforementioned techniques — scanned probe (STM or c-AFM) and mechanically-controllable break-junctions (Figs. 1.2a,b) [13–15]. In experiments with vacuum capabilities and careful cleaning of the surfaces, one can introduce the molecules either by deposition onto the surface or in gas phase and form molecular junctions by repeatedly opening and closing the junction gap [16]. In ambient conditions, the first demonstration of measuring single molecule conductance without complicated substrate assembly (*e.g.*, self-assembled molecular monolayers, nanoparticle layers) was by Xu and Tao, who

made repeated Au junctions immersed in solutions of dithiol-alkanes and 4,4'-bipyridine (Fig. 1.2c) [17]. Recent work by Venkataraman *et al.* has made it possible to perform such measurements without trace selection by careful choice of endgroups (Fig. 1.2d) and to also measure properties such as I - V , thermo-power, and force [18–20].

Figure 1.2: Examples of statistical measurement of single molecule conductance. a) Conductance histograms from Ref. [15], measured using mechanically-controlled break-junctions (see (b)) with clean Pt (solid black) and Pt in H_2 atmosphere (hatched). b) Illustration and SEM image showing the structure of a mechanically-controllable break-junction setup, from Ref. [16]. c) Conductance traces and histograms from Ref. [17], measured using repeatedly-formed break-junctions in a solution of 4,4'-bipyridine. Top row shows Au contacts, middle row shows molecular junctions, and bottom row is without molecules. d) Conductance histograms from Ref. [21], measured with repeatedly-formed break-junctions in solutions of benzene-based molecules. Yellow: no endgroup. Red: R = SH. Green: R = CN. Blue: R = NH_2 . Inset is the same data on a linear scale.

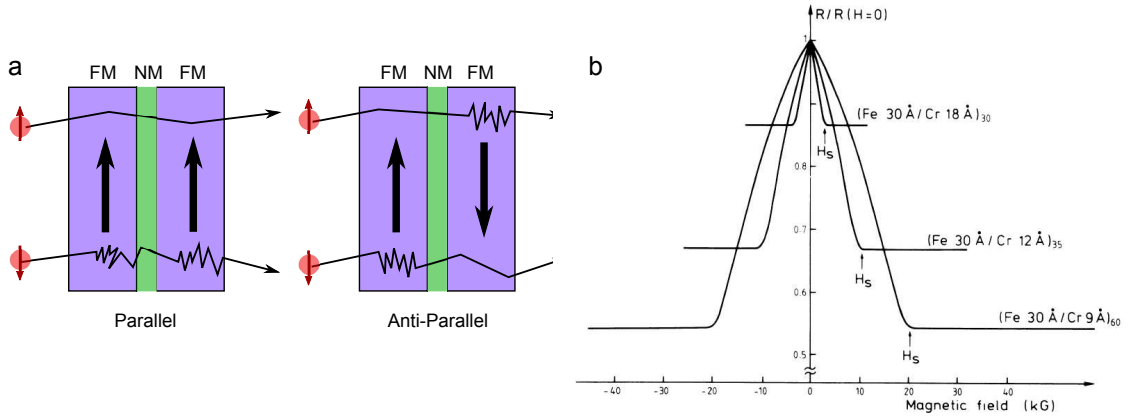


1.1.2 Spintronics

Since two chapters of this thesis deal with spin-related electronic transport properties (Chapter 3 on N@C₆₀ and Chapter 5 on graphene), I feel that it is necessary to place the work of my research in the very broad field of spintronics, the study of the spin degrees of freedom and their interaction with electronic properties. The field of spintronics traces its roots to the 1980s from the discovery of spin-polarized current injection, magnetoresistance, and, of course, the giant magnetoresistance effect (Fig. 1.3) which enabled the development of magnetic hard drives and led to a Nobel prize for Albert Fert and Peter Grünberg [22–24]. This area of research has always been closely linked to computing technology, in particular for faster and more compact and efficient storage/memory devices. Longer-term goals include next-generation logic devices, such as the so-called spin transistor or spin-FET, a configuration of which was first suggested by Datta and Das in 1990 [25]. For all of these goals, insight into spin generation and transport and the interaction between spin and electrical signals is central.

Here, we have explored two very specific topics under the umbrella of spintronics — spin-state-dependent transport characteristics of a single molecule and the injection of spin current into graphene *via* the spin Hall effect. Much of the motivation for the study of single atom and single molecule spins, other than for fundamental interest in this purely quantum mechanical property [26, 27], comes from their potential use in quantum computation [28, 29]. The intrinsic large anisotropy that can be engineered into molecules (or clusters of atoms) allow molecular magnets to maintain their magnetization over relatively long time-scales, much longer than the time needed to manipulate or read the spin state [30, 31]. The low spin-orbit coupling in carbon-based materials that leads to

Figure 1.3: Giant magnetoresistance. a) A simple picture of the path (thin black lines) of an electron of each spin (small red arrows) through ferromagnetic (FM) films aligned parallel or anti-parallel, separated by a non-magnetic (NM) layer. The amount of zig-zagging represents the amount of scattering experienced by the electron. b) Experimental data from Baibich *et al.* (Ref. [24]) showing magnetoresistance of three Fe/Cr multi-layer structures at 4.2 K, with field applied along the direction of the current.



long spin relaxation times in organic molecules is also the reason for slow spin relaxation in graphene and, to a lesser extent, carbon nanotubes [32–34]. Along with other well-known electronic properties of graphene — high mobility, gate-tunability — this makes graphene a promising material as a spin-conserving medium. We will explore this further in Chapter 5 of this thesis.

1.2 Overview of this thesis

In Chapter 2, I discuss the basic theory necessary to understand electronic transport through single electron transistors. I also describe the fabrication procedure to make electromigrated break-junctions and the measurement techniques we employ to identify devices of interest and to resolve fine electronic structure in conductance measurements. This sets the stage for Chapter 3, in which

I describe our observation of spin excitations and a spin state transition in individual endofullerene N@C₆₀ molecules.

Continuing with the theme of single molecule electronics but moving to room temperature, in Chapter 4 I first focus on the design and construction of a repeatedly-formed break-junction setup (the “sewing machine”) to statistically measure single molecule conductance in solution under ambient conditions. The second half of this chapter is devoted to the discussion of our experiment on the optically-switchable dithienylethene molecule.

Finally, in Chapter 5, I turn to my most recent work in partnership with Wan Li on spin injection into graphene, which is currently still in progress at the time of this writing. I first discuss our motivation for investigating graphene for spintronics, then describe the fabrication process, measurement scheme and progress. I end by presenting some preliminary results and a projection of the next steps.

CHAPTER 2
SINGLE MOLECULE TRANSISTORS

2.1 Introduction

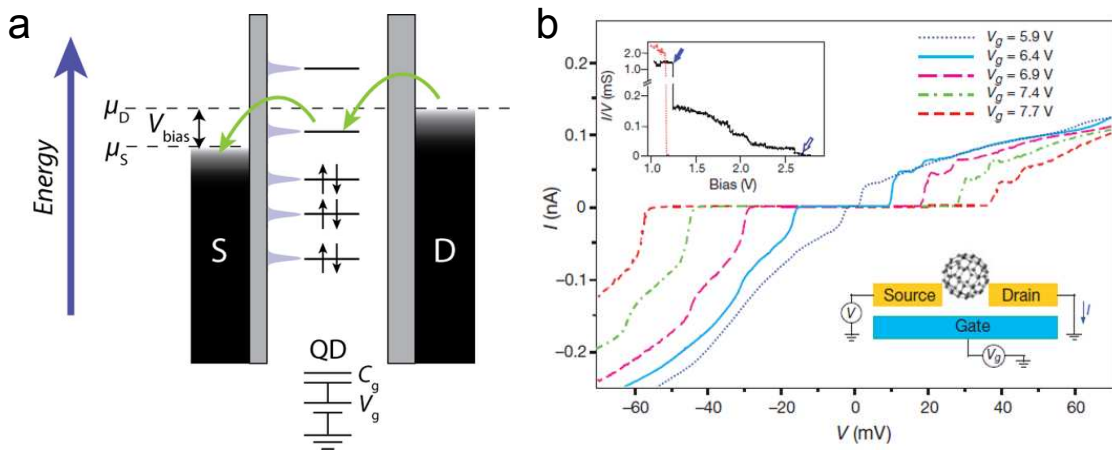
This chapter will describe the fundamentals of single molecule transistors (SMTs) as background for the experiments discussed in the next chapter on $N@C_{60}$. I will first develop a basic theoretical understanding of transport through a quantum dot coupled to source and drain electrodes and a gate, focusing on the sequential-tunneling regime but also touching on the cotunneling and coherent tunneling regime. For further reading, there exist many excellent references, from basic [35] to intermediate [36] to somewhat more advanced [37]. I will then describe the fabrication and measurement techniques we employ in our work to achieve sufficient yield and signal quality to study the phenomena of interest. Much of the discussion in this chapter follows from corresponding chapters in the theses of Jacob Grose and Abhay Pasupathy [38, 39].

The SMT can be considered to be one specific type of a single-electron transistor (SET). The SET consists of a pool of electrons confined to a very small volume — an “island” — connected to electrodes (reservoirs of electrons) *via* tunnel connections, where transport of the *on* state involves the tunneling of a single electron on and off the island when the energy requirements are satisfied. The *on* state of the SET corresponds to when both the N -electron and $N + 1$ -electron states of the island are energetically accessible. This behaviour is purely quantum mechanical and, at low temperatures, can depend strongly on the energy states of the electrode-island-electrode system. The SMT is a special case of an SET where the island is a single molecule. This approaches the lower

limit for the size of an electronic island.

The SET was first physically realized in an all-metallic structure in 1987 when Fulton and Dolan observed conductance oscillations in their device [40]. Efforts intensified from the early 1990s, when fabrication and material growth techniques became sophisticated enough to allow one to confine electrons in volumes of on the order of 100 nm in lateral dimensions to first observe the characteristics of energy quantization [41,42]. As the size of the dot is decreased, the charging energy increases, giving a larger temperature and energy window to measure the low-energy phenomena of the system, such as the nanomechanical oscillations in a single fullerene C_{60} molecule [11].

Figure 2.1: a) Energy levels in a quantum dot coupled to source, drain, and gate electrodes. b) Experimental data from Park *et al.* (Ref. [11]) showing Coulomb-blockaded regions in the I - V curve for a C_{60} single SMT.



2.2 Spectroscopy by SET

In general, a single-electron transistor (SET) consists of a quantum dot or localized island of electrons — such as a nanoparticle, a molecule, or a gate-confined area of a two-dimensional electron-gas (2DEG) — tunnel-coupled to source and

drain electrodes that act as electron reservoirs (Fig. 2.1). The energy levels of the quantum dot can be tuned by a capacitively-coupled gate electrode to precisely control the number of electrons on the island, provided the thermal energy is not greater than the relevant energy spacings of the system. Because the conductance of such junctions are highly dependent on the relative alignment of the energy levels of the quantum dot and the Fermi levels of the electrodes, measuring the conductance of the dot while tuning parameters such as bias and gate voltages and magnetic field allows one to effectively perform electronic spectroscopy.

2.2.1 Relevant energy scales

We want to understand how the measured transport characteristics relate to the properties of the quantum dot and the entire junction. Naturally, we have to consider (1) the energy required for tunneling to occur through the junction, and (2) the sources of energy that may overcome (1).

We first look at the energy associated with quantum confinement. We can get an order-of-magnitude approximation from the expression for the energy level spacing, E_n , for a particle-in-a-box (of dimension a) model:

$$E_n = \frac{\hbar^2}{2m_e} \left(\frac{\pi}{a}\right)^2.$$

For a typical small organic molecule, assuming 1 nm for all dimensions, this yields an energy scale of about 0.4 eV. For metallic nanoparticles, the particle-in-a-box expression is often a good approximation for the intrinsic energy levels. However in molecules, the actual energy levels are determined by the molecular orbitals. The most important orbitals to consider for electronic transport are the

highest occupied molecular orbital (HOMO) and the lowest unoccupied molecular orbital (LUMO). We will denote the HOMO-LUMO gap energy as ΔE .

Another energy scale that becomes significant as we move down to nanoscale objects is the charging energy E_C for a single electron, related to the total capacitance C of the quantum dot:

$$E_C = \frac{e^2}{2C}.$$

For a quantum dot coupled to source/drain electrodes and a gate, $C = C_s + C_d + C_g$, where the terms are the contributions from the respective electrodes (Fig. 2.2b). The smaller the capacitance, the larger E_C — the smallest capacitance can be approximated as the self capacitance of a conducting sphere of radius R , $C = 4\pi\epsilon_0 R$. For $R = 1$ nm, $C \approx 1 \times 10^{-19}$ F, translating to a charging energy of 0.7 eV. For reference, for ~ 10 nm metal nanoparticles trapped in electromigrated break-junctions, capacitances on the order of 1 aF have been measured for C_s , C_d , and C_g [43].

The thermal energy is $k_B T$, which is about 25.9 meV at room temperature (300 K), and about 10 μ eV at base electron temperature in the dilution fridge (100 mK). It follows that for small molecules and very small quantum dots, the thermal energy even at room temperature is well below typical energy gaps. Another energy scale that contributes to broadening of the energy levels is the coupling to electrodes, characterized by the tunneling time constants τ_s and τ_d , for the source and drain, respectively. The corresponding energy for the effect of both electrodes is

$$\Gamma = \hbar \left(\frac{1}{\tau_s} + \frac{1}{\tau_d} \right).$$

To be able to resolve energy levels of the quantum dot-electrodes system requires that $\Delta E > k_B T, \Gamma$. In practice, T much lower than this requirement is

desired for better resolution and junction stability.

2.2.2 Coulomb blockade in the sequential-tunneling regime

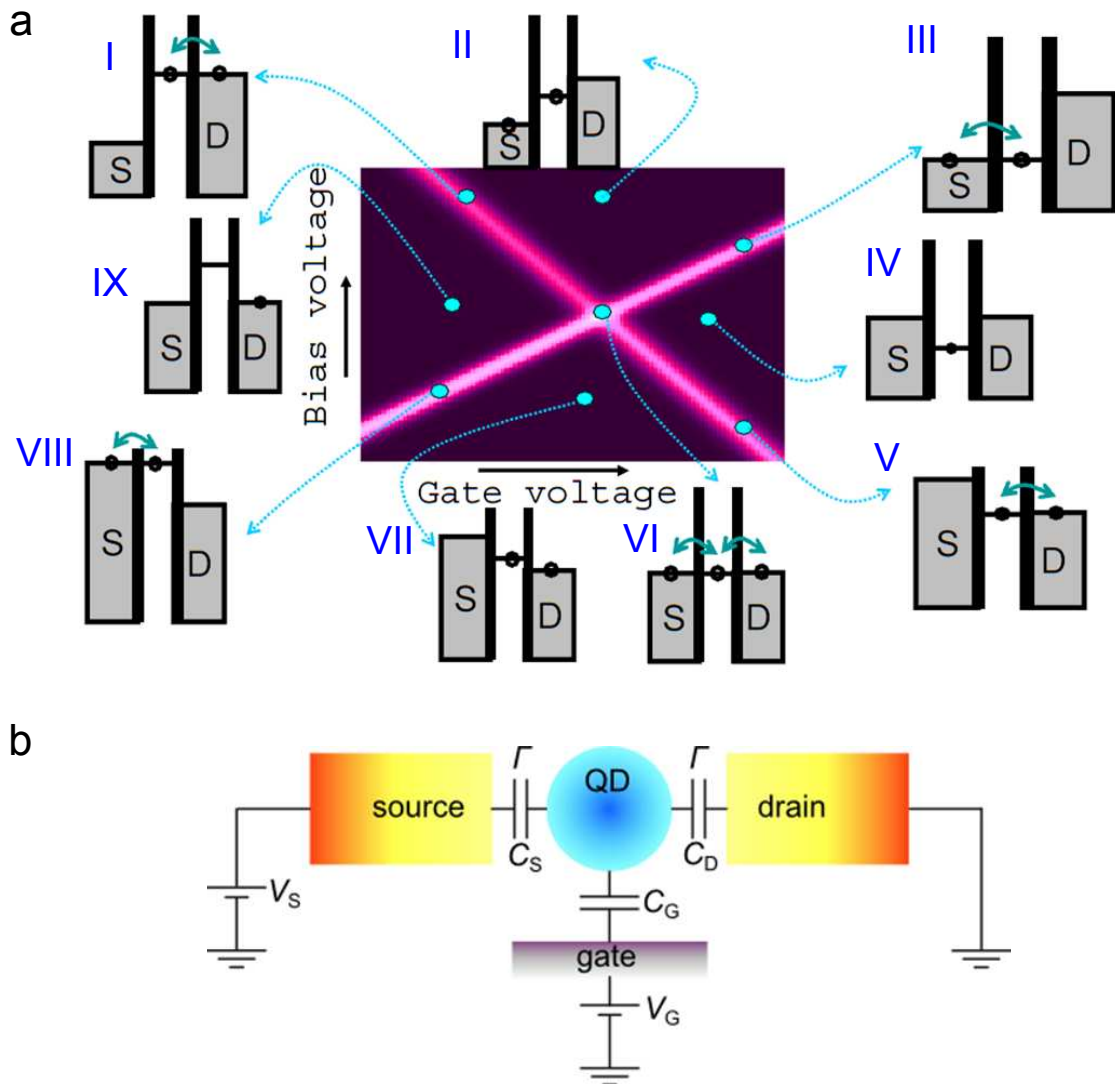
In the sequential-tunneling regime, the quantum dot alternates between two charge states as electrons hop on and off. The relevant energy in this picture is the energy of an additional electron to the N electrons already on the dot, which is the electrochemical potential μ_{N+1} , calculated as the difference between the total energy of the states with $N + 1$ and N electrons: $\mu_{N+1} \equiv U_{N+1} - U_N$. The electrochemical potential of the quantum dot in a junction may have several significant contributions, namely the intrinsic energy levels, the charging energy, and the capacitive energy associated with the voltages applied at the gate and at the electrodes. By definition, when a quantum dot is connected to two electrodes at zero bias, with chemical potentials $\mu_s = \mu_d$, the electronic states of the dot will be filled to N such that $\mu_N \leq \mu_s \leq \mu_{N+1}$.

Starting from $\mu_s = \mu_d = \mu_N$, to access the $N + 1$ -electron state, the energy tuning (either by the source/drain or the gate) required is the energy difference between electrochemical potentials

$$\mu_{N+1} - \mu_N = E_C(N) + \Delta E(N).$$

As V_g is tuned, the electrochemical potential of the quantum dot is changed with respect to $\mu_{s,d}$. When $\mu_{N+1} = \mu_{s,d}$ for some electron number N , the two charge states N and $N + 1$ become both accessible (see Fig. 2.2a-VI). This is a *degeneracy point* V_0 , a gate voltage at which current can flow at zero bias voltage. At higher and lower gate voltages (IV and IX), current is blocked at zero bias — this is referred to as the Coulomb blockade. Now we consider non-zero bias

Figure 2.2: a) From Pasupathy's thesis [39]. Energy level diagrams showing possible alignments of the chemical potentials of the electrodes and a single-level quantum dot and the corresponding regions in the dI/dV map as a function of bias and gate voltages. The black line in the center of each energy level diagram represents μ_{N+1} for some N . The Roman numeral labels are for identification in the text only and not in any particular order. b) Schematic of a typical SET "circuit."



— at degeneracy point, clearly current can still flow through the single level as depicted in II and VII. Away from the degeneracy point, if the bias shifts the Fermi level of an electrode such that μ_{N+1} falls between the Fermi levels of the electrodes, as shown in I, III, V, and VIII, then current can once again flow. It should be clear that as V_g is tuned further from the degeneracy point, a higher bias is required to make μ_{N+1} accessible.

Let us derive the precise relationship between V_g and V_s (assume $V_d = 0$) of the dI/dV peaks at the edge of the Coulomb blockaded regions near a degeneracy point V_0 . The charge on the dot Ne at potential V can be written:

$$Ne = C_s(V - V_s) + C_d(V - V_d) + C_g(V - V_g),$$

so that V can be written

$$V = \frac{Ne}{C} + \frac{V_s C_s}{C} + \frac{V_d C_d}{C} + \frac{V_g C_g}{C}.$$

Let us define the potential on the dot to be 0 when there are N electrons, at zero bias and when the gate voltage is at the degeneracy point V_0 , such that $V_0 = -Ne/C_g$. Now for one edge of the Coulomb diamond, we have energetic equivalence between having an electron on the source electrode and having an electron on the dot:

$$eV_s = eV = \frac{-eV_0 C_g}{C} + \frac{eV_s C_s}{C} + \frac{eV_g C_g}{C},$$

while at the other edge, for energetic equivalence between having an additional electron on the drain electrode and having it on the dot, we require (recall: $V_d = 0$)

$$0 = eV = \frac{-eV_0 C_g}{C} + \frac{eV_s C_s}{C} + \frac{eV_g C_g}{C}.$$

So from the last two equations, we obtain:

$$V_s = -\frac{C_g}{C_s}(V_g - V_0)$$

and

$$V_s = \frac{C_g}{C_g + C_d}(V_g - V_0).$$

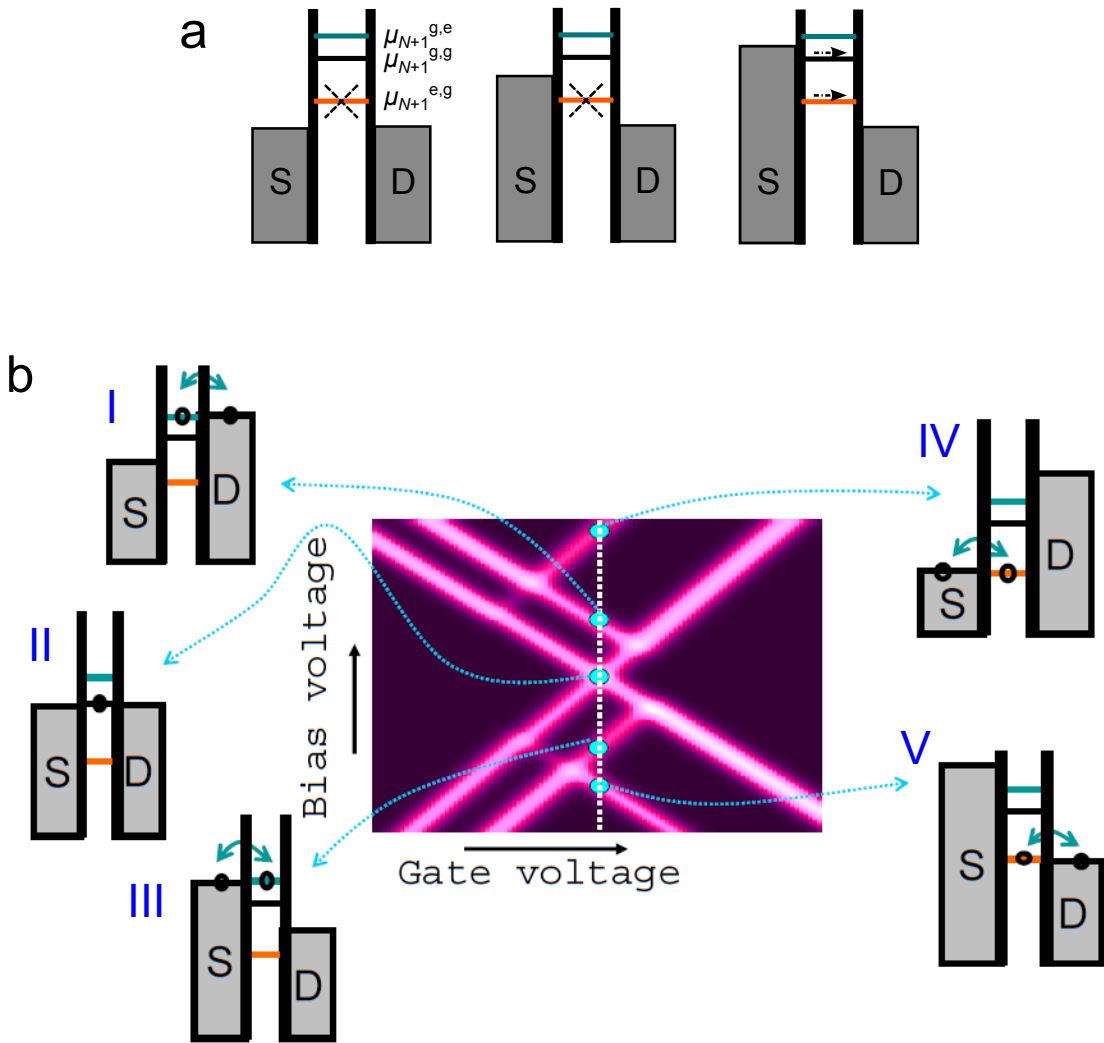
Thus, the slopes of the edges of the Coulomb diamonds for a quantum dot are determined by the capacitances C_s , C_d , and C_g .

Excited states in the dI/dV

Next, consider the case where, instead of having only the ground state of each charge state (N and $N+1$ here), there exist excited states at energies accessible by a bias voltage. These low-energy excitations could arise from internal vibrational modes, center-of-mass oscillations, and magnetic excitations. The influence of these excited states on the dI/dV is critical to our discussion of spin excitations in the next chapter. Figure 2.3a illustrates possible scenarios for the alignment of the energy levels of the electrodes and the quantum dot, where we have now labeled μ_{N+1} as μ_{N+1}^{g-g} to denote ground-state-to-ground-state and included μ_{N+1}^{e-g} (μ_{N+1}^{g-e}), which corresponds to transition from the N -electron excited (ground) state to the $N+1$ -electron ground (excited) state.

Tunneling transitions involving excited states appear in dI/dV maps (*vs.* bias and gate voltages) as additional lines, parallel to the edges of the Coulomb diamond and not extending into the blockaded region (Fig. 2.3b). That the excited state peaks are confined to the regions outside the Coulomb diamonds reflects the requirement that the μ_{N+1}^{g-g} must fall within the bias window for the excited state transitions to be allowed. Otherwise, the dot will settle into the ground state of the only energetically allowed charge state. When the excited states are accessible, it is easy to see that their dependence on bias and gate voltages will be similar to that for μ_{N+1}^{g-g} , assuming that the excited states do not somehow have

Figure 2.3: a) Energy level diagrams showing that transport is blocked until the ground-state-to-ground-state transition falls within the bias window, because otherwise the charge state of the dot is fixed and neither of the excited state transitions are accessible. The blue (orange) line is an excited state of the $N+1$ (N) charge state. b) Adapted from Pasupathy's thesis [39]. Energy level diagrams showing the electrochemical potentials of the source, drain, and quantum dot at different points in the dI/dV vs V_s, V_g color-scale map.



significantly different capacitances.

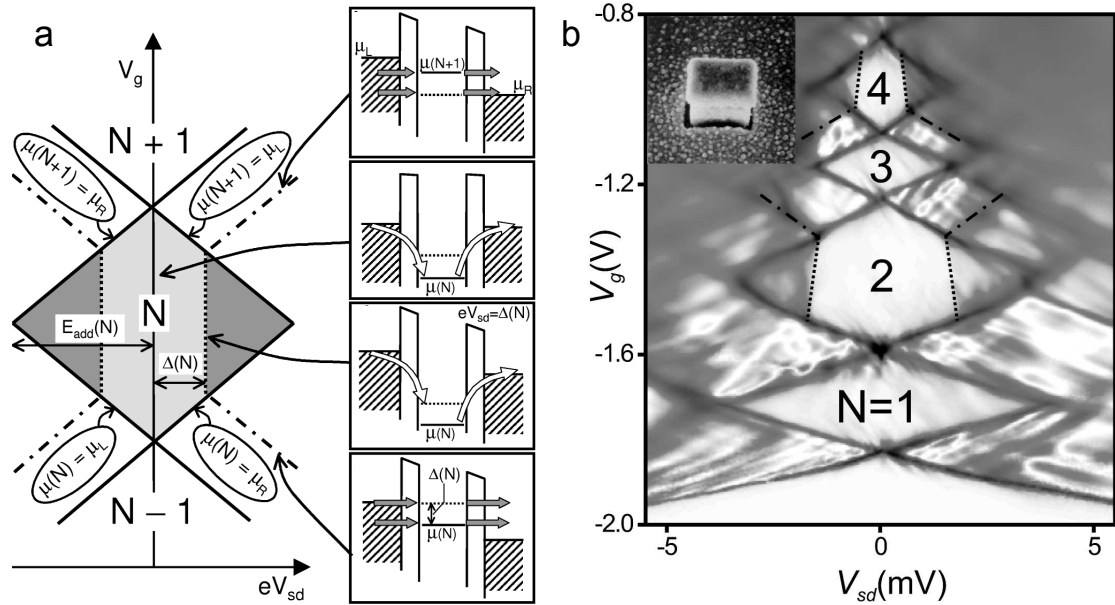
The onset of increased tunneling due to each excited state is, therefore, a way to directly probe the energies of excitations in a quantum dot-electrode system. Our ability to resolve such resonances is again limited by the broadening introduced by thermal energy and dot-electrode coupling.

2.2.3 Co-tunneling

In contrast to sequential-tunneling, which requires energetic degeneracy between two charge states, transport can also within a single charge state *via* higher-order processes involving simultaneous tunneling of two or more electrons, known as cotunneling. While this is not studied in my work described in this thesis, it is of sufficient interest in this area of research that I will describe this regime briefly in this section. Cotunneling is more dominant in junctions where the quantum dot is more strongly coupled to the electrodes, where tunneling rates are higher. Much of the interest in studying the cotunneling regime is due to the fact that one can also study the energies of excited states from the conductance data.

The cotunneling dI/dV characteristics can be understood by looking at the energy level diagrams in Fig. 2.4a. In particular, the second and third panel from the top depict cotunneling in the elastic and inelastic regimes, respectively. When the bias voltage is less than the excitation energy, cotunneling occurs by having electrons tunnel simultaneously into and out of the dot to the ground state level, preserving the charge and remaining in the ground state in the process — this is elastic cotunneling. When the bias reaches the excitation energy,

Figure 2.4: Both panels from De Franceschi *et al.* [44]. a) Energy level diagrams corresponding to different regimes of conductance. Top and bottom diagrams (with grey arrows) are in the first-order tunneling regime as discussed in the previous section, while the middle two diagrams (with white arrows) correspond to cotunneling. b) Experimental data on a semiconductor quantum dot, showing cotunneling features in the even-numbered Coulomb diamonds.



inelastic tunneling can occur, which leaves the dot temporarily in an excited state. This shows up as a sharp increase in conductance at the excitation energies (vertical dotted lines in Fig. 2.4a) when such excitations exist at energies less than the addition energy of the dot. Thus, cotunneling is another regime in which the energy levels of a quantum dot can be studied. An early demonstration of the measurement of cotunneling is shown in Fig. 2.4b, in work by De Franceschi *et al.* [44], performed on a fabricated semiconductor quantum dot of with dimensions of 450-600 nm. At the end of Chapter 3, I will describe the results of Roch *et al.* [45] in the cotunneling regime on $N@C_{60}$ which corroborate the conclusions we draw from measurements in the sequential-tunneling regime.

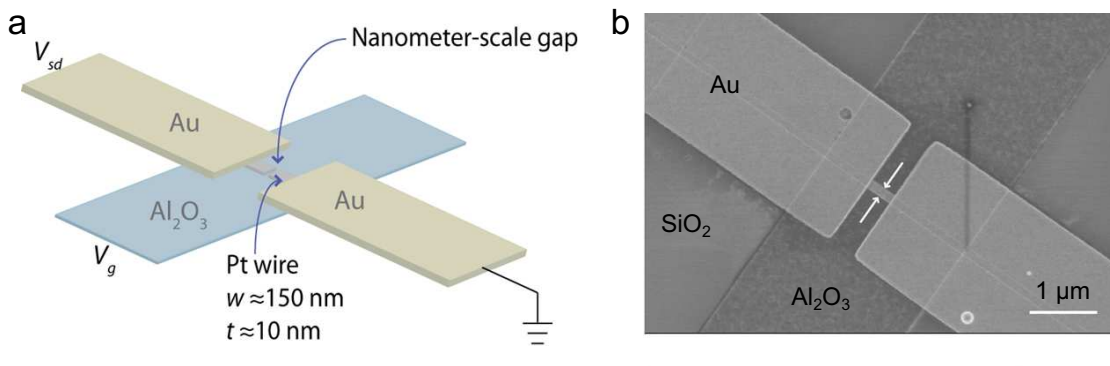
2.2.4 Coherent tunneling

Here I round out this basic overview of transport through SETs/SMTs by briefly discussing tunneling in the strongly-coupled regime. When the coupling, Γ , between a quantum dot and the electrodes is strong, the many-body interaction between the conduction electrons of the electrodes and the localized electrons on the quantum dot becomes non-negligible. One striking manifestation of this is in the appearance of a zero-bias conductance peak due to the Kondo effect in quantum dots. The Kondo effect in bulk systems is characterized by an increase in the resistivity at low temperatures. The physical origin was first explained by Jun Kondo in 1964 as arising from the increased coupling between itinerant electrons and localized magnetic impurities at low temperatures (below T_K , the Kondo temperature) to form singlet states [46,47]. The analogous phenomenon in strongly coupled quantum dots — the conduction electrons of the electrodes screening an unpaired electron on the dot to form a singlet state — results in an increase in the conductance at zero bias [46].

The Kondo effect has been intensely studied in quantum dots, including work done within our group (with collaborators) using electromigrated break-junctions and, further, mechanically-controlled break-junctions, in which the distance between electrodes can be controlled with high precision [3, 48, 49]. Single molecule (or single atom) junctions have a definite advantage over other larger quantum dots in the study of the Kondo effect — the extremely small volume increases the Coulomb energy, which exponentially increases the Kondo temperature. In molecular junctions, T_K of tens of kelvin have been observed, allowing greater experimental access to studying the Kondo effect, since its observation requires $T \lesssim T_K$.

2.3 Device fabrication

Figure 2.5: a) Pictorial depiction of a break-junction and typical dimensions. b) SEM image of a break-junction.



The electromigrated-breakjunction is central to our measurements of single-molecule transistors. The procedure for fabricating such devices has been developed and described since the early 2000s [11, 12]. In this section I will describe briefly the specific techniques and parameters I used to fabricate Au and Pt break-junctions on Al gates, using the facilities (many now obsolete) at the CNF. Much of it follows from the theses of Abhay Pasupathy, Jacob Grose, and Joshua Parks [38, 39, 50]. The procedure is as follows:

- (1) Start with a low-resistivity (highly doped) 4-inch silicon wafer with 200–250 nm thermal oxide (as purchased).

- (2) Coat wafer with photoresist (S1813) with standard procedures (prime with P-20, spin, bake at 115°C). Use a contact aligner (HTG at the time, 6 s) to define alignment marks for the 10X stepper. Develop. Descum with O₂ plasma. Etch the oxide in CHF₃/O₂ plasma with the PT72 or Oxford80 (run the process for double the expected time) and etch 4 μm into the silicon with the Unaxis 770 (OTRENCH, 8 loops). Strip the resist (hot bath is fine).

(3) Spin clean and/or plasma clean the wafer. Bake it on a hotplate at 180°C for 10 min to “dry” it. Spin LOR (3A or 5A preferred, 3500 rpm). Bake at 180°C for 5 min. Without priming, spin S1815 with standard parameters, bake. Run it through a stepper (10X at the time) to define the “thin Au” pattern. Post-exposure bake at 115°C for 2 min. Develop in MF321 for 60 s. Bake at 130°C for 5 min. Develop in MIF300 for 60 s. Descum with O₂ plasma (30-60 s). Evaporate 1 nm for Ti for adhesion and 12–16 nm of Au and liftoff in Remover 1165 (MicroChem). The thinner the better, but you need a continuous film of Au. It may be advisable to use AuPd (10 nm) for this step instead if one is concerned about Au/Al intermetallic formation (most commonly purple death), although high conductivity is probably not critical for a gate electrode.

(4) Repeat step (3) for thick Au pattern, depositing 1–2 nm of Ti and at least 120 nm of Au to make contact pads. The alignment marks for electron-beam (e-beam) lithography and dicing grid lines (optional) are also defined in this step.

(5) Repeat step (3) for Al gates (2 nm Ti, 14 nm Al). Deposit this film in the Sharon evaporator while cooling the stage with liquid N₂ for a more uniform film. Bleed in pure oxygen to ~10 mTorr to oxidize the surface of the aluminum. Wait until the sample is at room temperature before venting to air (this may take hours of purging the LN₂ line with compressed air — be patient). The native oxide is the gate dielectric. Check to see if there are any Al streaks from the resist cracking, though I have not encountered this problem.

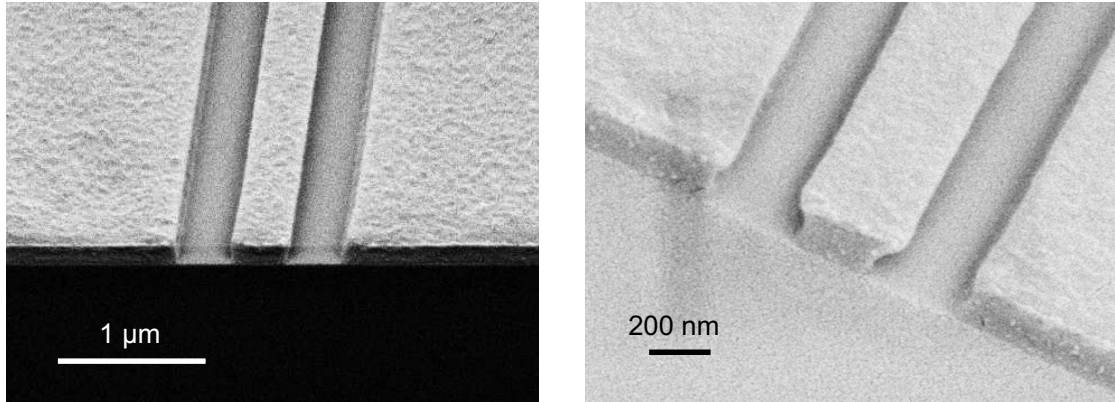
(6) Perform one or two steps of aligned (global and chip) e-beam lithography to define the nanoscale wires for electromigration. Two steps are sometimes required to define low-resistivity (thicker Au, for example) electrodes that are

also aligned to within 200 nm to contact the higher resistance segment where one wants the electromigration to occur. We used a bilayer PMMA/copolymer recipe to ensure clean lift-off. The first layer is a copolymer MMA(8.5)MAA 11% 3:1 ethyl acetate spun at 2500 rpm for 60 s and baked at 170°C for 15 min. The second layer is PMMA 495K A4 (sometimes 950K A4 is used instead), spun at 1500 rpm and baked the same way. Develop in MIBK:IPA 1:3 for 60-70 s, dunk in methanol for 15 s, rinse in IPA and blow dry. A gentle or quick (6-8 s in the Oxford 80) O₂ plasma descum is recommended afterwards. For Au break-junctions, we typically evaporate 1 nm Ti and 14-18 nm Au. For Pt, 10 nm is sufficient for a continuous film. Lift-off in acetone.

A note about the PMMA/copolymer bilayer recipe: In our later work for spin injection into graphene, the undercut property of the PMMA/copolymer layer was quite critical, so we performed a dose test with several popular recipes and sectioned the photoresist for SEM imaging. We found that the standard MIBK:IPA (1:1 or 1:3) development followed by a short isopropanol rinse did not give any undercut, except at very high dose. The methanol dip that is in some recipes turns out to make quite a difference in developing an undercut. Figure 2.6 shows the difference between the resist profile with (right) and without (left) a 10-second methanol dip. The effect of methanol in developing an undercut is clear. It is probably possible to develop an undercut with a longer isopropanol soak/rinse, but methanol seems to have a more dramatic effect due to it being more polar.

(7) Spin and bake at least 2 layers of S1827 to protect the devices (the primary threat is the water jet pressure) and dice with the silicon blade on the dicing saw.

Figure 2.6: SEM images of e-beam resist, with a coating recipe similar to that described in the text. Patterns were written with a dose of 1000-1300 $\mu\text{C}/\text{cm}^2$. Left: No methanol dip. Right: 10 s methanol dip. The samples are cleaved after development, then coated with ~ 10 nm AuPd for imaging.

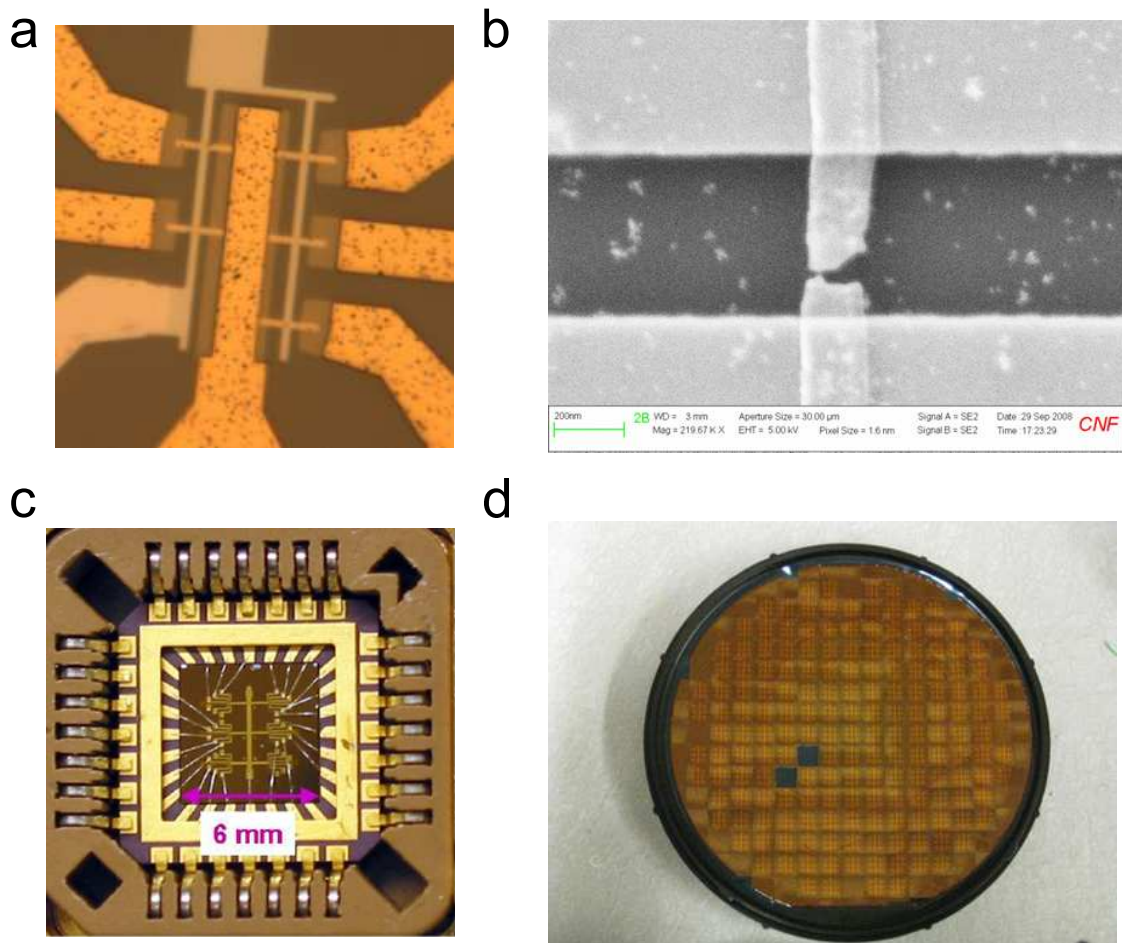


2.3.1 The trouble with Pt

One of my original goals was to fabricate more Pt break-junction devices which would be much more stable than Au break-junctions. Pt was difficult to work with for two reasons. The first was that Pt evaporates at a much higher temperature compared to Au and therefore in the Sharon it requires cooling of the stage to preserve the integrity of the PMMA resist. On the other hand, one cannot cool it to LN_2 temperatures because the PMMA would surely crack. Even with water cooling, I evaporated no more than 3 nm at a time, for a total of 10-12 nm. The CNF evaporators place the sample further from the source, but for our measurements it is necessary to keep the materials and processing as clean as possible, so we stay with the Sharon. The second more critical issue was that the Pt break-junctions would always result in weak or leaky gate oxides. Unlike Au break-junctions under which the gate voltage could be pushed to about ± 3 V, with Pt the gates would break down under 1 V. Moreover, they would blow under electromigration, even at low temperature and with feedback control and

minimal series resistance. Ferdinand Kuemmeth noted in his thesis [51] that the combination of Pt and a Ti sticking layer caused leakage even on much thicker SiO₂ (using Si as back gate). For him, substituting Cr in place of Ti solved the problem. Unfortunately, even after switching to Cr, the Al gate still broke down under electromigration. I tried going without a sticking layer, but was unsuccessful.

Figure 2.7: a) Optical image of a cluster of 5 break-junctions and the gate electrode (grey). b) SEM image of an electromigrated break-junction. Scale bar in lower left is 200 nm. c) Wire-bonded chip in a chip holder. (Photo from Janice Guikema.) d) Diced wafer protected with photoresist.



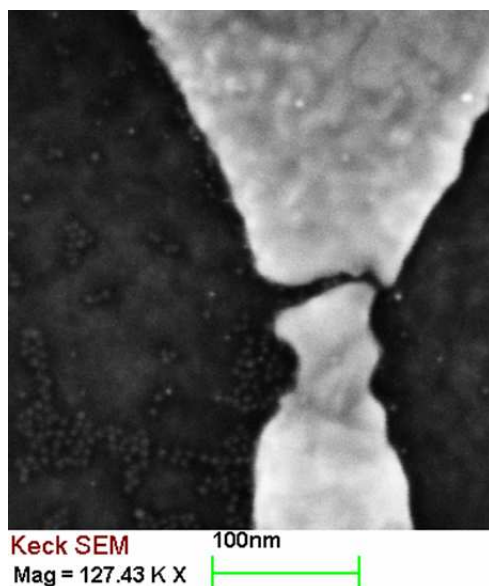
2.3.2 Device preparation for measurement

Soak individual chips in acetone and rinse with isopropanol to remove the protection layer of photoresist. For single molecule measurements, the cleaning process is critical. We plasma clean the chip for 1 min in the Oxford 80 or PT 72 and clean again in the Harrick plasma cleaner in Clark Hall immediately before molecule deposition.

The concentration of the solution that we use to deposit fullerene molecules is typically about 0.1–1.0 mM, in toluene (relatively high boiling point). We drop 25 μL of this solution on the chip, let it sit for 1–2 min, blow dry with N_2 , and repeat once for a convenient yield of devices.

I have also worked briefly with nanoparticles, including ferromagnetic FePt ones (from Chris Murray at University of Pennsylvania) and PbSe semiconductor quantum dots (from Frank Wise's group), both with diameters of 7–10 nm. We deposit the nanoparticles *after* breaking the junctions. All the nanoparticles we have worked with were protected by capping layers of long organic molecules, to prevent oxidation and clumping. We found that there is a fine balance between having too few trapped particles (concentration too low) and the particles forming clusters (concentration too high). The very simple technique described by Cui *et al.* worked surprisingly well for trapping a small number of nanoparticles in electromigrated gaps [52]. They made use of the capillary force by tilting the substrate while the solvent evaporates along the longitudinal direction of the trenches (for us, the electromigrated gaps). Figure 2.8 shows an example of an Au electromigrated break-junction where we have trapped PbSe nanocrystals by this method. Others in the group have tried electrostatic trapping with some success [53].

Figure 2.8: PbSe nanocrystals trapped in an electromigrated Au break-junction. The PbSe nanocrystals are nominally 7 nm in diameter with an oleic acid capping layer. (For best contrast, see electronic version of this thesis.)



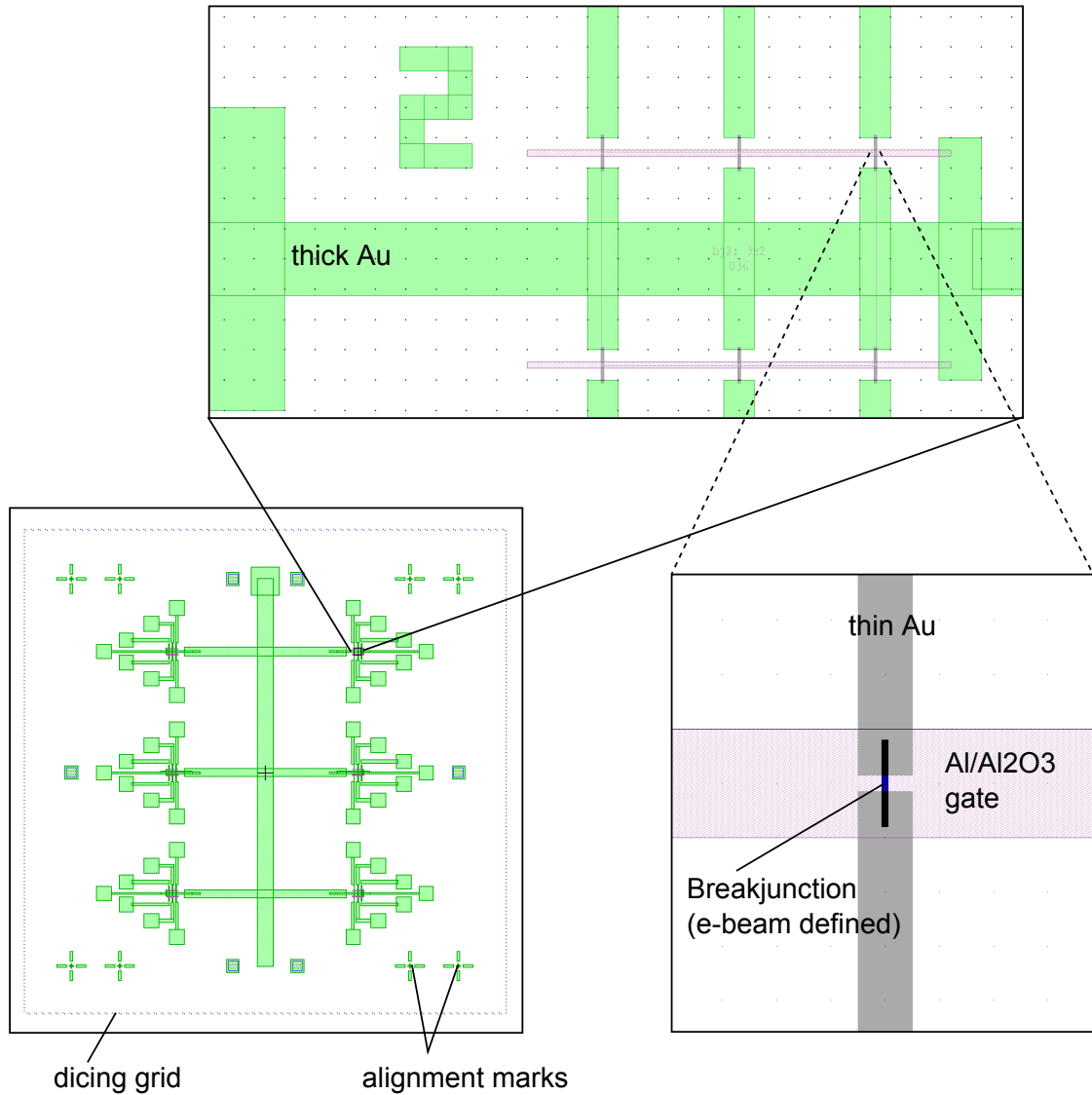
After molecule/particle deposition, we attach the chip to a chip carrier with silver paint and wirebond (Al wire) to promising devices (checked on a probe station at room temperature).

2.4 Break-junctions, 2012 edition

In 2011–2012, I modified the fabrication procedure to adapt to the new equipment in the CNF since all of the lithography tools I used previously are now gone. I chose to use the ASML deep UV stepper and the JEOL6300 e-beam tool. The ASML is highly automated and makes the photolithography steps much easier. In fact, for simple shapes like Au lines down to 100-200 nm, it is likely possible to tune the recipe (mask pattern size, resist, dose, focus, and aperture size) to pattern the smallest features with the ASML and eliminate the e-beam

step altogether. I have stuck with e-beam for the sub-micron features. Figure 2.9 shows the design of the electrodes on each die. The pattern for the ASML mask is in a file called “20110903_ReticleFlatten,” which lays out 9 images on one mask, some of which were for testing purposes.

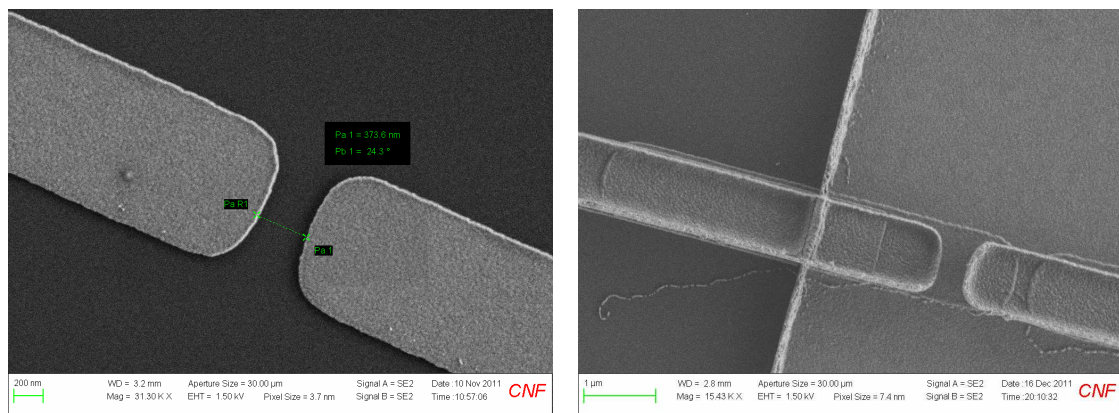
Figure 2.9: Top: one cluster of electrodes for break-junctions, grid spacing 10 μm . Bottom left: whole chip, side length 6 mm. Bottom right: a single breakjunction, e-beam wire width shown here is 120 nm. All panels: different colours represent different lithography steps. Green = thick Au. Grey = thin Au. Blue = e-beam. Purple shade = Al.



Briefly, the steps to make break-junctions are as follows:

(1) Spin the wafer with developer-soluble anti-reflection coating DS-K101-312 at 1350 rpm (5000 ramp) and hot-plate bake at 180°C for 60 s. Spin coat with UV210-0.6 at 3500 rpm (1000 ramp) and proximity bake at 135°C for 60 s. Expose the alignment marks layer on the ASML stepper. Post-exposure bake at 135°C for 90 s. Develop in Hamatech in 726-MIF for 90 s, double or triple puddle. Descum and etch the oxide in Oxford 80 (CHF_3/O_2 , 7 min total in 2 min intervals). The resist is not very etch resistant and will also harden when etched for too long. A plasma strip is usually necessary.

Figure 2.10: Left: Good lift-off from ASML photolithography. Right: Bad lift-off due to overbaking and/or underdevelopment.



(2) Plasma clean off any resist residue. Repeat the resist coating and exposure described in step (1) to define the thin Au and thick Au (contact pads, alignment marks, dicing grid) patterns for metal deposition and lift-off. The parameters of the first bake are quite critical for clean lift-off. I found that baking at 185°C hardened the resist such that it often (not always) resulted in bad lift-off as seen in Fig. 2.10. Also, for small features (sub-micron, as we have here), develop for 120 s or more; otherwise, the undercut will be insufficiently developed. Lift-off in 1165 at 65°C overnight. Rinse in acetone and isopropanol.

(3) Define break-junctions on the JEOL6300, with both global and chip align-

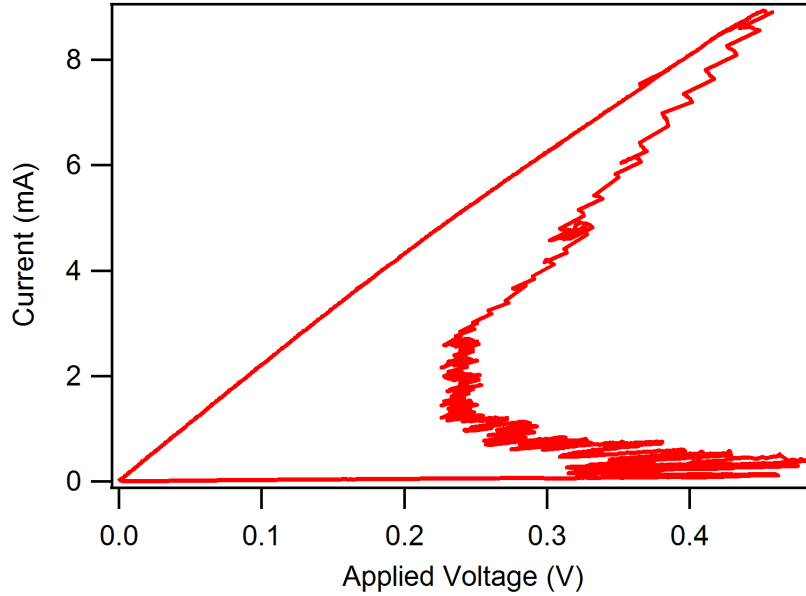
ment. For thin metal (*e.g.*, 10 nm of Pt), I find that a single layer PMMA recipe (A4, 950K, spun at 3500 rpm) results in more consistent lift-off than bilayer recipes. In case it may be helpful to future users of the JEOL6300, I have included a sample of the job deck and scheduling files (*.jdf and *.sdf) in Appendix 1.

(4) Spin and bake 3 layers of S1827 to protect the devices and dice with the dicing saw.

2.5 Electromigration

I followed well-established techniques for performing electromigration to reliably form nanometer-scale gaps without forming stray metallic clusters [54]. Feedback control implemented in the program iMeasure allows one to break the wires in a fairly controlled manner, with a high rate of “live” devices — ones with measurable tunneling current after the break. See Fig. 2.11 for an example of a current-voltage trace for the electromigration of a Au wire with feedback control. For the work on N@C₆₀ described in the next chapter, we broke the Pt wires without feedback (ramp rate 5-10 mV/s) at base dilution fridge temperature (100 mK) with the new probe which has low-resistance lines. Typically Pt wires break abruptly at about 1.0 V. This was found to provide gaps of suitable size for measuring fullerene-type molecules, determined by SEM images and electrical measurements. The specific choice of breaking parameters (feedback control, or no feedback) are highly dependent on the material and dimensions of the particular set of devices.

Figure 2.11: Current-voltage trace of electromigration of an Au wire with feedback.

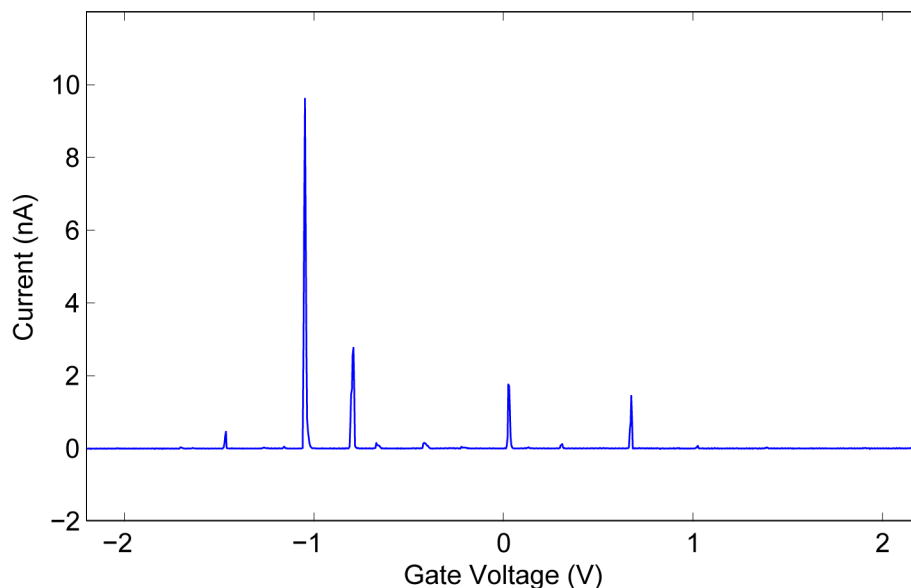


2.6 Measurement techniques

For dilution fridge temperature measurements, we cool down the device twice — the first time to break the wires with the low-resistance probe, and the second time to perform low-noise measurements with the probe with higher resistance lines. The intrinsic RC in the lines, copper powder filters and room-temperature low-pass filters removes excess thermal noise from reaching the sample.

The base electron temperature of devices cooled down in the dilution fridge is about 100 mK, calibrated from the width of quantum dot resonance peak widths. We first do quick gate sweeps at low bias (*e.g.*, Fig. 2.12), sourcing both gate and bias directly from the DAQ card, reading current through a DL 1211 (Ithaco) current pre-amplifier to identify the presence of one or more molecules in the gap. For low-noise extended sweeps as a function of gate voltage or magnetic field, we use an HP3325A function generator to supply a waveform for

Figure 2.12: Current as a function of gate voltage at a fixed source-drain voltage, $V_{sd} = 5$ mV for an N@C₆₀ device.



the bias voltage and a Yokogawa 7651 voltage source for the gate. The voltage output of the HP3325A is amplified by a PAR113 before being acquired by the DAQ card, which synchronously records the output of the DL 1211 measuring the current through the junction. dI/dV is calculated numerically from the I - V curve. The junctions are typically on the order of 100 M Ω , and capacitive currents are significant, so lock-in techniques are not used. We distinguish between tunneling through multiple molecules from the slopes of the boundaries of Coulomb diamonds (individual molecules will be differently coupled to the gate and electrodes).

We avoid applying bias voltages of much more than 10 mV to preserve stability of the junction. Before measuring the junctions, we test each gate electrode for leakage, which usually happens at about 3 V. Most junctions are fairly stable at base temperature and can be measured for long periods of time. A good junction will usually still retain its qualitative characteristics after a thermal cy-

cle to room temperature, as long as care is taken to cycle slowly and to prevent condensation on the sample.

2.7 Control samples

One of the difficulties of using break-junctions to measure molecules is that one can only identify the presence of molecules from the electronic transport characteristics as molecules are far too small to be directly imaged by any technique applicable to break-junctions. It is therefore crucial to compare measurements of molecules with those on control devices. Control measurements should proceed in exactly the same way as measurements on real devices (with molecules) except for the absence of molecules. If molecules are deposited by drop-casting in solution, control devices should be treated in the same way with pure solvent (no molecules). We have found it necessary to use high purity (HPLC grade) solvent to get clean control measurements.

2.8 Summary

In this chapter we have laid down the basis for the theory and experimental techniques required for the study of SMTs in break-junctions. The ability to interpret dI/dV data and deduce information about the energy states of the system under study will be needed for our results on $N@C_{60}$ described in the next chapter.

3.1 Scope of this chapter

This work was done while I was a first year student working with Jacob Grose. By the time I arrived he had worked out most of the fabrication and measurement details and I entered at the start of the measurement process. Much of this project is described in his thesis [38], but the development of a full interpretation of the data and the completion of the paper [55] occurred after the publication of his thesis, so here I complete the account of the full story.

3.2 Introduction

The study of the electronic and magnetic properties of individual magnetic molecules can give insight into the fundamental mechanisms of ferromagnetism. Furthermore, they hold the promise of extending molecular electronics to molecular spintronics. On their own, single magnetic molecules with long spin relaxation times have been proposed as possible qubits based on their spin degrees of freedom. There have been intense efforts in the design, synthesis, and characterization of magnetic molecules that are stable with clear magnetic character [30,31].

Much of the work in exploiting the spin degree of freedom in molecules [30] has focused on a class of superparamagnetic molecules known as single molecule magnets (SMMs). While such molecules are not the subject of this

chapter, they are highly relevant in the motivation and future direction of similar studies. SMMs are molecules that have long magnetization relaxation time and exhibit magnetic hysteresis intrinsically as a single unit due to superexchange coupling between the core metal ions. For a nice review of the research and potential of SMMs, I refer the reader to Ref. [31]. A particularly interesting phenomenon that is expected to be observed in an SMM is the quantum tunneling of magnetization, which is a classically-energetically-forbidden transition between states of $S_z = +|S|$ and $S_z = -|S|$, but quantum mechanically allowed through avoided crossings between states of different S_z upon changing the magnetic field [27,56]. One early popular candidate were Mn_{12} -based SMMs (" Mn_{12} " = $\text{Mn}_{12}\text{O}_{12}(\text{OAc})_{16}(\text{H}_2\text{O})_4$), which showed exceptional magnetic properties with $S = 10$ but suffered from degradation under higher temperatures and when in contact with metal surfaces [57, 58]. More recently, strong interest has developed for Fe_8 -based SMMs and lanthanide phthalocyanine double-decker (Pc_2Ln) SMMs for their greater stability.

When we started the work described in this chapter, Jacob Grose had previously measured the Mn_{12} -based molecules in SMT geometry and found magnetic signatures in the form of lifted degeneracy at zero-field in four out of sixteen devices, but did not observe hysteresis in any of them [57]. This was attributed to the molecules being unstable in air and therefore likely to have degraded into non-magnetic components during electromigration, which is known to cause local heating of up to ~ 500 K [54]. After this, we were able to obtain from Freie Universität Berlin a small and precious sample of N@C_{60} molecules, which are expected to be stable at high temperatures and to possess simple magnetic character.

3.3 The endofullerene N@C_{60}

Figure 3.1: Left: Pictorial representation of a N@C_{60} molecule, image adapted from Wolfgang Harneit. Right: Spin states of N@C_{60} in neutral and anionic states. The thick blue arrow represents the $S_{\text{N}} = 3/2$ of the N atom. The horizontal black lines represent the lowest unoccupied orbitals of the C_{60} molecule. The S labels the total spin of the molecule.

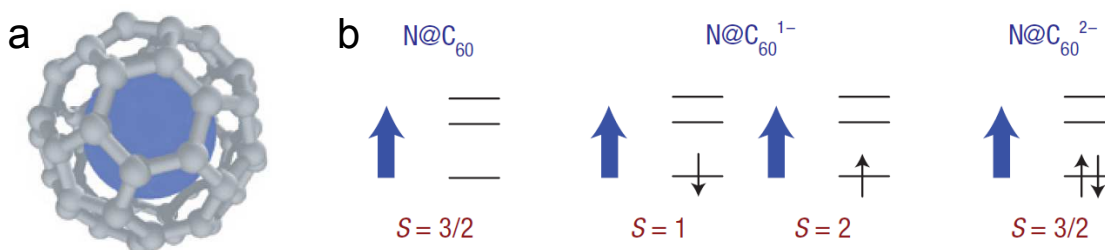
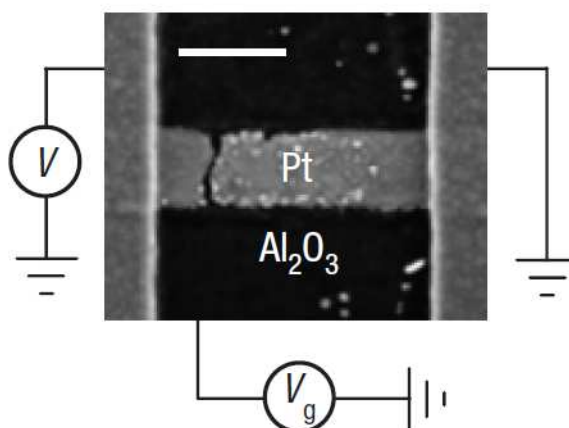


Figure 3.2: SEM image of an electromigrated breakjunction from one of the chips we used in the experiments described in this chapter. The white scale bar denotes 200 nm.



In this chapter, I will describe the results of using the devices (Fig. 3.2) and techniques described in the previous chapter to measure the endohedral fullerene (endofullerene) molecule N@C_{60} , which has a nitrogen atom inside a C_{60} cage, as shown in Fig. 3.1. Our interest in this molecule stems from the fact that the N atom largely retains its atomic properties when incorporated into this molecule, including its spin of $S_{\text{N}} = 3/2$. This gives us a stable high-spin molecule with a very convenient control species to compare against, C_{60} , that

has been extensively studied [11, 39, 59, 60]. Furthermore, unlike other small molecules in which the energy splitting due to anisotropy are beyond experimentally accessible field scales, this highly symmetric molecule with exchange coupling might allow us to study spin state transitions in a single molecule for the first time.

We infer that the nitrogen atom and the C_{60} cage are only weakly electronically coupled from cyclic voltammetry performed by Burak Ulgut which showed that the reduction peaks of $N@C_{60}$ and C_{60} occur within 25 mV of each other (attributable to variation in the film morphology of the samples used in the measurement). Michael Scheloske and Wolfgang Harneit synthesized the molecules by continuous nitrogen ion implantation into freshly sublimed fullerene layers and purified by multi-step high-pressure liquid chromatography [61]. The product was found to have purity greater than 99.5%.

Our goal was to measure the magnetic properties of $N@C_{60}$, so let us first look at the spin structure of this molecule. Figure 3.1 shows the molecule (left) and the possible spin configurations of the molecule in its neutral, 1- and 2- states (right). We show here the neutral and negatively charged states as C_{60} is known from experimental results to exist in one of these charge states when adsorbed on metals [62, 63]. When the molecule is neutral, the situation is simple, with just $S = S_N = 3/2$. In the 1- state, S could be either 1 or 2, depending on whether the coupling between the electronic spin and S_N is antiferromagnetic or ferromagnetic, respectively. These two spin multiplets are separated by the exchange energy, $|J|$. For the 2- dianion, the analogous C_{60}^{2-} is known from ESR experiments to have a singlet ground state with low-lying triplet excited states due to Jahn-Teller distortion which splits the three-fold de-

generate LUMO [64,65]. As a result, the N@C_{60}^{2-} anion is again expected to have $S = S_N = 3/2$.

In our published work, Ref. [55] and in other work related to N@C_{60} [66], this molecule is often referred to as “magnetic,” although the sense in which it is magnetic is quite different from SMMs. SMMs such as those based on Mn_{12} clusters intrinsically have strong anisotropy such that the large spin has a preferred axis. In contrast, the N@C_{60} molecule has negligible anisotropy and is “magnetic” in the sense that it has a non-trivial total spin ($S > 1/2$). The lack of anisotropy is expected from the symmetry of the molecule and the weak spin-orbit coupling of its constituents. Furthermore, as described in the rest of this chapter, it turns out that the exchange interaction gives rise to an accessible spin-state transition at standard low-temperature laboratory magnetic fields.

3.4 Theoretical background

The experiments described in this chapter were preceded and motivated by theoretical calculations by Dr. Florian Elste and Dr. Carsten Timm in 2005 on transport through a single N@C_{60} molecule weakly coupled to normal metal electrodes in a break-junction [66]. By a density-matrix formalism, they derived rate equations to calculate the current-voltage and differential conductance for this molecular junction at 0 T and 2 T. Their calculations were based on the following Hamiltonian:

$$H_{\text{el}} = (\epsilon - eV_g^*) \sum_{\sigma} a_{\sigma}^{\dagger} a_{\sigma} + U a_{\uparrow}^{\dagger} a_{\uparrow} a_{\downarrow}^{\dagger} a_{\downarrow} - J \mathbf{s}_e \cdot \mathbf{S}_N - B(s_e^z + S_N^z),$$

where ϵ is the on-site energy of electrons with spin $\sigma = \uparrow, \downarrow$, created by a_{σ}^{\dagger} , V_g^* is the electric potential at the molecule, U the Coulomb repulsion, J the exchange

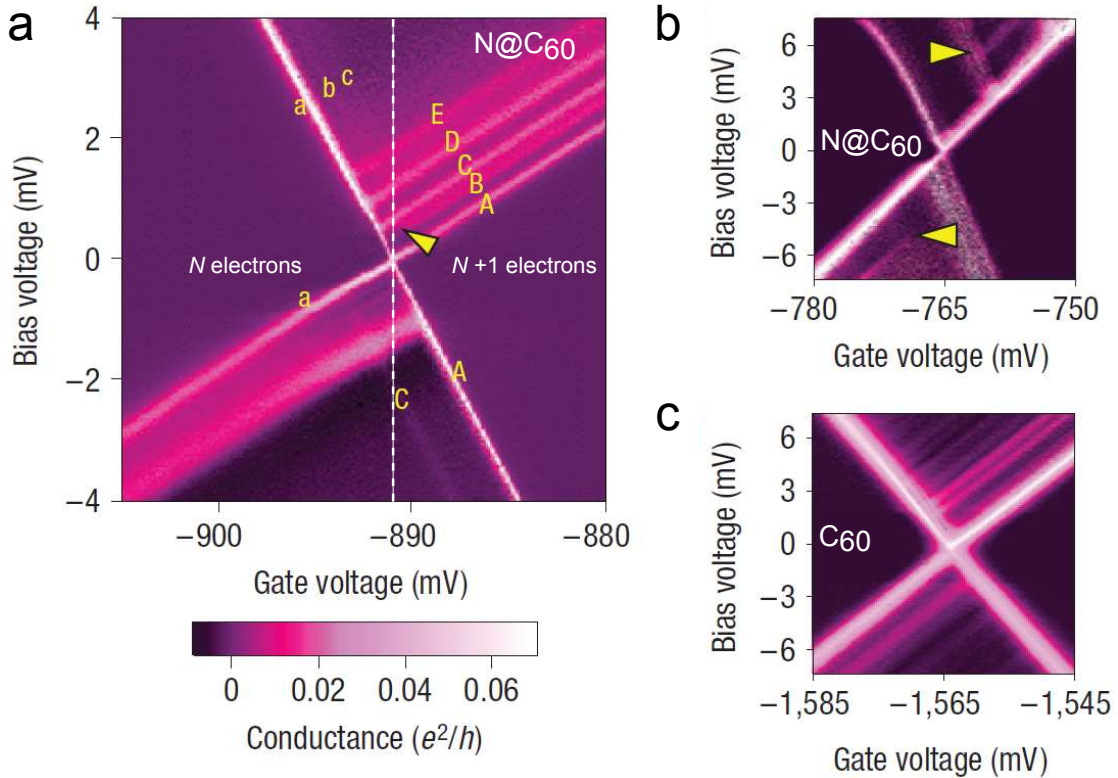
interaction between \mathbf{S}_N and \mathbf{s}_e , the spin of the electrons in the LUMO. Assuming a ferromagnetic exchange of $J \sim 1$ meV, they show that one could expect to see characteristic fine structure in the differential conductance map near the degeneracy points in the Coulomb blockade regime. This fine structure corresponds to tunneling processes involving higher energy spin states arising from the exchange coupling between the N atom and C_{60} cage. It was with these predictions in mind that we began our experimental work on this molecule.

3.5 Results and discussion

First, a word about our specific methodology in this experiment: in addition to making measurements on break-junctions with $N@C_{60}$ molecules, we also perform two types of control measurements: on devices treated with pure toluene and those treated with a C_{60} solution. On 39 pure toluene devices, we found 0 with Coulomb-blockade-type features in the gate and bias voltage scans. In contrast, we measured Coulomb blockade features in 17 out of 59 devices with C_{60} deposited and in 9 out of 19 devices with $N@C_{60}$ (Fig. 3.3). Of these, 5 C_{60} and 6 $N@C_{60}$ devices were sufficiently stable for gate and field sweeps.

The panels of Figure 3.3 show conductance maps as a function of bias and gate voltages as color-scale maps, with the gate voltage swept near a degeneracy point. Figure 3.4 shows field sweeps performed at a slightly more positive gate voltage than the degeneracy points shown in Fig. 3.3, respectively from (a) to (c). For both figures, (a) and (b) are examples of $N@C_{60}$ devices and (c) is a C_{60} control device. Characteristic features of $N@C_{60}$ will be discussed and contrasted with those of C_{60} in the following sections, but the analysis will mostly

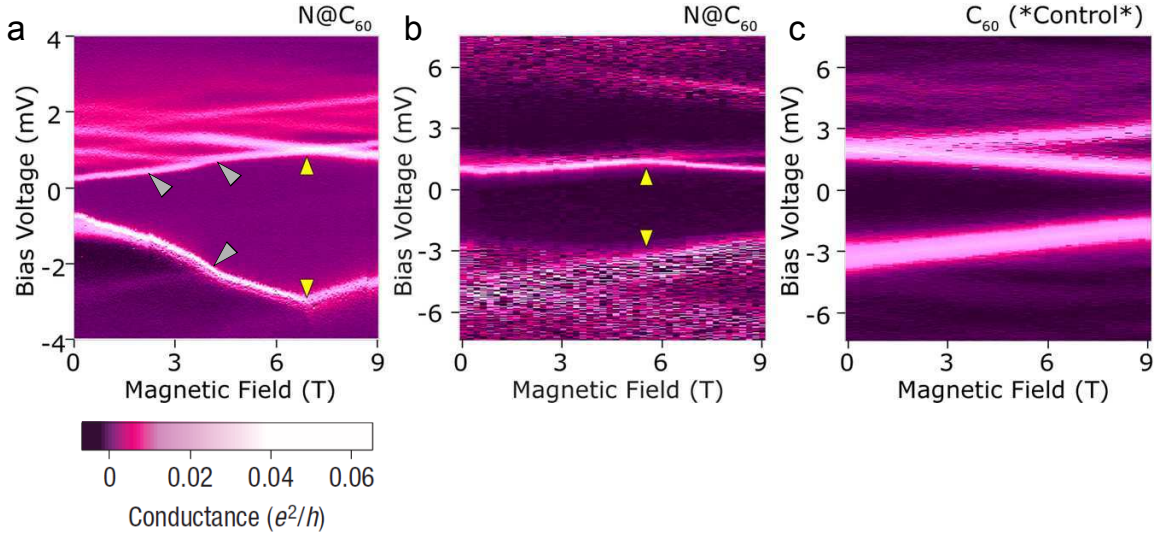
Figure 3.3: Color-scale maps of differential conductance (dI/dV) as a function of bias voltage and gate voltage at zero magnetic field. (a) and (b) are for N@C₆₀ devices, while (c) is for C₆₀. White dashed line in (a) marks the degeneracy point in gate voltage. Yellow triangles in (a) and (b) point to the termination of ETE peaks associated with non-equilibrium transitions. The labels in (a) correspond to transitions in theoretical results. (a-c) in this figure are measured on the same devices as in Fig. 3.4(a-c), respectively.



focus on the device shown in panel (a).

The most striking difference between devices with N@C₆₀ and the control devices with C₆₀ can be seen in the magnetic field dependence of the dI/dV peaks (Fig. 3.4). In four out of five devices in which we performed this measurement (at $V_g > V_0$), we observe that the conductance peaks corresponding to the boundary of the Coulomb diamond first move apart as the applied magnetic field is increased, then change to moving back closer together. This transition — a “kink” in the field-dependence of the peaks — was observed at fields from

Figure 3.4: Conductance (dI/dV) maps as a function of bias voltage and magnetic field. The left and center panels are measurements on N@C₆₀ devices while the right panel is a control measurement on C₆₀



1 to 7 T in the four devices in which it was seen. These conductance peaks correspond to tunneling processes involving a transition between the ground state with charge q and the ground state with charge $q + 1$. We have not observed this transition in any C₆₀ devices studied, such as that shown in Fig. 3.4c. As in the N@C₆₀ devices, there are low-energy excitations in the data for C₆₀, but the lack of spin transitions in the field-dependence data suggests that these are vibrational excitations.

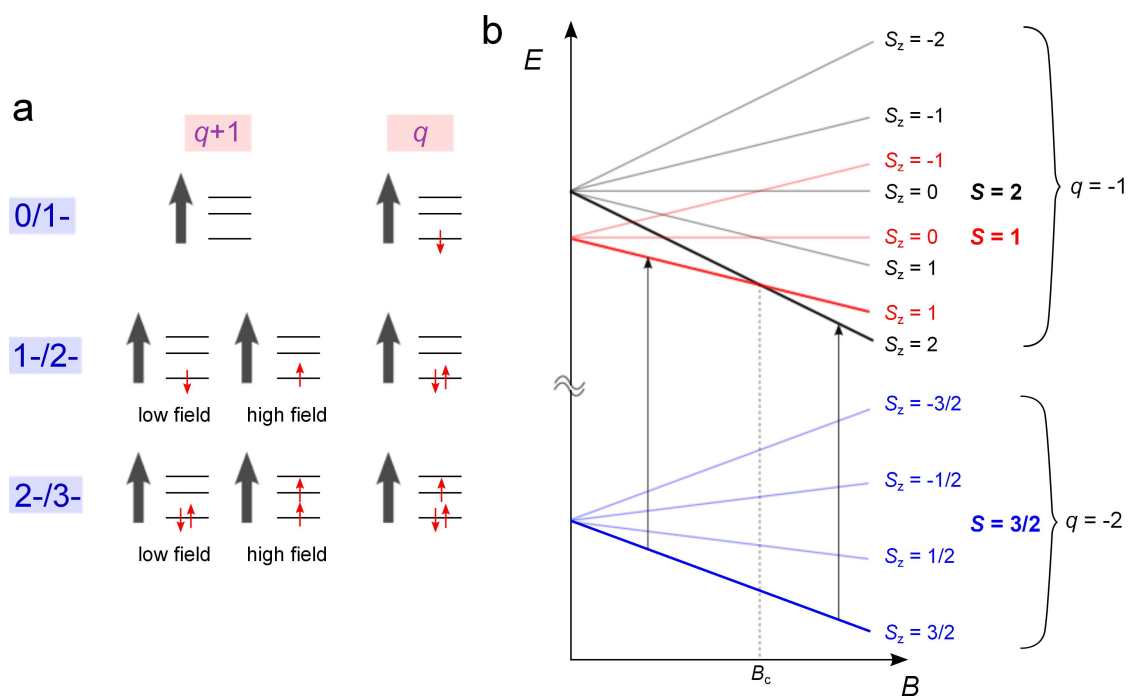
Since the field sweeps in Fig. 3.4 were taken at $V_g > V_0$, the observation that the peaks move apart indicates that $S_{z,q} > S_{z,q+1}$. In N@C₆₀ devices, beyond the transition field, B_c , a spin state transition results in the reversal of this relation, $S_{z,q} < S_{z,q+1}$. At B_c , one also observes level crossings — an excited state from $B < B_c$ becomes the ground state of $B > B_c$. Assuming that $|S_{z,q} - S_{z,q+1}| = 1/2$, the slopes of the peaks in Fig. 3.4 correspond to an electronic g -factor of $|g| = 2.0 \pm 0.3$.

The assumption of a lack of anisotropy in this molecule is supported by the

observation that the field dependence of the energy levels appear to be very close to linear, with $|g| = 2$, except for minor deviations at certain level crossings. If anisotropy is significant, since the anisotropy axis could be oriented in any direction with respect to the applied field, we would expect deviations from linearity, such as that seen in measurements on molecules with expected anisotropy (*e.g.*, Mn_{12}) [57].

3.5.1 Charge state

Figure 3.5: a) Spin states for 3 possible charge couplets. Thick black arrow represents nitrogen spin $S_N = 3/2$. Smaller red arrows represent electron spins on the C_{60} cage. b) Splitting as a function of magnetic field for different S, S_z states, showing the cross-over of the $q = -1$ ground state from having spin $S = 1$ to $S = 2$. The ground states of each spin multiplet is highlighted in thick dark lines. Vertical arrows show transitions from the q to $q + 1$ charge states. Dashed line indicates position of transition field, B_c .



To identify the charge and spin states associated with the degeneracy point

in Fig. 3.3a near which the data in Fig. 3.4a was taken, we consider the possibilities, illustrated in Fig. 3.5a:

- We can rule out 0/1- because, checking back with the gate-voltage sweep in Fig. 3.3a, we see that an excited state of the more positive charge state is involved in the level crossing with the ground-state-to-ground-state transition. The $q = 0$ charge state, with simply $S = S_N = 3/2$, does not have any such expected transitions.
- The 1-/2- transition is plausible. To satisfy the relations between $S_{z,q}$ and $S_{z,q+1}$ observed, we have to have $S_{z,-2} = 3/2$ and $\{S_{z,-1} = 1 \text{ for } B < B_c; S_{z,-1} = 2 \text{ for } B > B_c\}$. This means that at low field, the nitrogen spin and the single electron spin couple anti-ferromagnetically to give $S_{z,-1} = 1$, while at higher field the spins align.
- The 2-/3- transition is also plausible. If this were the case, the spin states would be $S_{z,-3} = 2$ (ferromagnetic coupling) and $\{S_{z,-2} = 3/2 \text{ for } B < B_c; S_{z,-2} = 5/2 \text{ for } B > B_c\}$. However, we argue that this charge couplet is unlikely since our measurements were made at $V_g < 0$ and it would imply that $q = -3$ at zero gate voltage. This situation is energetically unfavorable based on results from previous studies on the C_{60} molecule, which finds an equilibrium charge of 1- or 2- when it is adsorbed on noble metal surfaces, with the 3- state likely at a much higher energy [62,63].

By process of elimination, we identify the charge couplet associated with this degeneracy point as 1-/2-, which means that (1) the molecule is at $q = -2$ at $V_g = 0$, and (2) the coupling between the N atom and the C_{60} is anti-ferromagnetic. The first of these implications we have already addressed. The

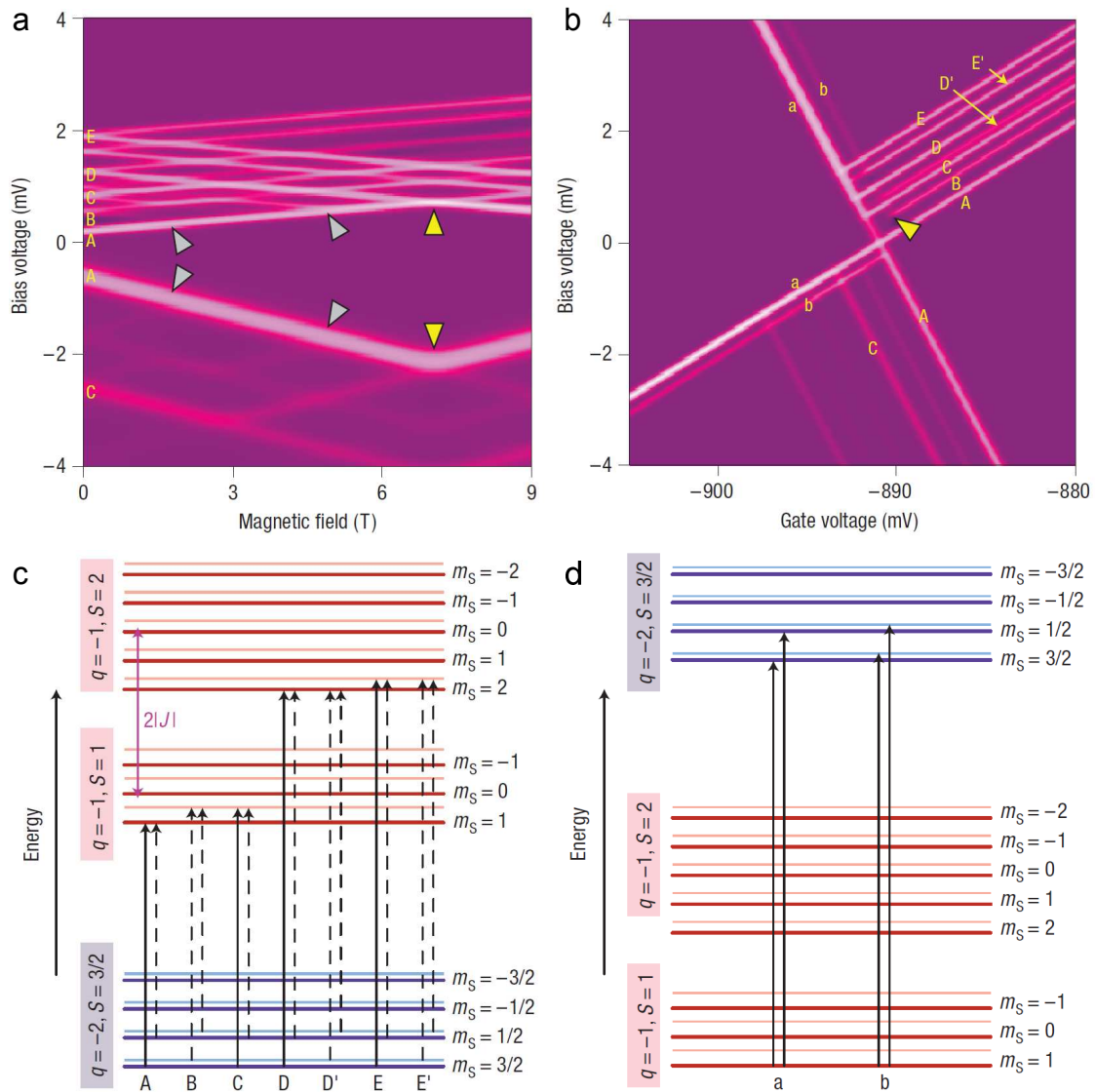
second, the nature of the exchange coupling, was somewhat unexpected based on the predictions of an *ab initio* calculation [67], which found a ferromagnetic J , on the order of 1 meV. However, we argue that the calculation of the exchange interaction is difficult as it is computed as a small difference between large total energies. Later experimental work from Roch *et al.* [45] have found results completely consistent with ours (see further discussion in Section 3.6). Figure 3.5 shows the evolution of the Zeeman-split levels, including the cross-over from a $S_{z,-1} = 1$ ground state to a $S_{z,-1} = 2$ ground state.

From the fields (1–7 T) at which the spin state transition occurs, we calculated values for the exchange coupling $|J|$ ranging from 0.06 to 0.4 meV. This fairly large range of exchange strengths and also the difference in the conductance spectra from device to device is likely due to variations in the environment for each molecule studied. The environment can influence the transport properties *via* local electric fields and by inducing deformation in the molecule.

3.5.2 Comparison to calculations

Interestingly, we can reproduce qualitatively most of the features observed in the spectra of Fig. 3.3a by assuming a simple model as shown in Fig. 3.6c,d. This includes the three multiplets ($q = -2, S = 3/2$), ($q = -1, S = 1$) and ($q = -1, S = 2$) and an excited state associated with each, possibly arising from vibrational modes or energy shifts due to charging effects. We assume that the molecule has negligible anisotropy, such that the different m_S states are degenerate at zero field, and the splitting between different S states is entirely due to exchange J . Dr. Carsten Timm used the rate-equation approach

Figure 3.6: Numerical calculations by Dr. Timm to qualitatively reproduce experimental data. a) Differential conductance, dI/dV , as a function of bias voltage and magnetic field at a constant V_g on the positive side of the degeneracy point between the $1 - 1/2$ - charge states. b) dI/dV as a function of bias voltage and gate voltage in the vicinity of the degeneracy point between $1 - 1/2$ - charge states, at zero magnetic field. The labels and grey and yellow triangles correspond to the same in Figs. 3.4a and 3.3a to allow for comparison. c,d) Energy level diagrams showing tunneling transitions included in the calculations for (a,b) at non-zero magnetic field. The dashed arrows indicate non-equilibrium transitions (ETE).



in the sequential-tunneling approximation with this energy level structure to calculate the differential conductance spectra shown in Fig. 3.6a,b. The parameters have been chosen to best qualitatively match the experimental data: $\epsilon = -3.23415$ eV, $U = 3.1$ eV, $J = -0.4$ meV, $k_B T = 20$ μ eV. The effective gate voltage V_g^* in the Hamiltonian is defined as $V_g^* = \alpha V_g + \beta_L V$ with $\alpha = 0.15$ and $\beta_L = 0.25$ yielding the best fit. They used a ratio of $t_L/t_R = 0.4$ for the tunneling amplitudes between the molecule and the two electrodes (L,R). Comparing to the experimental data in Figs. 3.3a and 3.4a, we see reasonable agreement between the pattern of the excitations in the calculations and the experimental data. The peaks (a-c, A-E) are labelled to the best of our abilities to relate the two.

The question may be raised about the origin of the excited state multiplet that we have included in the model. It is known from previous reports of both experiments and theory that the lowest internal vibrational modes of C_{60} have an energy of ~ 30 meV and a bouncing-ball mode at ~ 5 meV [11,68], both much higher than that of the excitations that we observe here. The < 1 meV excitations that we observe may be vibrational modes associated with hindered rotation or translation along the substrate. The transition c labelled in Fig. 3.3a appears to be an excited state with two vibrational quanta, based on its energy relative to transition b. This is not seen in the calculated dI/dV because we have only taken into account single-quantum excitations.

The first $N@C_{60}$ characteristic that is reproduced qualitatively within this model is seen in the gate-dependence dI/dV maps: some excited-state conductance peaks terminate at other excited state peaks instead of at the edge of the Coulomb diamond (ground state peak). A few examples of these peaks

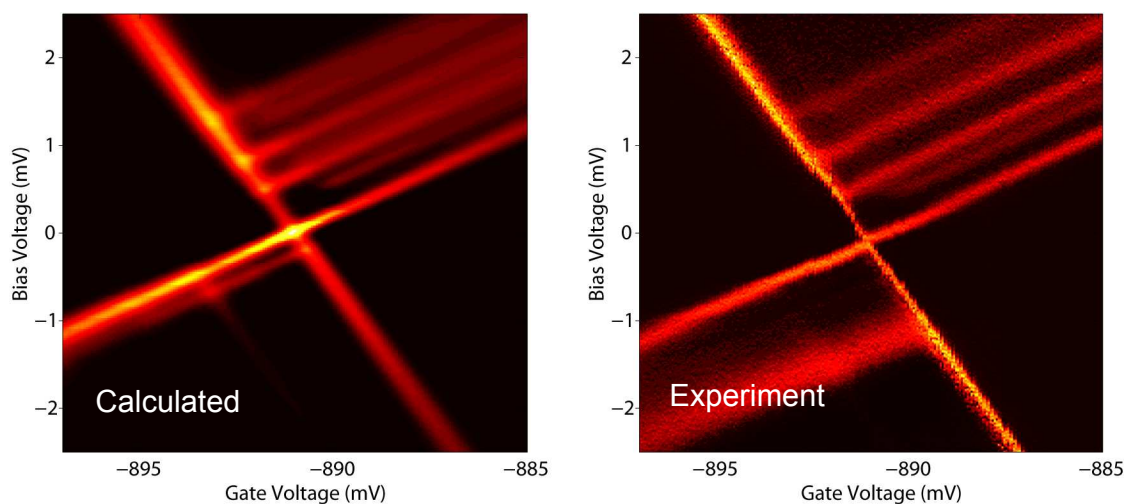
are marked by yellow triangles in Figs. 3.3a,b. This was predicted in Ref. [66] and are non-equilibrium excitations associated with excitations of this molecule. They represent tunneling processes that involve transitions from an excited state to an excited state (ETE) between the two charge states. These ETE transitions were observed in four out of six N@C₆₀ devices and in none of the thirteen C₆₀ devices (*e.g.*, Fig. 3.3c) on which we performed this measurement. While such ETE are not unique to this particular type of quantum dot and have been observed in other systems such as Co nanoparticles and fabricated quantum dot structures [69,70], their significance here lies in the fact that they agree well to the energy levels (spin states with an excited state multiplet) in N@C₆₀ shown in Fig. 3.6. The energy level transitions corresponding to each labelled peak in Figs. 3.6a,b are shown in Figs. 3.6c,d. The ground state ($q = -2, S = 3/2$) to ground state ($q = -1, S = 1$) transition is labelled A. The dashed arrows in Figs. 3.6 are non-equilibrium transitions. The next measurable transition, B, originates from the lowest energy $q = -2$ excited state and terminates at the lowest energy $q = -1$ excited state. For this transition to be energetically possible, a sufficiently large bias voltage has to be applied for a transition from the ($q = -1, S = 1$) ground state to the first excited state with ($q = -2, S = 3/2$), from which transition B can occur if the excited state does not relax to the ground state before the next tunneling event. The bias voltage (energy) requirement is the reason for the termination of the B peak at the excited state (b) instead of at the ground state (a). As a check for the plausibility of this energy model, we noted that the energy of between the ground state and the vibration-mode-like excited state can be determined by both $E_C - E_B = 0.19$ meV and $E_b - E_a = 0.20$ meV (determined from the experimental data by the voltage at which each peak intersects or would have intersected the Coulomb blockade boundary); these

values agree within experimental uncertainty (± 0.02 meV). Other energies of interest we extract from the data in Fig. 3.3 are: $E_C - E_A = 0.48$ meV, the energy of the excitation associated with the ($q = -1, S = 1$) state; $E_D - E_A = 0.93$ meV, the energy difference between the ground states of ($q = -2, S = 3/2$) and ($q = -1, S = 2$); $E_E - E_D = 0.42$ meV, the energy of the excitation associated with the ($q = -1, S = 2$) state, which is expected to be close to or equal to 0.48 meV, that of ($q = -1, S = 1$) if the excitation is not spin-related.

The second characteristic that we find to be qualitatively reproduced by the theoretical calculations is the change in the sign of the slope of the dI/dV peaks as a function of magnetic field (*i.e.*, there is a kink) as well as excited-state peaks that are opposite in slope from the ground state peak and that terminate when they intersect the ground state peak (marked by grey triangles in Figs. 3.4a and 3.6a for transitions B and C). These again are related to the non-equilibrium ETE transitions, as below the threshold voltage required for a ground-state-to-ground-state transition, the ETE transitions are not allowed.

We have noted that in the calculated spectra shown in Fig. 3.6a,b, there are additional peaks labeled D' and E' not seen in the experimental data. These are ETE transitions related to and close in energy to the transitions D and E. We believe that it is possible that these peaks are present in the experimental data but are simply not resolvable because the linewidth of the peaks are comparable to the energy differences. In the experimental data, it can be seen that the linewidths increase as a function of energy (bias voltage). If we extract the bias-dependent linewidth from the experimental data and convolve it with the calculated spectra as shown in Fig. 3.7, we find that the D' peak is completely obscured while the E' peak is far less visible.

Figure 3.7: The effect of broadening on the calculated dI/dV vs. bias and gate voltages. Left: Calculated dI/dV , same as Fig. 3.6b, but convolved with experimentally measured linewidth (as a function of bias voltage), from right panel. Right: Same experimental data as Fig. 3.3a.



3.6 Conclusion and further developments elsewhere

In this chapter, I have described our results and their interpretation from experiments on a magnetic molecule. We were able to contact individual $N@C_{60}$ molecule using electromigrated break-junctions to form a single molecule transistor. From the magnetic field sweep data near a Coulomb blockade degeneracy point, we identified the charge states as mostly likely being $1-/2-$ with anti-ferromagnetic coupling between the nitrogen spin and the electron spin on the C_{60} cage. We have shown that a spin state transition is accessible in laboratory fields and can be distinguished by electrical measurements. The next steps include trying to manipulate spin states by other means (*e.g.*, microwave excitation), improving the consistency of device assembly (*e.g.*, by chemically modifying the molecule/metal contact), and improving read-out strategies, possibly to enable measurement of spin state life-times. In the rest of this section, I describe some concurrent or subsequent work by the Wernsorfer and Balestro group on

the spin states of single molecules in SMT geometry to illustrate the power of this technique.

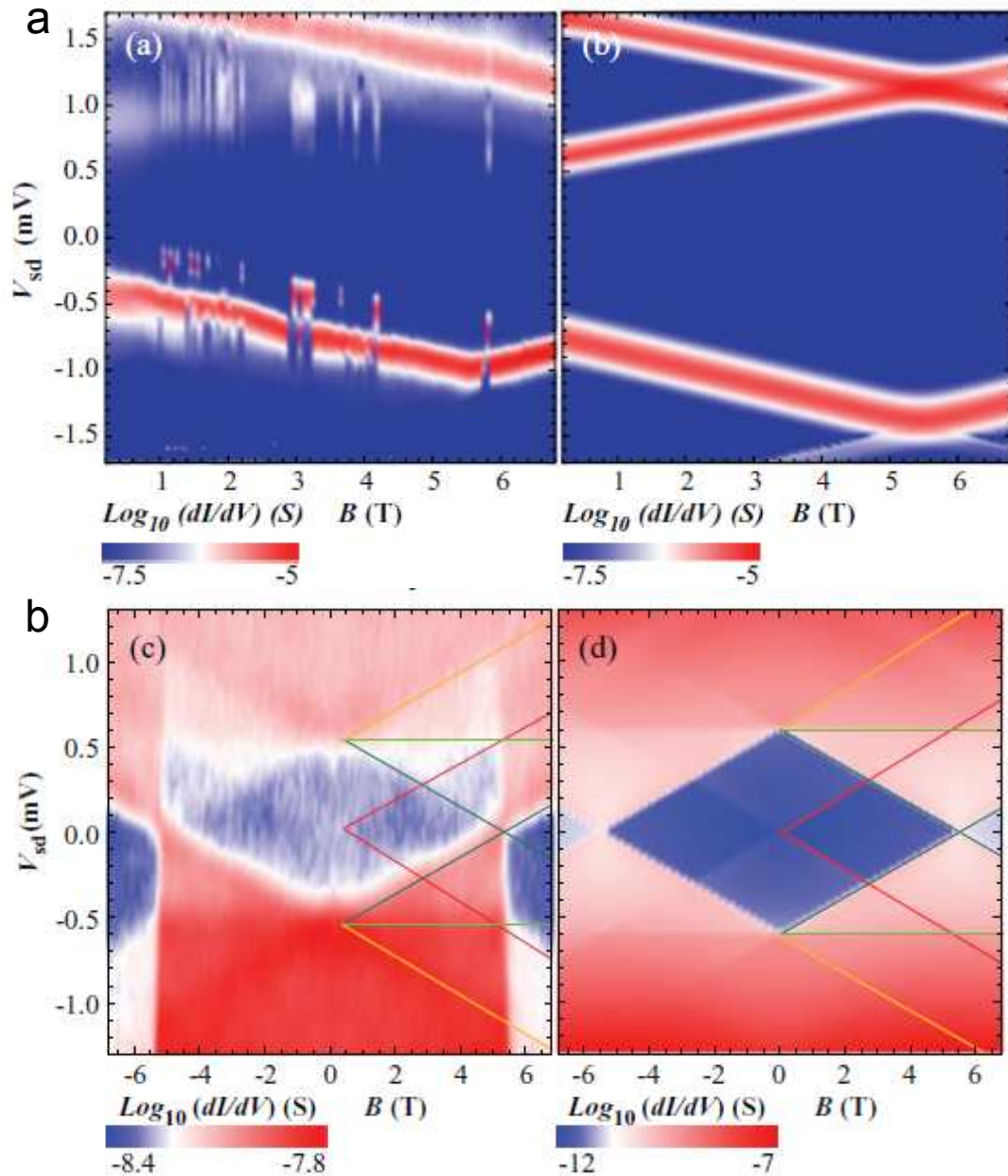
3.6.1 Cotunneling in N@C₆₀

We were pleased to see our results independently confirmed in 2011 by Nicolas Roch *et al.* [45]. They also studied the N@C₆₀ molecule in SMTs formed by electromigrated break-junctions. The first half of Ref. [45] showed magnetic-field dependence of dI/dV that on the positive side of the only degeneracy point in their field range, and they observed a kink as we did at a field of about 5.5 T (see Fig. 3.8a), and the best fit to experimental data yielded exchange coupling of $J \simeq -0.3$ meV. The antiferromagnetic exchange interaction between the C₆₀ spin and the nitrogen spin they observed is consistent with our results. They further extend the study to the regime of intermediate molecular-lead coupling, where cotunneling occurs. Cotunneling transport is a higher order process involving only one charge state, which Ref. [45] argues allows for easier interpretation of the magnetic-field dependence data. The evolution of steps in the cotunneling spectra, shown in Fig. 3.8b, for both sides of the degeneracy point corroborate the interpretation of the charge state couplet as $1-/2-$.

3.6.2 Quantum phase transition in C₆₀

Also related to this discussion is an earlier work also by Dr. Roch and his colleagues in 2008 which was published after our work described in this chapter was submitted [71]. Roch *et al.* described measurements of a “quantum

Figure 3.8: All panels are taken from Ref. [45] by Roch *et al.* a) dI/dV in the weakly coupled regime, which qualitatively agrees with our results shown in Figs. 3.3a and 3.4a. b) Results of calculations to reproduce the data in (a). c) dI/dV in the cotunneling regime for $q = -1$, showing the expected magnetic field behaviour for the same spin assignments as in our work. d) Calculations to reproduce (c).



phase transition” in a C_{60} SMT induced by a gate voltage between singlet and triplet electronic spin states. While this may seem to contradict our claim of the absence of a magnetic transition in C_{60} devices, we note that this transition was observed in the cotunneling regime in a device where the molecule was relatively-strongly-coupled to the electrodes, whereas our measurements were done near a degeneracy point in a weakly-coupled device. They were only able to induce a spin state transition with magnetic field in a very narrow range of gate voltage, near the center of Coulomb blockade region where the singlet-triplet splitting is sufficiently small. Due to the weakly-coupled nature of the devices we were able to study, we could not resolve such higher-order cotunneling features in these regions. Furthermore, while we performed our measurement at a negative voltage, they observed the singlet-triplet transition at ~ 1.9 V, more positive than two degeneracy points. It is likely that our devices were measured at different charge states. Having resolved this “inconsistency,” we are much encouraged by this work for its demonstration of the richness of physical phenomena that can be observed in such systems.

3.6.3 Electronic read-out of the nuclear spin of an SMM

Finally, I would like to highlight work from Wernsdorfer, Balestro, *et al.* from Grenoble published very recently (August, 2012) [72]. Using electromigrated Au break-junctions to contact an individual SMM $TbPc_2$ molecule (Pc = phthalocyanine), they measured the conductance while sweeping the magnetic field with a vector magnet that allows careful tuning of the direction. This molecule has a ground state total electronic angular momentum of $J = 6$, as well as a nuclear spin of $I = 3/2$. Their interpretation of the conductance data is that the

transport occurs through a quantum dot located on the organic ligands, which is exchange coupled to the Tb^{3+} ion. The conductance exhibits abrupt switching in the field sweeps, corresponding to a quantum tunneling of magnetization (QTM) between $J_z = \pm 6$ states. The precise field at which this switching occurs (± 14 mT and ± 40 mT) is influenced by the coupling between J and I and constitutes a read-out of the nuclear spin states $I_z = \pm 3/2, \pm 1/2$. By varying the time between sweeps, they measure the transition matrix between spin states and find that the level life time of the nuclear spin is on the order of tens of seconds. The combination of long life time, non-invasive electronic read-out ability and molecular stability makes this system extremely promising for use in quantum logic and computation. It will be exciting to see further investigation into the feasibility of coherently manipulating the spin of this SMM.

CHAPTER 4
STATISTICAL MEASUREMENTS OF SINGLE MOLECULE
CONDUCTANCE

4.1 Introduction

The low-temperature measurements of single molecule junctions in electro-migrated break-junctions described in the previous chapters are well suited to studying low-energy phenomena in individual molecular junctions [11, 12]. However, because of the strong dependence of the characteristics of a molecular junction on the junction geometry, other techniques have also been extensively pursued in which the junction geometry can be varied controllably and/or repeatedly.

Using the ultra-high resolution of the scanning tunneling microscope (STM), researchers have been able to probe the conductance through a molecule as a function of position and energy, in effect mapping its orbital structure [5, 6, 73]. At Delft University of Technology, van der Zant, van Ruitenbeek *et al.* used mechanically-controlled break-junctions at low temperature and in vacuum to build histograms of the conductance of atomic and molecular junctions [15, 16, 74]. Another method pioneered by Xu and Tao in 2003 [17] is the repeated formation of molecular junctions in solution with statistical analysis. In this work, a molecular junction with 4,4'-bipyridine (and also dithiol-alkanes) was formed repeatedly and the resulting conductance traces binned into histograms. Xu and Tao were able to measure sharp conductance peaks at $1\times$, $2\times$, and $3\times 0.01 G_0$, which they interpreted as corresponding to the conductance of 1, 2, and 3 molecules in parallel in the junction. However, the data analysis was se-

lective in that only the traces with a plateau in the expected conductance range were kept for binning into histograms. This method was therefore susceptible to bias and was likely representing only a small slice of the entire picture of the molecular junction under study. As will be discussed later in this chapter, recent advances in this type of measurement has eliminated the need to do selective analysis and has allowed us to independently reproduce completely consistent results for the conductance of specific molecules.

The experiments described in this chapter were begun by Dr. Mitk'El B. Santiago-Berríos of the Abruña group. Joshua Parks of our group and I joined the project in the early stages and when Dr. Santiago-Berríos accepted a position in Puerto Rico, we adopted it while continuing our collaboration with the chemists in the Abruña group, to whom we are very grateful.

4.2 Conductance of atomic-sized contacts

Before moving on to molecular junctions, it is both instructive and important to consider the properties of the much-studied system of atomic-sized conductors. An excellent review is Ref. [75] by Agraït, Yeyati and van Ruitenbeek. This section will outline some of the major concepts to consider when dealing with electronic transport in the meso- to nano-scale quantum regime.

4.2.1 Length scales — bulk, mesoscopic, nanoscale

In bulk macroscopic conductors, Ohm's law applies, such that the current being directly proportional to the potential applied. In the simplest picture, this can

be intuitively explained by the free-electron Drude model, starting from:

$$\frac{d}{dt}\mathbf{p}(t) = q\mathbf{E} - \frac{\mathbf{p}(t)}{\tau},$$

where $\mathbf{p}(t)$ is the moment of the carrier of charge q in an electric field of \mathbf{E} , and τ is the mean time between scattering events. As the size of the conductor is decreased, several length scales become relevant: the phase-coherence length, the mean free path, and the Fermi wavelength. The phase-coherence length is related to the diffusion constant D and the phase coherence time τ_ϕ (the time over which quantum coherence is preserved), $L_\phi = \sqrt{D\tau_\phi}$, and can be measured from quantum interference phenomena such as weak localization and universal conductance fluctuations. The elastic mean free path, l , is the mean distance travelled between elastic collisions with scatterers (impurities and defects) and its relation to the conductor size determines whether carrier motion is ballistic or diffusive. Finally, the Fermi wavelength, $\lambda_F = 2\pi/k_F$, determines the “quantum-ness” of the conduction electrons – the relevance of the wave nature of the electron.

The atomic and molecular junctions discussed in this chapter have transverse and longitudinal dimensions, W and L , on the order of 0.1 nm and 1 nm, respectively, which is close to the scale of the Fermi wavelength in metals such as Au, about 0.5 nm. It is therefore necessary to treat the problem fully quantum mechanically. On the other hand, let us first consider the semiclassical expression for conductance through a ballistic contact ($L < l$) with transverse dimension a biased at a potential, starting from the following expression for the current density written as a function of the position \mathbf{r} across the junction

$$\mathbf{j}(\mathbf{r}) = \frac{2e}{L^3} \sum_{\mathbf{k}} \mathbf{v}_{\mathbf{k}} f_{\mathbf{k}}(\mathbf{r})$$

where $\mathbf{v}_{\mathbf{k}}$ is the group velocity of electrons in momentum state \mathbf{k} , and $f_{\mathbf{k}}$ is the

distribution function. We treat the electrodes as reservoirs with electron distributions that (written in terms of energy E now) follow the Fermi-Dirac distribution

$$f(E, \mu_i) = \frac{1}{1 + e^{\frac{E - \mu_i}{k_B T}}},$$

where $i = s, d$ for the source and drain. At zero temperature, summing over the states originating from each of the two electrodes, the net current arises from the states within the difference in potential V between the electrodes ($\mu_s - \mu_d = eV$) due to the bias V applied — $j = ev_z(E_F)\rho(E_F)(eV/2)$, where $\rho(E_F)$ is the density of states and $v_z(E_F) = \hbar k_F/2m$ is the average velocity in the direction of the junction. Integrating over the circular cross-sectional area of radius a , one arrives at what is known as the Sharvin conductance,

$$G_s = \frac{2e^2}{h} \left(\frac{k_F a}{2} \right)^2$$

which can be used to estimate the conductance of mesoscopic contacts, dependent on only the electron density through the Fermi wave-vector. From this expression, one estimates that for a Au wire of transverse dimension equal to the Fermi wavelength, the conductance would be on the order of $2e^2/h$ and proportional to the area of the contact. In fact, the conductance of an atomic-sized wire is measured to jump between discrete values as the wire dimension decreases to the single-atom limit. This can be understood if we follow the Landauer formalism.

4.2.2 Quantum transport — the scattering approach

The Landauer formula [76] relates the conductance of a quantum conductor to transmission values of its transport channels. We consider a one-dimensional

wire, highly confined in the transverse direction such that the corresponding energy states are discrete quantized levels, which we will refer to as “channels” of transmission. If we first consider 1-D ballistic transport through a single channel without any electrode/interface effects, the current can be written as the sum over states originating from the source and drain

$$I = \frac{g_s e}{L} \sum_k v_k (f(\epsilon_k, \mu_s) - f(\epsilon_k, \mu_d))$$

where $g_s = 2$ is the degeneracy due to spin. We can convert this to an integral with the normalization factor $L/2\pi$

$$I = \frac{g_s e}{2\pi} \int v_k (f(\epsilon_k, \mu_s) - f(\epsilon_k, \mu_d)) dk.$$

Now changing from momentum to energy with $v_k dk = v_k (d\epsilon/dk)^{-1} d\epsilon = d\epsilon/\hbar$, we get

$$I = \frac{2e}{h} \int (f(\epsilon_k, \mu_s) - f(\epsilon_k, \mu_d)) d\epsilon.$$

At zero temperature, the Fermi-Dirac distribution is a step function, and this yields $I = GV$, where $G = 2e^2/h \equiv G_0$ is the conductance of a single perfectly transmitting channel and $eV = \mu_s - \mu_d$ is the bias potential.

We now consider more generally transport with scattering from interfaces and impurities, and imagine for simplicity a junction with N modes on each lead, and write a $2N \times 2N$ scattering matrix

$$\mathbf{S} = \begin{bmatrix} r & t' \\ t & r' \end{bmatrix}$$

where r, t, r' and t' are $N \times N$ arrays with elements r_{ij} and t_{ij} that are the reflection and transmission amplitudes, respectively, from mode i to mode j . The respective probabilities are denoted $T_{ij} \equiv |t_{ij}|^2$ and $R_{ij} \equiv |r_{ij}|^2$. For 1-D conductors,

we have already seen that the current is independent of velocity and density of states from the above, so at zero-temperature,

$$I_{ij} = \frac{2e}{h} T_{ij} (\mu_s - \mu_d).$$

Adding up contributions from all modes to get the total current:

$$I = \sum_{i,j=1}^N I_{ij} = \frac{2e}{h} (\mu_s - \mu_d) \sum_{i,j=1}^N T_{ij} = \frac{2e}{h} (\mu_s - \mu_d) \sum_{i,j=1}^N |t_{ij}|^2 = \frac{2e}{h} (\mu_s - \mu_d) \text{Tr}(tt^\dagger).$$

With $\mu_s - \mu_d = eV$ and $T \equiv \text{Tr}(tt^\dagger)$, we arrive at the Landauer formula

$$G = (2e^2/h)T_{12} = G_0 T.$$

According to this formula, the conductance of a nanoscale contact or wire is determined by the number of channels, N , and the transmission of each. In systems where ionized impurity scattering and intermode scattering is weak, the conductance approaches $G = 2Ne^2/h = NG_0$. This quantization of conductance has been observed in quantum point contacts fabricated in 2-dimensional electron gases [77,78].

4.3 Transport through single molecules

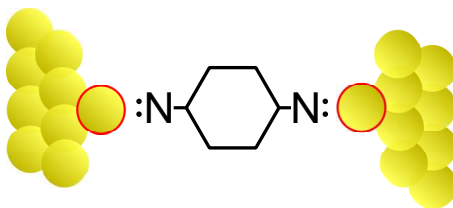
4.3.1 Physical understanding

After the preceding discussion about general nanoscale junctions, let us consider what physically happens in the experiments described in this chapter — the repeatedly-formed breakjunction. We begin with the tip and substrate in good contact, assuming that at least in some places they have essentially joined (Au-Au bond made). As we pull the two apart, at some point in time, due to the

mobility of Au atoms, what remains will be a single-atom Au wire. The formation of atomic wires has been directly seen using ultra high-vacuum tunneling electron microscopy [79]. Simultaneous conductance measurements showed that the conductance of a single strand of Au atoms is close to $1 G_0$, corresponding to one channel that is almost fully transmissive (calculations and shot noise measurements support this interpretation, as opposed to the situation of multiple partially transmissive channels) [80]. Such atomic wires can be stable for times on the order of an hour in a high-vacuum ultra-stable STM or mechanical break-junction setup [74].

Linker groups on molecules

Figure 4.1: Illustration of a molecular junction with diamine linker group.



Upon further separation of the electrodes, the atomic Au wire will eventually yield and break. This presents under-coordinated Au atoms on the surface of the two electrodes. In the presence of molecules (in solution, for example), these sites are where linker groups preferentially bind. What happens at this stage is highly dependent on the end-group on the molecule. Linker groups such as amines, phosphines, methyl-sulfides and pyridines possess electron lone pairs (on the N, P and S atom, respectively) that can form bonds with under-coordinated Au atoms that sit atop the electrode surface (Fig. 4.1) [81–83]. Certain groups including amines, dimethylphosphines and diphenylphosphines are found from DFT calculations to only form flexible

bonds to such undercoordinated Au atoms in specific motifs by the delocalization of the lone pairs [82]. It is this specificity that yields well-defined conductance peaks in histograms without any data selection. With these linker groups, as the junction is pulled apart, the flexibility of the bond will accommodate changes in inter-electrode distance to a certain extent, and then either an Au atom will shift in position or the linker-Au bond will break. The shifting of an adatom between sites (hollow, bridge, atop) occurs with relative ease, but beyond that, computations indicate that the break occurs at the linker-Au junction rather than at an Au-Au bond [84]. Other endgroups such as the pyridine appear to be less specific, and pyridine in particular is assumed to have two stable binding motifs on Au, leading to two peaks in histograms.

At the other end of the specificity spectrum is the thiol endgroup, perhaps the most studied one in the history of molecular junctions with Au electrodes, for its exceptionally strong binding to Au surfaces and its use in forming self-assembled monolayers on Au surfaces [85–87]. While the protonated thiol group (SH) can form coordination-type bonds with Au, a much stronger covalent bond is formed between Au and the deprotonated form of the endgroup, a thiolate-Au bond. This bond is, in fact, shown to be stronger than the Au-Au bond, such that as a thiol-bonded junction is pulled, the Au atoms are more likely to be rearranged than for the thiolate-Au bond to break (and possibly re-form). While a strong bond may appear to be desirable, the robustness of the thiol-Au bond leads to complications in statistical measurements in that the thiol can attach in a wide variety of motifs in addition to forming covalent bonds. Moreover, disulfide bonds can form as well as thiolate-Au-based polymeric chains, which gives rise to a wide range of conductances [21, 86, 88].

4.3.2 Theoretical efforts

Historically, much theoretical work has been done to compute the characteristics of single molecule junctions. If one can reliably reproduce conductance characteristics from first-principles calculations, it would lead to insight about the physical mechanisms underlying the conduction of electrons through these junctions. Furthermore, it would allow much more efficient design and improvement of functional molecules for potential applications. Progress in single-molecule junction calculations will likely benefit calculations for nanostructured materials and bulk materials as well.

Most single-molecule conductance calculations rely on density functional theory (DFT) with a suitable approximation for the exchange-correlation potential — the local-density approximation (LDA) or generalized gradient approximation (usually an improvement over LDA for molecular junctions) [89–91]. In a typical calculation, a potential is imposed across bulk electrodes and the structure of the molecule and the first few surface layers of the electrode (including the contact points) are “relaxed” and the electronic structure is calculated in a Kohn-Sham ground state DFT calculation. The conductance is then calculated in a non-equilibrium Green’s function DFT approach using the Landauer formula [92].

While results were reasonably consistent with those found in experimental for the absolute simplest systems such as metallic atomic junctions [93] or for the H₂ molecule [15], for even simple organic molecules such as benzene, the calculated values were often off by an order of magnitude or more [89]. Part of the difficulty in such calculations is the inherent uncertainty in the contact geometry in actual experiments. In all types of single molecule conductance

measurements except high-vacuum scanning tunneling microscopy, the precise bonding configuration between the molecule and the electrodes is not known or controlled. This is the primary reason for performing statistical measurements and comparing to calculations for a large range of possible geometries. However, the main cause for the discrepancy between theoretical and experimental conductance values is generally recognized to be the inability of DFT to treat self-interaction in the exchange-correlation potential and also many-body correlations [91,94,95]. This leads to underestimates of the HOMO-LUMO gaps (consequently, overestimate of the proximity of the density resonances to E_F) in molecular junctions, which translates to overestimates of the conductance [89, 90, 92]. The calculation of trends in conductance as a function of various parameters such as molecular length, substituents, and molecule twist angle would clearly be influenced, even if in a less drastic manner, by this error in the HOMO-LUMO gap.

Driven by the apparent discrepancy between experiment and theory, much progress has been made by theorists in recent years to improve the exchange-correlation potential approximations used in DFT calculations. Neaton *et al.* used the *GW* approximation [96] for the electron self energy to compute the electronic structure of benzene adsorbed on graphite and found a change in ~ 3 eV in the quasiparticle gap arising from the electron correlation energy that is absent from Kohn-Sham DFT calculations [97]. The inclusion of correlations at the second Born or *GW* levels appear to eliminate some of the artifacts and errors in Kohn-Sham DFT [98–100]. A less costly strategy was first proposed by Quek *et al.* in Ref. [89] and then refined in Ref. [101], which corrected for two components: one is the difference between the DFT HOMO and LUMO energies and the measured gas phase ionization potential and electron affinity; the second is

an “image charge” term arising from the polarization effect of the electrode on the energy of the LUMO or HOMO — this quantity is directly computed from a simple image charge model [97]. Refs. [89] and [101] found that this correction leads to quantitative agreement between experiment and calculations for the conductance and decay constant (molecular length) for oligophenyldiamine and alkanediamine junctions.

4.4 The “sewing machine”

In recent years, significant advances have been made by the Venkataraman group and their collaborators in the repeatedly-formed breakjunction technique (often referred to as “modified STM”). A key finding was the importance of the end-groups on the molecule measured in these types of experiments. It turns out that one can measure a peak in the conductance histogram without data selection by careful selection of the end-groups [21]. For example, on the same central benzene unit, the amine group yields a relatively sharp conductance peak, while the isonitrile group yields a broader peak and the thiol group does not yield a well-defined peak at all. This crucial finding and clever compound selection/synthesis has enabled detailed studies of the dependence of molecular conductance on variables such as molecular length, chemical substituents and twist angle [21, 102, 103].

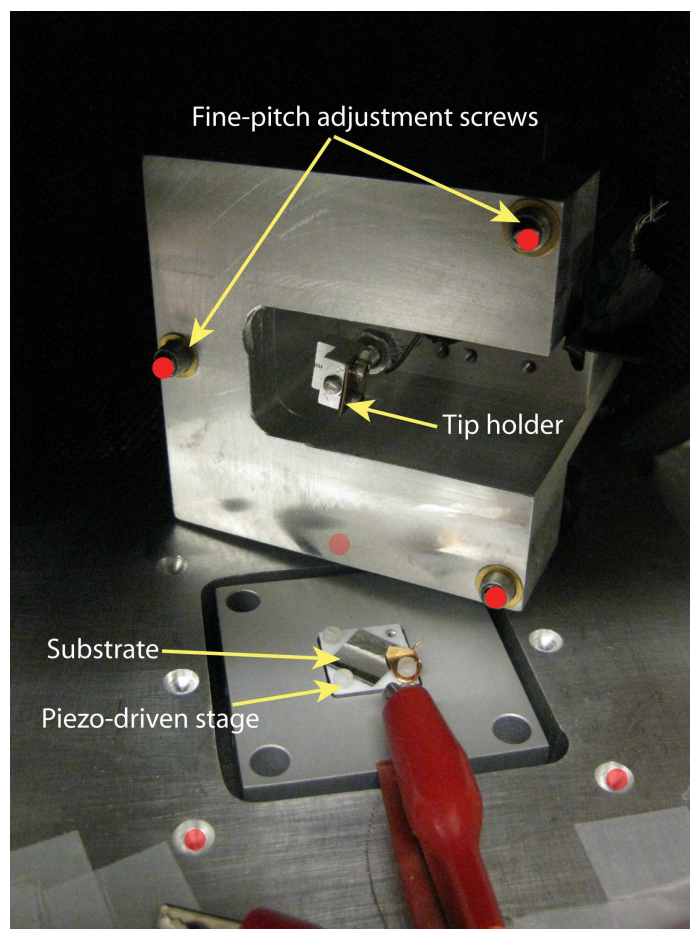
4.4.1 First version

In our first attempt to build an apparatus to perform such statistical ambient-condition measurements, we inherited parts for a design in which the tip is mounted on a piezo-electric actuator connected to a axial motor (the assembly is sourced from Physik Instrumente [PI]). The substrate was affixed to an aluminum base, on which the tip-actuator assembly is mechanically mounted. This assembly sat atop an aluminum plate on bike tire tubes inside a foam/ plexiglass/copper wire mesh cage for acoustic and electromagnetic isolation. We were able to measure reasonable conductance histograms for Au contacts and for small molecules with this simple setup.

4.4.2 Upgraded version

To further improve the stability and possibly add capabilities to the apparatus, a redesign was necessary. With advice from the Venkataraman group, we purchased from Mad City Labs a single axis high precision nanopositioning system, the Nano-HSZ with the HV amplifier bypass and open loop control options. We practically never use the HV amplifier because we need precision and not range. The full range of this stage is about 10 μm , and the position precision is sub-nanometer with the feedback option turned on. In our experiments, we use the NI DAQ card to output the control voltage to the amplifier (on bypass mode), so the DAQ output voltage directly controls the piezo stage. Ten volts give nominally 667 nm of travel. For anyone using this piezo stage in the future, the clicking noise that occurs at every significant move is normal and not a sign of problems.

Figure 4.2: The tip holder and the Nano-HSZ stage mounted on an aluminum base.



We machined an aluminum base on which to mount the stage from MCL. The tip holder screws into a solid aluminum block, which sits on the aluminum base, contacting through three fine-pitch screws from Thorlabs. These serve as the coarse adjustment of the tip position. The substrate is isolated from the metal stage by a piece of Teflon and is secured by a beryllium-copper clamp piece with a nylon screw. To set up a measurement, the Au tip is fastened to the tip holder by two set screws. The tip holder block is then lowered carefully until the current amplifier registers a reading, then raised about a quarter turn on one of the three fine-pitch screws. The piezo stage should now be able to make contact with the tip when the program starts.

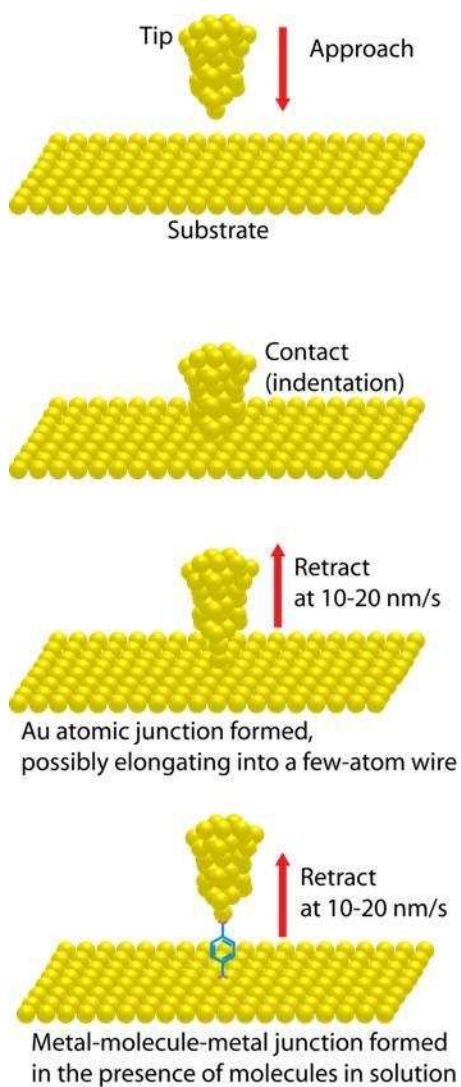
4.5 Sample preparation

To assemble a break-junction for conductance measurements, we use a tip freshly cut from 0.25 mm-diameter Au (99.999%) wire from Alfa Aesar and an oxidized Si chip with 100 nm of Au (99.999%) deposited by electron-beam evaporation as the substrate. The wire is cleaned in acetone, rinsed in isopropanol and cleaned in an O₂ plasma before cutting. With the wire segment secured in the tip holder and the substrate on the piezo stage, we deposit a small drop (~1 μL) of solution at the contact between the tip and substrate. We use 1,2,4-trichlorobenzene as the solvent for its high boiling point (214.4°C). The concentration of the solution varies from about 10 μM to 10 mM.

4.6 The measurement

The tip is biased at 25-100 mV and the current through the substrate is amplified with a DL 1211 current preamplifier (Ithaco) with appropriate gain settings (1 μA/V to 1 nA/V). The output of the current preamplifier is read by a National Instruments PXI-4461 card at 40 kHz. A series resistor is sometimes added in the circuit and taken into account in the data processing. The tip is moved by a piezoelectric actuator with data recorded as the tip is withdrawn from the substrate. Every conductance versus displacement trace in which the junction breaks completely (implemented as requiring $G < 5 \times 10^{-6}G_0$) is binned into conductance histograms with evenly spaced bins (*i.e.*, a linear scale). The measurement cycle is automated to allow us to measure thousands of traces for each histogram.

Figure 4.3: Pictorial representation of each measurement cycle: the Au tip is crashed into the Au substrate, then retracted to draw an atomic Au contact; when this contact breaks, a molecule in solution can be trapped within the gap, at which point molecular conductance is measured.



A brief description of iPiezo

We wrote a program called iPiezo in LabWindows to automate the measurement process. The original version allowed for motor control (serial controller), so most of that code is still in the program, but disabled. Also, at one point a Keithley was used as the voltage source, so there is Keithley GPIB control code which is also mostly disabled in the latest version. In the current experiment, in terms of software control, a measurement sequence goes as follows when the user clicks “Start”: the piezo stage moves in 1-nm steps checking at each step whether contact has been made (user-defined threshold); once contact has been made, a ramp-sequence is generated and sent to the output buffer to simultaneously retract the stage and acquire data at the user-defined frequency; it checks whether the last points acquired are below the “break” threshold – if not, the piezo is retracted in steps until contact is broken; if contact was broken, the trace is “good” and the entire trace is binned into the histogram, plots are updated and the trace is saved if the option is enabled; the cycle repeats with a step-wise approach to make contact; when the prescribed number of cycles has been run or if the user clicks “Stop,” the histogram is saved if auto-save was enabled at the start of the measurement.

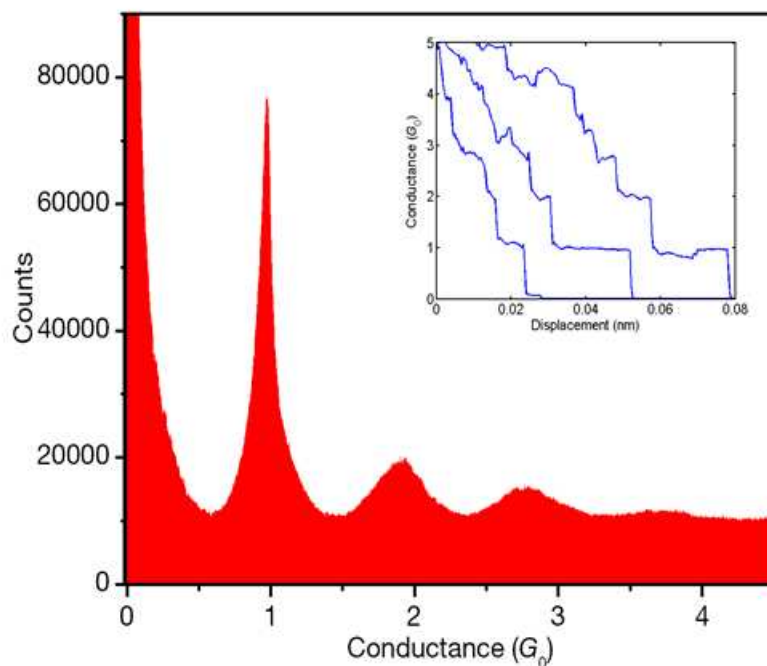
Two-dimensional histograms

To construct two-dimensional histograms as a function of both conductance and junction displacement [83], we first take each conductance trace and define as zero displacement the data point at which the conductance drops and remains below $1 G_0$. Each trace is then binned using a logarithmically-spaced conductance scale and a linearly-spaced displacement scale. Normalizing the counts

to the respective conductance bin widths recovers the histogram obtained with linearly spaced bins. Comparing histograms for molecular species to control histograms (bare Au electrodes) shows that the peak is not an artifact of binning. To roughly determine the peak conductance at each displacement value, we take a line cut at each displacement value and fit to the peak with a high-order polynomial.

4.7 Capability check

Figure 4.4: Conductance histogram of bare Au contacts. Inset: Sample traces, as a function of electrode displacement.



The first test of the apparatus is to measure the conductance histograms from bare Au electrodes. As expected, the histogram shown in Fig. 4.4 shows sharp peaks at conductance values of approximately integer multiples of G_0 . The most prominent “1 G_0 ” peak corresponds to conduction through a single high trans-

mission channel expected for a Au junction of single-atom diameter. In this simple measurement, we noticed that the noise in the histogram is far higher than one would expect based on counting statistics. It turns out that this is due to the differential nonlinearity in the ADC of the DAQ card [104]. This refers to the characteristic that the voltage bins of the ADC itself are not uniform in width, so even when measuring a uniformly distributed signal (*e.g.*, a sawtooth wave), a histogram of the signal will not be flat within counting errors. This nonlinearity is quite noticeable in our 16-bit DAQ card. As explained in Ref. [104], it is fairly easy to compensate for this effect – find the bin widths by measuring a uniformly distributed signal and normalize the corresponding bin in your data. In practice, we have not found it necessary to make this correction to get interpretable data.

Next, we tested the apparatus on several molecules for which results have been previously reported. Shown in Fig. 4.5a are conductance histograms for simple carbon chains terminated with amine groups. We extract the conductance for each molecule by fitting a Gaussian curve to the region near the peak. The conductance shows the expected exponential dependence on molecular length, as shown in Fig. 4.5b. The individual conductance values and the decay constant, 0.91 per methylene group, are in excellent agreement with those reported by the Columbia group [21]. From this measurement, we determined that we are able to measure down to a conductance of $1 \times 10^{-6}G_0$ (for 1,12-diaminododecane). At this conductance value, the Johnson current noise at room temperature with the acquisition rate as the bandwidth ($\Delta f = 40000$) is $\sqrt{4k_B T \Delta f / R} = 0.2$ pA, and at a bias of 100 mV, the signal would be 8 pA. The signal-to-noise ratio decreases as the resistance increases, which places a fundamental limit on the measurement.

Figure 4.5: a) Conductance histograms for several diaminoalkanes, $\text{NH}_2(\text{CH}_2)_N\text{NH}_2$. b) Conductance peak positions (extracted by Gaussian fits to each histogram shown in panel (a)) as a function of the number of methylene groups in the molecule. The black line is a linear fit to the logarithm of the conductance as a function of the number of methylene groups, yielding a conductance decay constant of 0.91 ± 0.03 per methylene group.

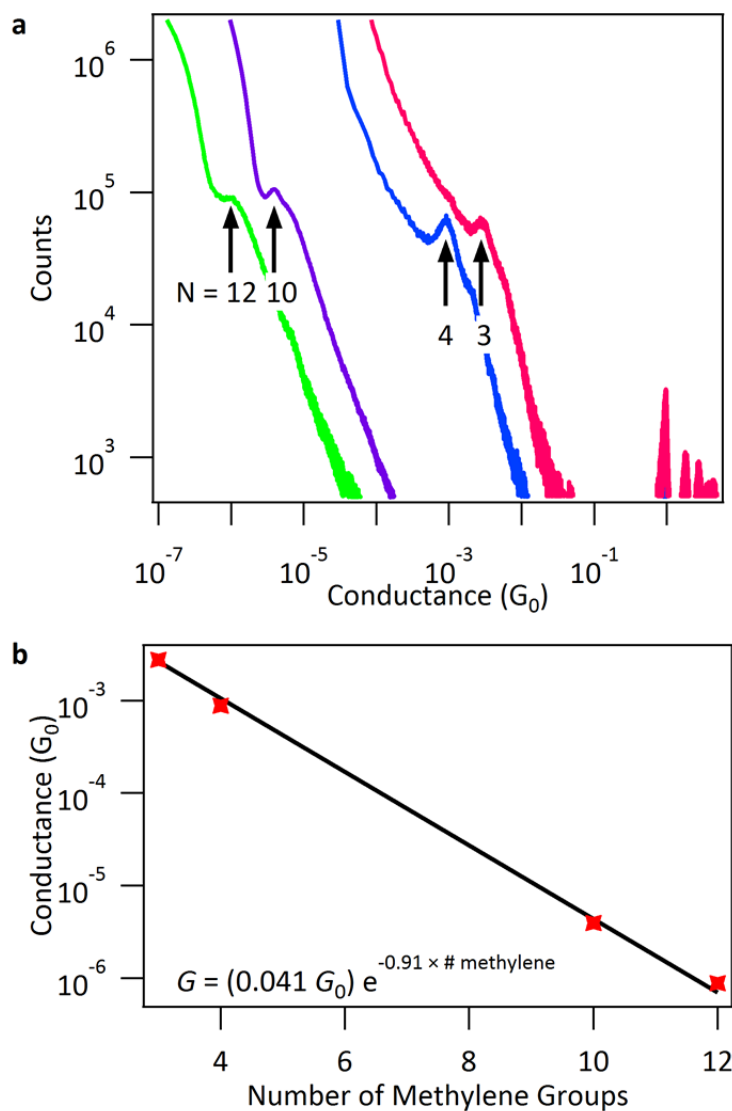


Figure 4.6: Conductance histograms (at least 3000 traces) for (a) 4,4'-bipyridine and (b) 1,2-bis(4-pyridyl)ethane. Insets show the same data on a linear scale with Gaussian fits, yielding conductance peak values at (a) $(1.7 \pm 0.1) \times 10^{-4} G_0$ and $(6.0 \pm 0.2) \times 10^{-4} G_0$ and (b) $(5.3 \pm 0.2) \times 10^{-6} G_0$ and $(1.0 \pm 0.1) \times 10^{-5} G_0$.

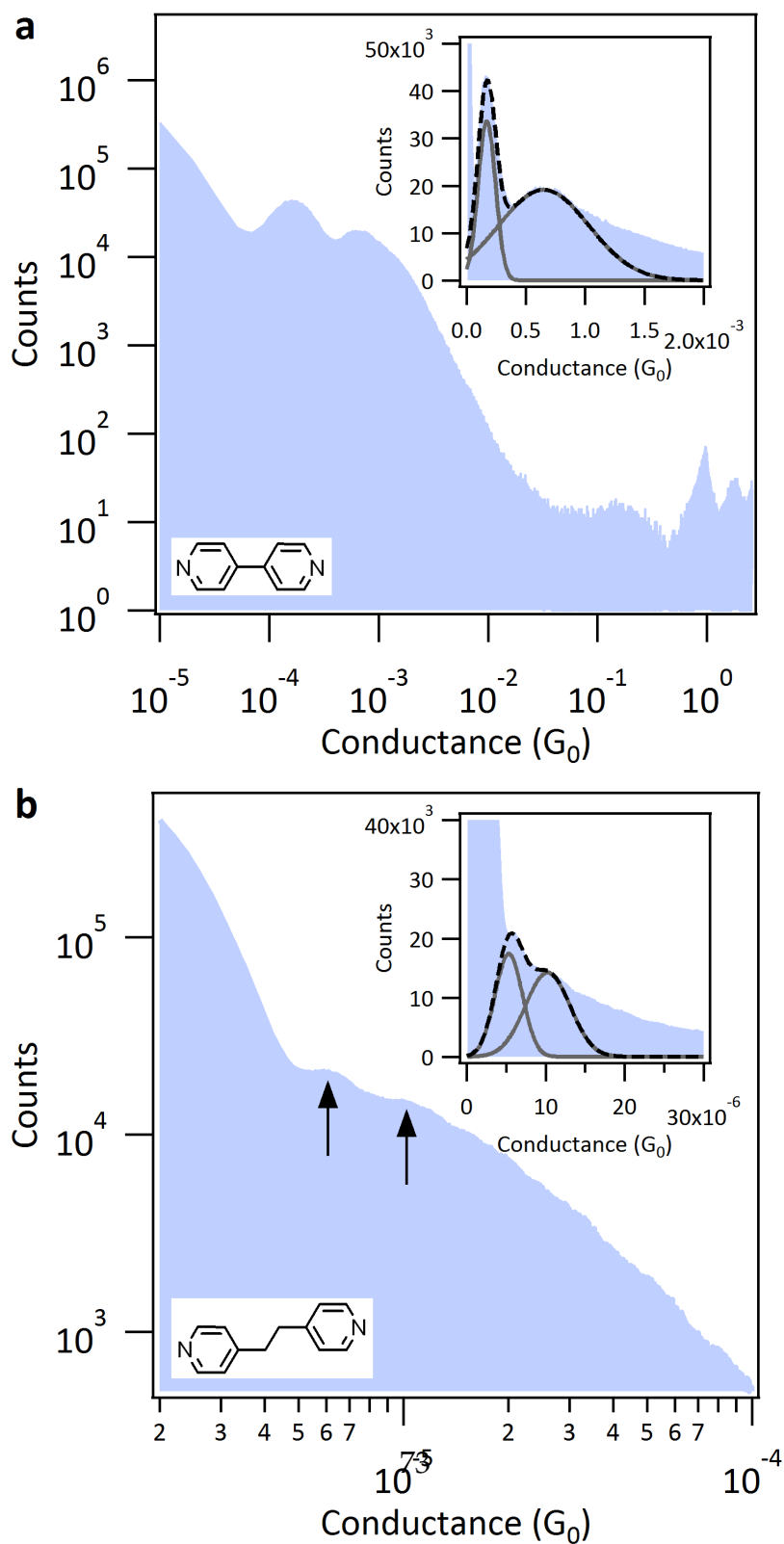
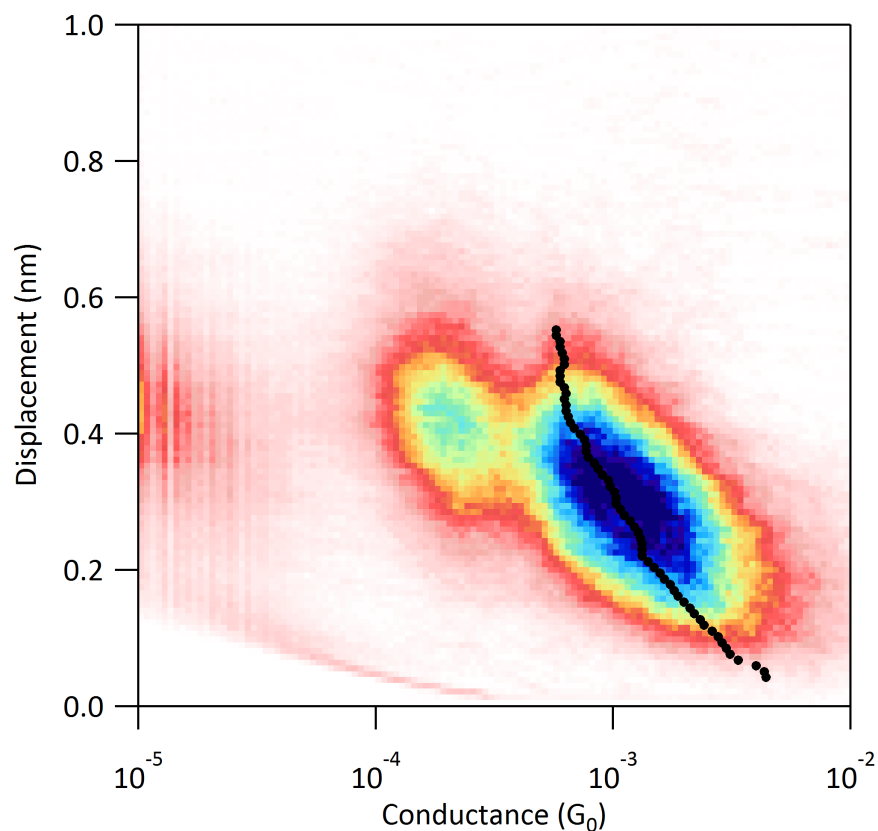


Figure 4.7: Two-dimensional histogram for 4,4-bipyridine from 5000 traces. Black circles mark the fitted peak conductance for each displacement value. Conductance bins are logarithmically spaced.



As another test, we measured two of the simplest pyridine-terminated molecules, 4,4'-bipyridine and 4,4'-bipyridyl-ethane. The work of the Columbia group [83, 105] has shown conductance histograms from pyridine-terminated molecules show double-peaks, interpreted as corresponding to two distinct contact geometries between the molecule and the Au electrode surfaces. Specifically, Ref. [83] identifies the lower-conductance (higher-conductance) peak at $1.6 \times 10^{-4} G_0$ ($6 \times 10^{-4} G_0$) with the molecule's long axis being more perpendicular (parallel) to the N-Au bond, which directly affects coupling of the molecular π -system with the Au s -orbital. In Ref. [105], they further investigated other simple molecules terminated with pyridines and find consistent results. Our data

for 4,4'-bipyridine and 1,2-bis(4-pyridyl)ethane, shown in Fig. 4.6, are in excellent agreement with Refs. [83] and [105]. It was found, in performing these test measurements, that the longer molecules required using very dilute solutions in order to achieve mostly-single-molecule junctions. Instead of ~10 mM that we typically use for molecules such as 4,4'-bipyridine, for the long carbon chains or for 1,2-bis(4-pyridyl)ethane, we dilute the solution 10- to 100-fold. Figure 4.7 shows a two-dimensional histogram constructed for 4,4'-bipyridine, and this again qualitatively agrees well with that in published work by Quek *et al.* [83].

4.8 Optical switch molecules – dithienylethenes

4.8.1 Introduction

In the development of molecular and nanoscale electronics, there is an active search for molecules whose electrical conductance is optically switchable, which could open the possibility of integrated opto-electronic devices. Especially promising are diarylethenes, a class of photochromic molecules that can reversibly change configuration back and forth between two different conductance states by irradiation with specific wavelengths of light [106] as well as by electrochemical methods [107]. The high-conductance conjugated isomer (hereafter referred to as the "closed" or **c** form) can be switched by visible light to the low-conductance un-conjugated isomer ("open" or **o** form). The reverse process occurs under ultraviolet (UV) irradiation. For applications in both thin-film solid-state devices and in single-molecule junctions, diarylethenes are particularly attractive because of their thermal stability, high fatigue resistance, and

sub-ångström difference in length between isomers [108]. This last characteristic is particularly important due to the strong dependence of conduction on junction length. In this chapter, I will describe the results we obtained by using the sewing machine on this class of molecules, published in 2011 [109].

Experimental approaches to investigate electronic transport through diarylethene derivatives have included mechanically controllable break-junctions, [110] self-assembled monolayers with macroscopic electrodes [111], scanning tunneling microscopy (STM) [112,113], attachment to single-walled carbon nanotube electrodes [114], and incorporation into metal nanoparticle networks [115,116]. Key findings include on/off conductance ratios ranging from 10 to 100 and the irreversibility of switching for certain derivatives when attached to Au electrodes. Ensuing theoretical analysis predicted the conduction to be HOMO-dominated with conductance on/off ratios ranging from 20 to several hundred, in reasonable agreement with experiment [117–120]. The calculated conductances varied, with some predictions for the closed forms of thiol-terminated derivatives as high as 0.6-0.7 G_0 [117,118] (where G_0 is the conductance quantum) much higher than the experimentally measured values which are on the order of $10^{-3} G_0$ [110,112]. However, conductance overestimation is common in density functional theory (DFT) calculations as we have discussed earlier in this chapter [90]. The irreversibility of open-to-closed switching of some derivatives when attached to Au electrodes was attributed to the much lower energy of the HOMO for the open form, so excited states are quenched by the coupling to a metallic reservoir. For reviews of the synthesis and properties of diarylethenes, see Refs. [106], [108], [121], and [122].

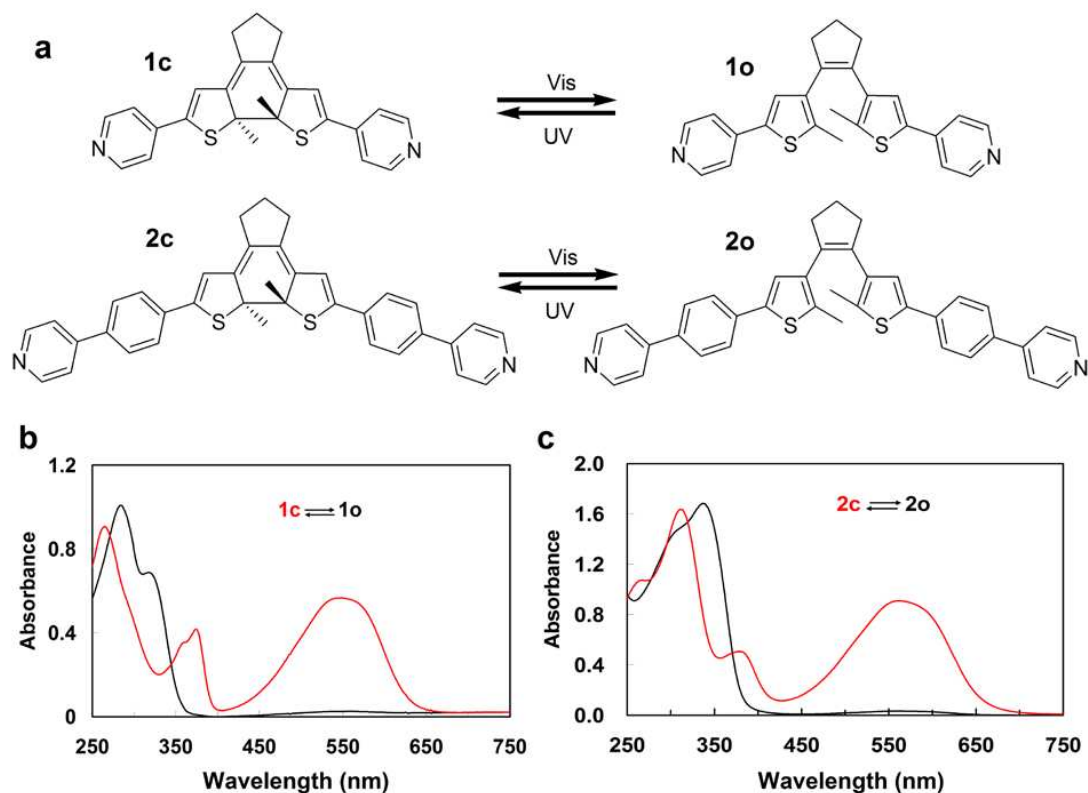
Previous studies of the conductance properties of diarylethenes have re-

ported results from a limited number of devices incorporating either individual molecules [110,113] or an ensemble of molecules [111,115,116]. Because fluctuations in the junction geometry can lead to exponential variations in molecular conductance, meaningful information can best be obtained statistically, *e.g.*, by repeated formation of molecular junctions [17,103]. A statistical study of a thiol-terminated dithienylethene derivative reported conductance values obtained from histograms constructed from a selected subset of traces for which a low-conductance plateau was evident [112]. However, recent work by Venkataraman *et al.* has shown that consistent and reproducible results can, in fact, be obtained without any data selection for molecules terminated with certain linker groups (including amine, phosphine, and pyridine) which yield well-defined conductance values, in contrast to molecules terminated with thiol and isonitrile end-groups [103]. Here, we report on measurements of the conductance of pyridine-terminated dithienylethenes without any trace selection, thus capturing the full range of possible junction geometries. We find a conductance value for the closed isomer **1c** (Fig. 4.8a) of $(3.3 \pm 0.5) \times 10^{-5} G_0$ and a lower bound for the on/off conductance ratio of 30. In contrast to simpler pyridine-terminated molecules [83,105], we observe that the closed dithienylethene isomer does not exhibit bi-stable conducting configurations due to two well-defined bonding motifs. We attribute this to the overlap of the conductance ranges for the two bonding motifs known for pyridine groups, as supported by DFT calculations.

4.8.2 Sample preparation

Yu-Wu Zhong from the Abruña group synthesized a family of dithienylethene-based molecules for these measurements, including compounds terminated

Figure 4.8: a) Molecules **1o/1c** and **2o/2c**. b,c) UV-vis absorbance of the two isomers of the molecules in (a).



with thiol, amine and pyridine end-groups. Thiol end-groups have the aforementioned problem of non-specific bonding, while amine end-groups resulted in molecules that were relatively unstable under UV irradiation. We therefore chose to focus on molecules with pyridine end-groups which are expected to bind well to Au electrodes and yield fairly well-defined conductances. Compound **2o** is designed with an additional phenyl spacer between the switch unit and each pyridine group, compared to compound **1o**. We were motivated to study this molecule by the report of reversible switching of a similar molecule when bound to Au electrodes in Ref. [113].

Figures 4.8b and 4.8c show the UV-vis absorption spectrum of the open and closed forms of molecules **1** and **2**. As prepared, the pale yellow solution

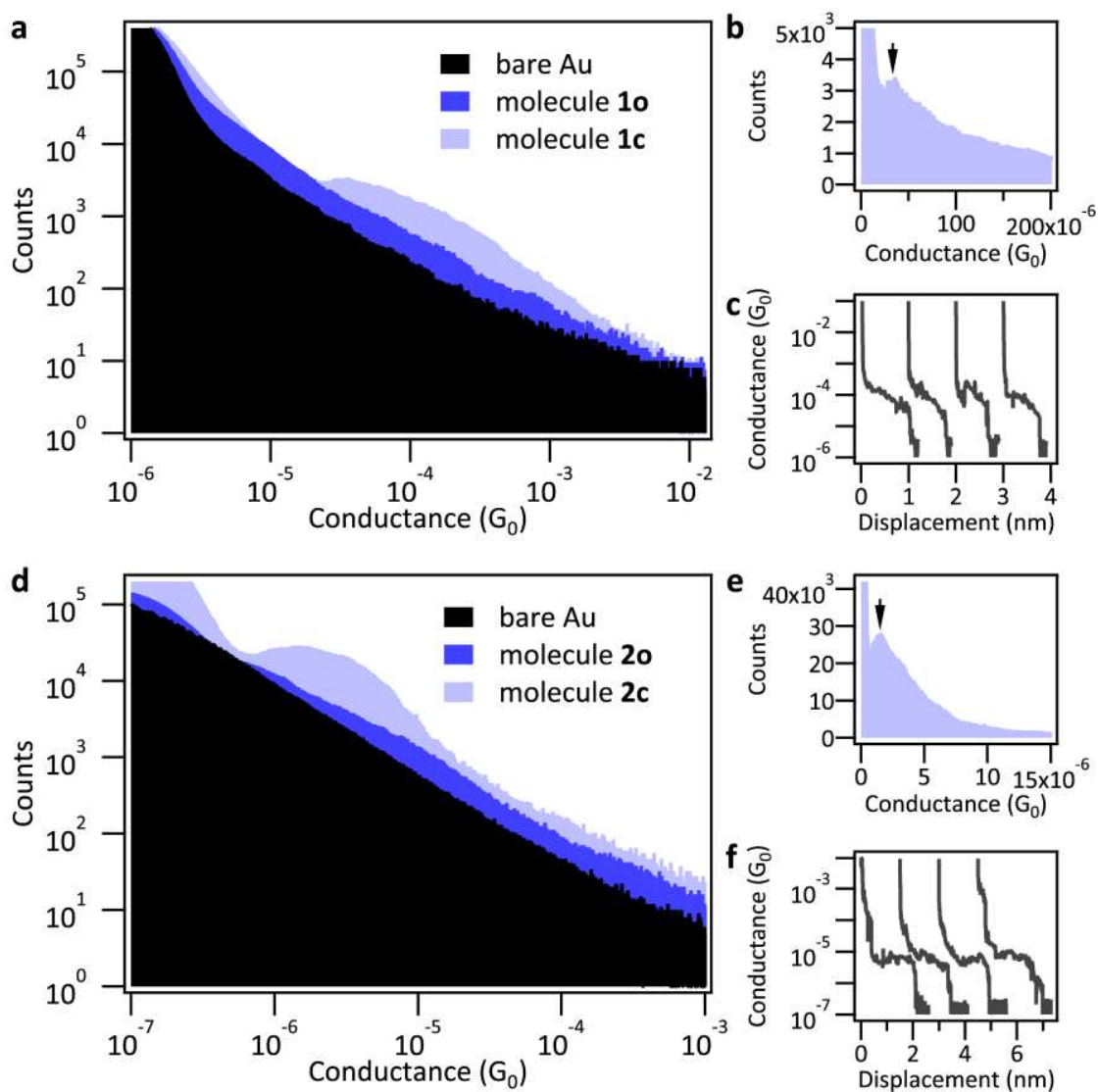
contains mostly molecules in the open form, showing negligible absorbance at wavelengths above 350 nm (black curves in Fig. 4.8b,c). After UV-irradiation with a single LED ($\lambda = 380$ nm; power density approximately $1500 \mu\text{W}/\text{cm}^2$) for 15 minutes, most of the molecules isomerize to the closed, conjugated form, and a prominent peak appears in the visible region of the spectrum (red curves). A solution of the closed isomer is dark purple. The reaction is reversible by irradiation at $\lambda = 500\text{-}600$ nm (green LED). The molecule appears to be not entirely stable under UV-irradiation because if left in UV light overnight, it turns dull clear yellow and no further opening/closing is possible.

With each of **1o** and **2o**, a <1 mM solution is made with 1,2,4-trichlorobenzene. A solution of the closed-form molecules is prepared by irradiating the open-form solution with a light-emitting diode centered at 362 nm ($1500 \mu\text{W}/\text{cm}^2$) for approximately 15 minutes. The conversion of the molecules to the closed form was verified by UV-vis spectroscopy.

4.8.3 One-dimensional histograms

Figure 4.9a shows overlaid conductance histograms in the range of 10^{-6} to $10^{-2} G_0$ for bare Au electrodes in pure 1,2,4-trichlorobenzene solvent and for Au electrodes in contact with solutions of dithienylethene derivatives **1o** and **1c**. The histograms are constructed from 1000 traces each with uniform bins of width $1 \times 10^{-6} G_0$, but are plotted on a log-log scale, for clarity, in Fig. 4.9a. The histogram for compound **1c** (closed isomer) shows a well-defined conductance peak not present in either the histogram for bare Au or compound **1o**. We fit the conductance peak for **1c** (Fig. 4.9b) to a Lorentzian function and find a junction

Figure 4.9: a) Conductance histogram for bare Au electrodes in pure solvent (black), molecule **1o** (dark blue), and molecule **1c** (light blue) plotted on a log-log scale. b) Isolated histogram for molecule **1c** on a linear-linear scale. Arrow indicates approximate peak location. c) Individual traces of conductance versus junction displacement for molecule **1c**. Plateaus in the $10^{-5} G_0$ range are clearly visible. (d)-(f): Same as (a)-(c), respectively, for molecule **2o/c**.

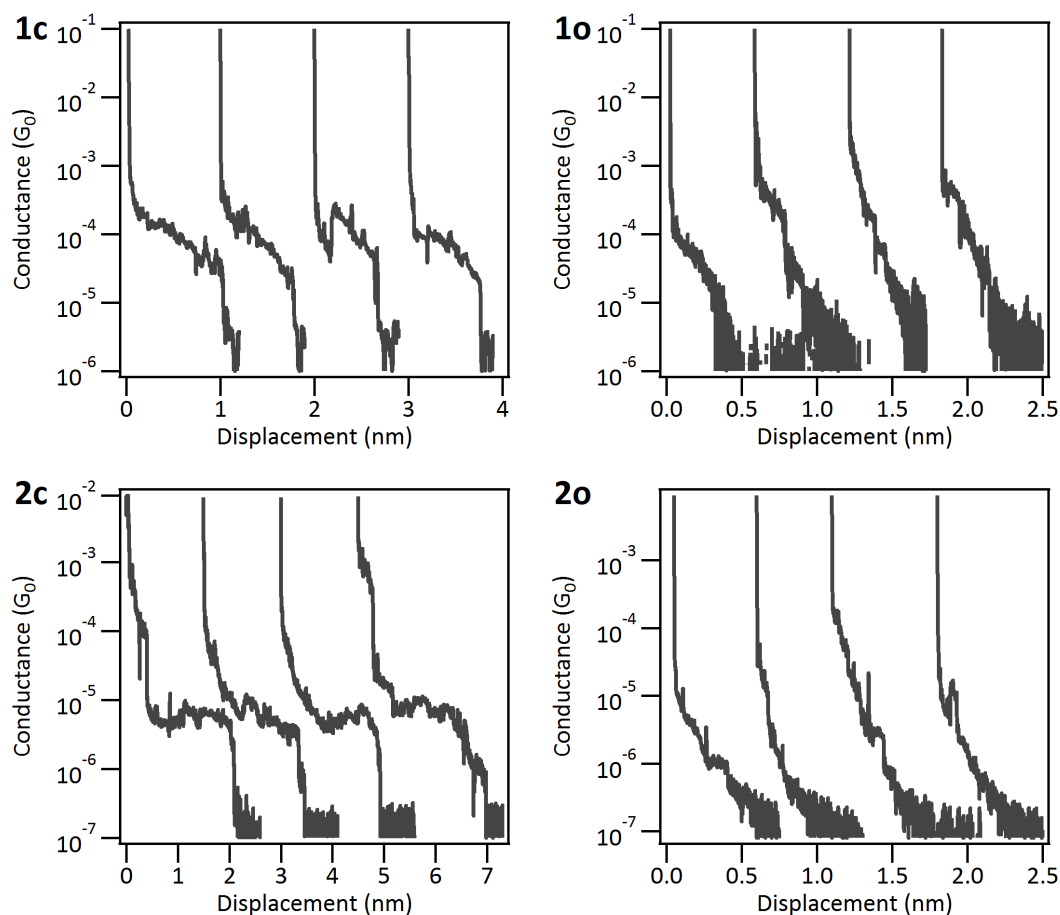


conductance of $(3.3 \pm 0.5) \times 10^{-5} G_0$. The peak is relatively broad (two orders of magnitude in conductance), suggesting contributions from a variety of different molecular geometries. This variability in geometry is also directly evident in the individual conductance *vs.* displacement traces like those shown in Fig. 4.9c. In most of the traces (over 70%), we see a clear sloping plateau with the conductance decreasing continuously as the junction is pulled apart, starting at values as high as $10^{-3} G_0$ and breaking abruptly in the $10^{-5} G_0$ range. We believe that this conductance plateau corresponds to the formation and elongation of a molecular junction. We interpret the histogram peak value to represent the most probable conductance of the fully stretched molecular junction. In contrast, for the open form of the molecule (**1o**) we were not able to measure a peak in the histogram above our conductance measurement limit of $10^{-6} G_0$. However, in the individual traces shown in Fig. 4.10 one can see that there is a measurable current in the **1o** junctions that decreases continuously to our noise level within a shorter displacement distance than the typical width of the conductance plateaus for **1c**, suggesting that the conductance of the fully stretched **1o** molecule is below our experimental noise floor.

Figures 4.9d-f show the corresponding data for compounds **2o** and **2c**, which have an additional phenyl ring between the central switching unit and each of the pyridine anchor groups. A Lorentzian fit to the peak in the histogram for **2c** (Fig. 4.9e) yields a conductance of $(1.5 \pm 0.5) \times 10^{-6} G_0$, which is 22 times smaller than that for **1c**. This decrease in conductance is in reasonable agreement with a naïve expectation based on previously reported results of conjugated molecules (specifically oligophenyldiamines) of a conductance decay constant of 1.7 per phenyl ring [103], which predicts a 29-fold decrease for two rings. We synthesized and measured compound **2o** to demonstrate the possibility of further

decoupling the switching unit from the electrodes. In the following, we mostly focus on a more-detailed analysis of data for compounds **1o** and **1c**.

Figure 4.10: Examples of individual conductance traces measured for the molecule species as labeled.



In Fig. 4.10, we show individual traces for the **1c/2c** and **1o/2o**. For each data set (thousands of traces), 10–20% of traces show an abrupt step from conductances on the order of $1 G_0$ to approximately noise level. These are likely associated with junctions in which the Au metallic contact breaks cleanly without forming a molecular junction. The traces we show in Fig. 4.10 are representative of 70–80% of the traces (depending on data set) which, from their conductance trend, we associate with the single-molecule junctions of interest. These types

of traces give rise to the histogram features seen in Fig. 4.9 (although all traces are included in constructing the histograms, with no data selection). A small percentage of traces show more anomalous behaviors of the types that might be associated with trace concentrations of the opposite isomer (*e.g.*, a closed molecule in the solution of open molecules) or multiple molecules in parallel within a junction. From the sample traces shown in Fig. 4.10, we note that although measurable current flows through both the open and the closed forms, there is a marked difference in the evolution of the conductance as the electrodes are pulled apart. For the closed forms (left panels), the conductance traces show a clear sloping plateau with both an abrupt beginning and an abrupt end, after which the current drops below noise level. In contrast, the sloping plateaus for the open forms (right panels) show a continuous decrease to noise level. This behaviour is also reflected in the two-dimensional histograms in Fig. 4.11 for the molecule **1o/1c**.

4.8.4 Comparison to past results

Although the dithienylethene derivatives that we employed are different from those in Refs. [110] and [112], it is worth noting that the conductance we measure for **1c** is two orders of magnitude less than the conductance values reported in those works (on the order of $10^{-3} G_0$ for the closed isomer). This disparity may arise from at least two differences between the experiments. First, the molecules studied in Refs. [110] and [112] are terminated with thiol groups, rather than pyridine groups. Thiols are known to form bonds to Au with strong coupling in a variety of motifs, while pyridines preferentially bind to under-coordinated atop sites [83, 123, 124]. Earlier work has reported conductance

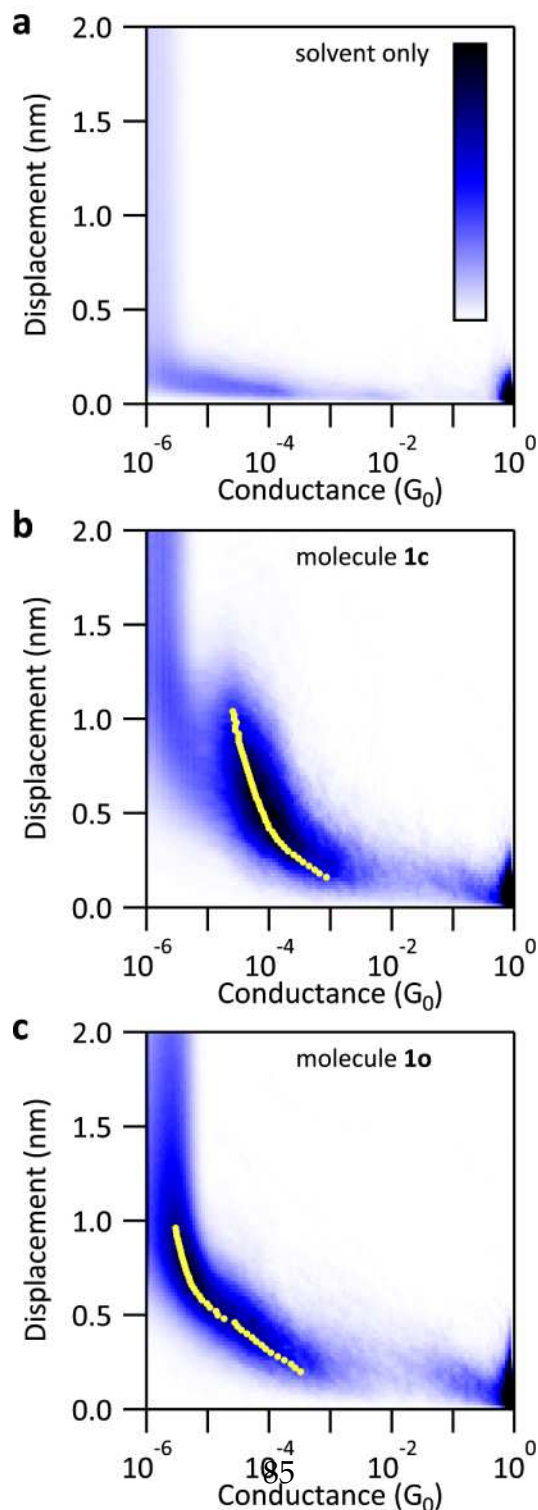
steps for 1,4-benzenedithiol junctions spanning the range from $10^{-5} G_0$ to as high as $10^{-1} G_0$ and no well-defined peak in the conductance histogram [21]. In contrast, benzene-based molecules with amine and pyridine end-groups yield histograms with relatively narrow peaks (with a peak width less than one order of magnitude) at lower conductances: 1,4-diaminobenzene shows a peak at $6.4 \times 10^{-3} G_0$ [21,125] and 1,4-bis(4-pyridyl)benzene shows two peaks in the $10^{-5} G_0$ range [105]. Second, our results represent the full range of geometric configurations, while the authors of Ref. [112] constructed histograms with a subset of traces that showed distinct plateaus, so it is possible that their measured conductance values represent the “high” range of conductance for the thiol-terminated dithienylethene molecules.

4.8.5 Two-dimensional histograms

To better understand the evolution and the range of conductance of our dithienylethene junctions, we constructed 2-dimensional histograms (binned in both conductance and in displacement) from our conductance data [84]. The displacement is measured from the point where the metallic Au junction first breaks so that the conductance drops below $1 G_0$, and the data are binned at 0.02 nm intervals. The three panels of Fig. 4.11 show data for bare Au in pure 1,2,4-trichlorobenzene solvent, and for compounds **1c** and **1o**, constructed from approximately 2000 traces each. All are plotted on the same color scale shown in panel (a). The conductance is binned logarithmically [83,84].

We note that binning logarithmically without normalization to bin width [126] is equivalent to multiplying the regular-bin histogram by the conductance

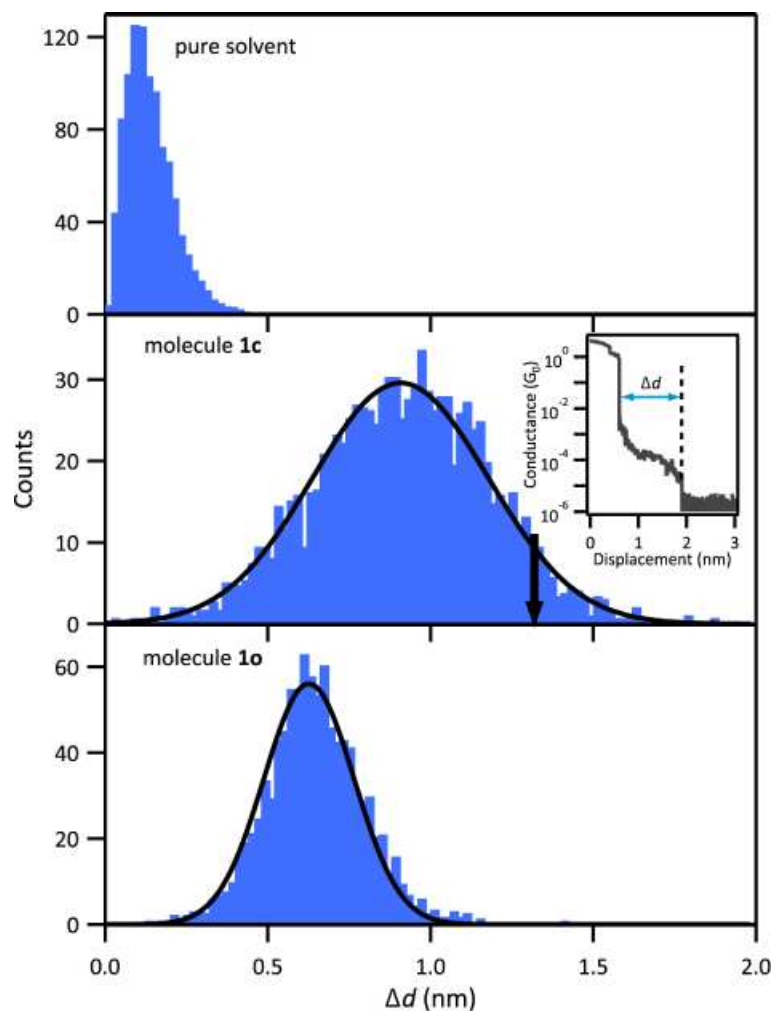
Figure 4.11: Comparison of logarithmically-binned (in conductance) 2-dimensional histograms for (a) bare Au junctions in pure solvent, (b) **1o** and (c) **1c**. The color scale (for counts) is linear and the same for all three plots. Counts are normalized to the number of traces. Yellow markers in (b) and (c) mark the peak position of the conductance histogram for each value of displacement (0.02 nm interval).



(with a multiplicative constant), since $dG = G d \ln G$, which distorts and shifts the peak towards a higher conductance. In fact, since the background for a histogram for traces with exponential decrease of conductance with distance is $1/G$, log-binning conveniently cancels out the background. Nevertheless, comparisons with histograms from bare Au electrodes (Fig. 4.11a) confirm that the peak feature in Fig. 4.11b is indeed associated with the molecule. Yellow dots in Fig. 4.11b,c mark the conductance with the highest count for each displacement value and show a clear trend of decreasing conductance as the electrodes are pulled apart. This suggests that a range of conductance values are sampled as the molecule evolves in the junction from an askew geometry to a fully stretched geometry. For comparison, in Fig. 4.7 we also see this same trend in conductance as a function of junction displacement for 4,4'-bipyridine.

Comparing the 2-D histograms of **1c** and **1o** (Fig. 4.11b,c, respectively), we see two key differences: (1) **1c** has a higher conductance than **1o** across the relevant range of displacement, and (2) the conductance feature for **1c** is separated from the noise (vertical feature at the left of the graph) whereas that of **1o** merges continuously with the noise band. As seen in the individual traces for **1o** (Fig. 4.10), there is measurable current immediately following the breaking of the Au metallic contact, but the conductance is significantly lower than that for **1c**, and the fully stretched **1o** junction conductance appears to be below the noise level of our measurements.

Figure 4.12: Histograms showing the distributions of the total displacement distance Δd (illustrated in inset) from the breaking of metallic atomic contact ($G < 1 G_0$) to the noise level of the conductance measurement. Counts are normalized to 1000. Black solid lines are fits to Gaussian functions. The black arrow in the center panel indicates the 95th percentile of this displacement distribution.



4.8.6 Total-displacement histograms

A complementary way of viewing of these results is shown in Fig. 4.12, which shows histograms for a quantity we call the total displacement distance, Δd , equal to the distance between the breaking point of the metallic junction ($G < 1 G_0$) and the point where the conductance drops below our instrumental noise

level ($G < 3 \times 10^{-6} G_0$) (see inset). Data are shown for Au electrodes in pure solvent (top panel), and with **1c** (middle) and **1o** (bottom). The distributions of Δd are much broader for junctions with molecules, with peaks at greater values of displacement compared to the bare Au junctions. This confirms the presence of open molecules (**1o**) in the junctions despite the lack of a distinguishable feature in the conductance histogram for **1o** in Fig. 4.9a.

As a reasonable estimate for the value of Δd for which the conductance of almost all of the **1c** junctions has fallen below noise level, we suggest taking the value of Δd at the 95th percentile, 1.32 nm (marked by a black arrow in Fig. 4.12b). (Counts that fall beyond this value in the tail of the histogram may correspond to junctions in which the Au electrodes lengthen atypically due to thermal motion or strain.) The distance between Au electrodes immediately after the breaking of the metallic junction (the snap-back distance) is known to be 0.65 ± 0.25 nm [74]. The sum of this snap-back distance and the 95th percentile Δd for **1c** is therefore 2.0 ± 0.3 nm, which is, within experimental uncertainty, equal to the calculated length of this molecule, 1.99 nm (calculations are discussed below). This is consistent with a picture where the conductance peak we measure for **1c** corresponds to the molecule in the fully stretched configuration. The same analysis does not apply in the case of **1o**, for which the sum is 1.5 ± 0.3 nm, significantly different from the calculated length of 2.03 nm. For **1o** junctions, we were unable to measure current above the noise level beyond about 1.5 nm of electrode separation, so this comparison provides confirmation that the conductance for the fully stretched configuration of this molecule is below the measurement limit allowed by our noise floor.

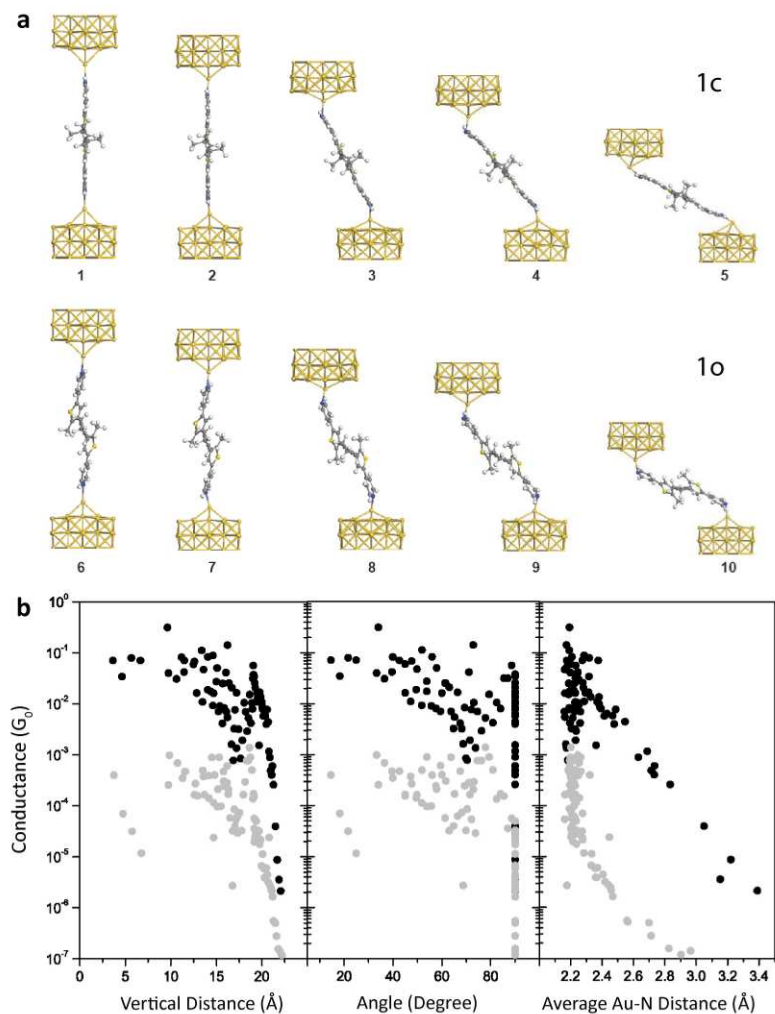
The Venkataraman group has shown previously that some simple pyridine-

terminated molecules exhibit bi-stable conductance, as we have discussed earlier in this chapter [105]. The low-conductance state is associated with the molecule being fully stretched between the Au electrodes. The high-conductance state is a few times more conductive and is associated with the molecule being held at an angle within the junction, thereby providing greater orbital overlap with the neighboring Au atoms. While our results on BPY and BPE show bi-stable conductance, consistent with the results reported, in our measurements of the pyridine-terminated dithienylethene derivatives, we observe only one broad peak with no sign of bi-stability.

4.8.7 Comparison to theory

Since there is no reason to expect the bonding to Au of the pyridine group of the molecule **1c** to be different from that of BPY and BPE, the observation of only a single peak for **1c** suggests that the range of the high- and low-conductance peaks overlap significantly such that they are not individually resolvable. To investigate this hypothesis further, we asked William Shum (presently: Hong Kong) and Garnet Chan (presently: Princeton University) to help us carry out a set of Kohn-Sham DFT calculations for **1o** and **1c**. They made use of the SIESTA package [127] with a custom implementation with help from Weitao Yang and Xiao Zheng at Duke University (Chemistry) [128]. They used the Perdew-Burke-Ernzerhof (PBE) generalized gradient approximation exchange-correlation functional. The atomic configuration was relaxed in two steps: first the isolated molecular structure is optimized with just a single Au atom at each end set at various angles and distances; then this structure is attached to Au[100] small-area electrodes. The top two layers of Au on each side (red atoms in Fig.

Figure 4.13: Conductance as a function of junction geometry obtained by density functional calculations on 182 relaxed molecular junctions. (a) Examples of molecular junctions with different electrode separations. 1 to 5 are examples for **1c**, and 6 to 10 are examples for **1o**. (b) Conductance of **1c** (black circles) and **1o** (gray circles) plotted against the electrode vertical distance, angle of the molecular junction, and N-Au distance.



4.14) and the molecule is allowed to relax in the next step of calculations to obtain the final geometry.

Figure 4.14: Simplified molecule-junction configuration used for geometry optimization. Au atoms in red are included in the relaxation; Au atoms in yellow are held fixed.

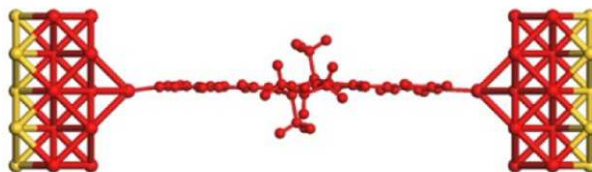


Figure 4.13a shows a sample of optimized molecular junctions included in the calculations. The full set included 182 such junction configurations corresponding to different electrode separations. To determine the conductance, several additional layers of Au were added (with no further optimization) and calculations were performed within a non-equilibrium Greens function DFT approach [129]. Figure 4.13b shows a scatter-plot of the conductances as a function of electrode separation, angle between the molecule and the electrode, and N-Au distance. Although the calculated conductance values are much larger than those found in experiment (due to well-known deficiencies in practical approximations to the functionals used to model conductance [94,95,129–131]), across a reasonable range of electrode separations we find that the conductance for **1c** is about two orders of magnitude larger than that of **1o**. This is consistent with our experimental limit for the on/off ratio. For the junction configurations considered, the calculated conductances vary smoothly with separation without any clear signs of bi-stability, again in agreement with our experimental findings.

From these calculations, we found that the Au-N bond distance is 0.224 nm for **1c** and 0.222 nm for **1o** (practically the same) and does not change significantly upon changing the inter-electrode distance. The compression is accom-

modated by the changing angle between the Au surface and the axis of the molecule, as shown in Fig. 4.13. The Au-N bond is stretched to 0.25 nm before it breaks (determined as when crossover of the energy of the connected molecular junction with the sum of the energy of the molecule itself and the unconnected junction).

4.9 Summary of the sewing machine experiments

In this work, we have independently confirmed the early results from Venkataraman *et al.* [21, 83, 105] using repeatedly-formed breakjunctions. We then applied this technique to the optically-switchable dithienylethene-based molecules **1o/1c** and **2o/2c**. Analyzing the data by one-dimensional and two-dimensional conductance histograms and also by displacement length histograms, we are able to determine the conductance for the fully stretched configurations of the closed forms of these two molecules, whereas the open form has much lower conductance and, in the fully stretched geometry, is beyond our measurement limit.

In the past few years, exciting results have come out, mainly from Columbia University, extending the limits of this technique. New endgroups have been found which are superior than those already mentioned (*e.g.*, amine, pyridine) in conductivity and/or stability. Unlike amines which oxidize over a timescale of hours in these experiments, diphenylphosphines have been demonstrated to be an air-stable alternative for linker groups [81]. Z.-L. Cheng *et al.* showed that the trimethyl tin (SnMe₃) endgroup on a molecule is actually displaced by Au atoms in the formation of a break-junction, and the resulting molecule-Au bond

is covalent and highly conductive ($\sim 0.09 G_0$ for a 4-carbon chain) [132]. Such developments motivate further improvement and addition of capabilities to the “sewing machine.”

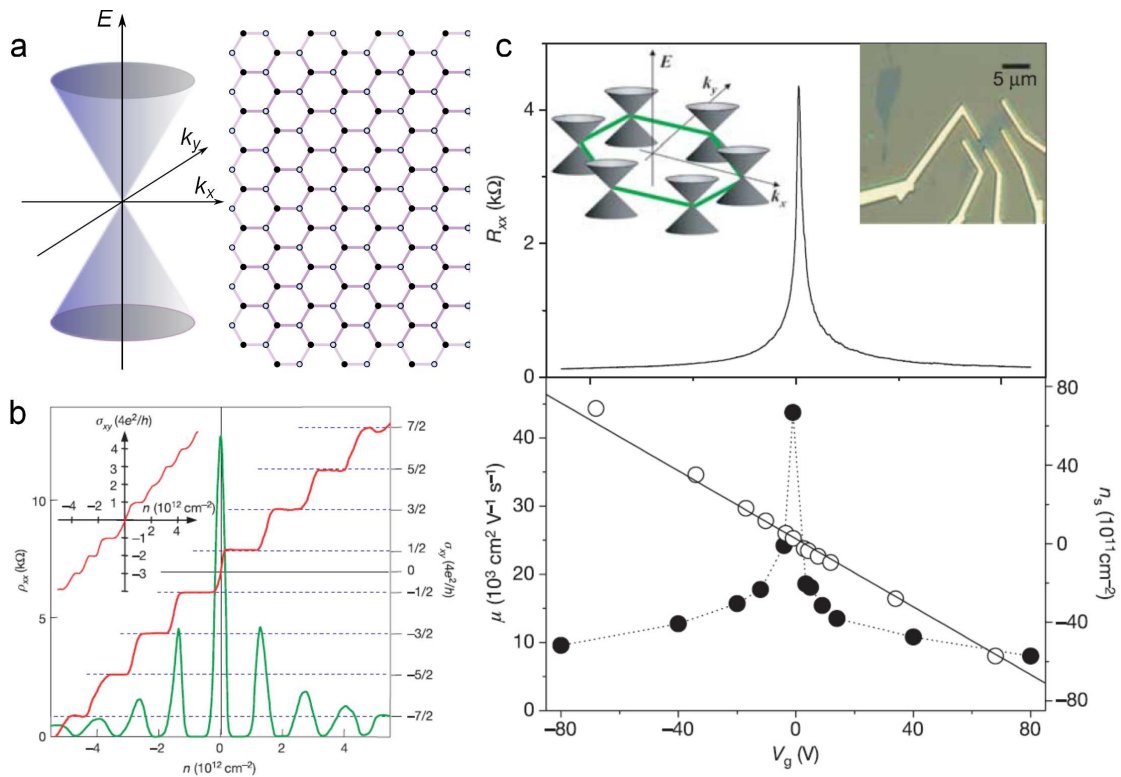
5.1 Introduction

In this chapter, I will discuss a project that is in-progress at the time of this writing, done in partnership with Wan Li of our group. The ultimate goal from the beginning is to efficiently inject spin current into graphene by the spin Hall effect. While we are still improving our devices for that purpose, along the way we have made some interesting measurements and developed a set of fabrication techniques which are described in this chapter. I first briefly introduce the two relevant subject areas — graphene and spin Hall effect — in “background” sections and then I explain our motivation for the project. In the second half of the chapter, I describe our fabrication process and preliminary measurement results.

5.2 Graphene

Graphene is a single layer of carbon atoms arranged in a two-dimensional honeycomb lattice. Though at first presumed to not be stable in this state as a 2D material, it was studied for decades as a model system and as a way to understand the properties of graphite [135]. The discovery of single layer graphene (SLG) as an isolated material in 2004 by Konstantin Novoselov, Andre Geim *et al.* led to their receiving the 2010 Nobel Prize for Physics [136,137]. Their technique of mechanically exfoliating highly oriented pyrolytic graphite (the “scotch tape

Figure 5.1: a) Low-energy $E(k)$, showing the linear spectrum of Dirac fermions, and the 2D honeycomb structure of graphene. Solid and hollow circles represent carbon atoms on the two equivalent A and B lattices, respectively. b) Data showing the quantum Hall effect for massless Dirac fermions from Novoselov *et al.* [133]. Inset shows data for bi-layer graphene, which exhibits QHE for massive Dirac fermions. c) Gate-dependence of resistance, mobility (solid circles) and carrier density (hollow circles) for SLG, from Zhang *et al.* [134]. Top right inset shows an optical image of a graphene flake contacted with electrodes.



method”) to obtain few layer graphene (FLG) on a substrate and then to identify SLG by the optical contrast when deposited on 280-300 nm silicon oxide on silicon has been widely adopted. Thus began years of very fruitful physics and engineering research on this zero-gap semiconductor with highly unusual properties, including but not limited to: high crystal quality from various production methods; high mobility even at high carrier concentration, which in turn can be widely tuned by gating; and exceptional mechanical strength and

thermal conductivity [135].

Figures 5.1b,c show data from two of the earliest works demonstrating the unusual properties of graphene due to its low-energy Dirac fermion spectrum $E(k)$ (Fig. 5.1a), here specifically the quantum Hall effect [133, 134]. It would be far beyond the scope of this chapter to even briefly review the enormous amount of progress in graphene research, which is of great interest both in terms of fundamental physics and potential carbon-based applications. I refer the interested reader to several excellent reviews and progress articles: Refs. [135] (progress to 2007), [138] (status and prospects to 2009), [139, 140] (electronic properties), and [141] (graphene for electronic and optical devices).

5.2.1 Graphene in spintronics

One potential use of graphene in the field of spintronics [142] is as a spin conserving medium due to its very low intrinsic spin-orbit coupling and low hyperfine interaction. The spin conservation property of a material is characterized by the spin relaxation time, τ_s , and the spin-flip length, λ_{sf} , which are the time and length over which the electronic spin is preserved, in diffusive mediums related by the diffusion constant, D , $\lambda_{sf} = \sqrt{D\tau_s}$.

For graphene, τ_s and λ_{sf} are predicted to be up to 10 μs and 100 μm , respectively [143–145]. Until very recently, experimental results have reported λ_{sf} of up to only about 1 μm and τ_s of up to ~ 100 ps from exfoliated and CVD graphene on substrates, but Dlubak *et al.* very recently reported $\lambda_{sf} > 100$ μm in epitaxial graphene on silicon carbide [33, 146–148]. Moreover, they measured an impressive non-local resistance (see below) of ~ 1 M Ω , four orders of magnitude

greater than previously reported. The progress that has come about in just a few years in improving graphene devices for spintronics bodes well for its potential for real applications.

Spin relaxation mechanisms

To improve graphene as a spin-conserving medium, researchers have naturally attempted to understand and distinguish between the causes of spin relaxation. In graphene spin relaxation can occur *via* the Elliott-Yafet (EY) mechanism and the Dyakonov-Perel (DP) mechanism, with the latter appearing to be dominant. The EY spin relaxation occurs when carriers scatter off impurities, even if the scattering potential is spin-independent, since the spin states are not perfect eigenstates of the band structure [149]. The relaxation rate due to EY mechanism is therefore proportional to the scattering rate. The DP mechanism plays a part in any material with broken inversion symmetry and changes the spin direction between scattering events [150]. In graphene, the Rashba spin-orbit coupling due to the presence of a substrate and/or gate voltage and due to ripples can contribute to DP-type relaxation. Earlier studies of the dependence of τ_s on momentum scattering time τ_e found at low temperatures a positive linear relation in SLG and an inverse relation in BLG (bilayer graphene), and therefore concluded that in SLG the EY mechanism is dominant while in BLG the DP mechanism is dominant [147, 151]. It is clear from the effect on τ_s of the tunnel barrier quality that the effect of the contacts is large on spin relaxation. More recent work has found that the spin relaxation in epitaxial graphene on SiC is so low that the value of λ_{sf} is largely determined by the tunnel barriers [148]. Further investigation of spin relaxation in graphene (exfoliated, CVD, epitaxial)

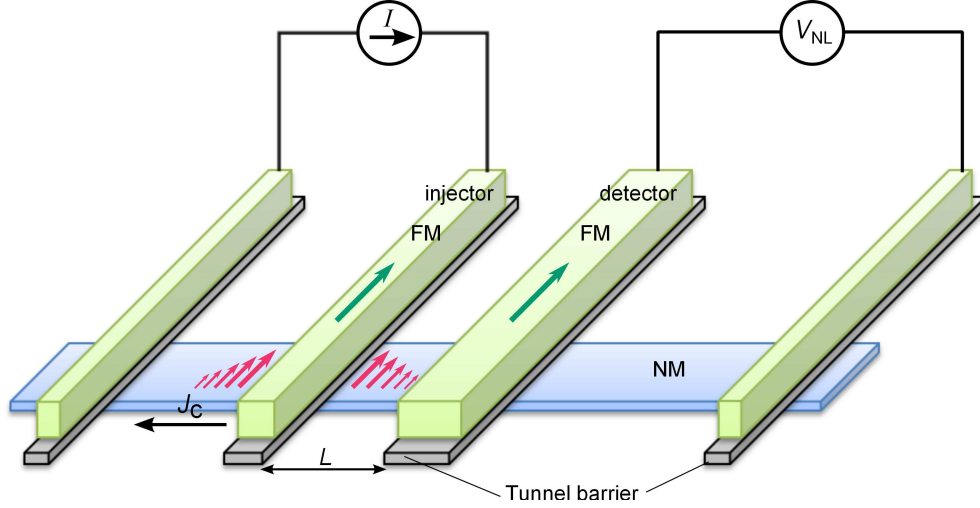
is clearly needed.

Spin injection and detection

Spin injection and detection in exfoliated graphene was observed at room temperature by Nikolaos Tombros *et al.* in Ref. [33] in 2007. To reduce spurious magnetic signals, they adopted a standard non-local geometry [152], similar to that shown in Fig. 5.2, where graphene is the non-magnetic (NM) material. The caption of Fig. 5.2 describes the injection and detection configuration. The detection circuit is (1) not in the path of the charge current and (2) sufficiently close (distance L) to the injection electrode that spin imbalance in the graphene is non-zero [153]. The FM electrodes (Co, in most cases for graphene experiments) are tunnel-coupled to the graphene through oxide barriers to enhance spin injection and reduce spin-current sinking at the detection electrode. Spin injection is enhanced because the tunneling resistance from an FM is large and spin-dependent, dominating over the spin-independent resistance of the semiconductor (here graphene), thereby overcoming the so-called conductivity mismatch problem of spin injection into semiconductors [33, 154, 155].

In non-local measurements of this type, the spin transport is typically characterized by the non-local resistance, defined as $R_{NL} = \Delta V_{NL}/I$, where $\Delta V_{NL} = V_P - V_{AP}$ is the difference in the non-local voltage when the injector and detector are parallel (P) and anti-parallel (AP), and I is the injected current. To determine τ_s and λ_{sf} , one can study the dependence of R_{NL} on L for a series of devices with different L , but a more robust method is to measure the precession of the injected spin as a function of an applied perpendicular field, B_{\perp} , known as Hanle precession [153]. Spins precess around B_{\perp} with the Larmor frequency

Figure 5.2: Non-local spin injection and spin detection geometry. The ferromagnetic electrodes (FM) are separated from the non-magnetic spin-conserving material (NM) by a tunnel barrier. Charge current flows through the left two electrodes, inducing an excess of up-spin under the injector electrode. The spin imbalance (small pink arrows on NM) decays spatially with λ_{sf} as the decay length. If the voltage detector electrode is close enough to the injector, it will detect a voltage with respect to the farther reference electrode, the sign of which depends on the alignment of the magnetization of the FM electrodes.

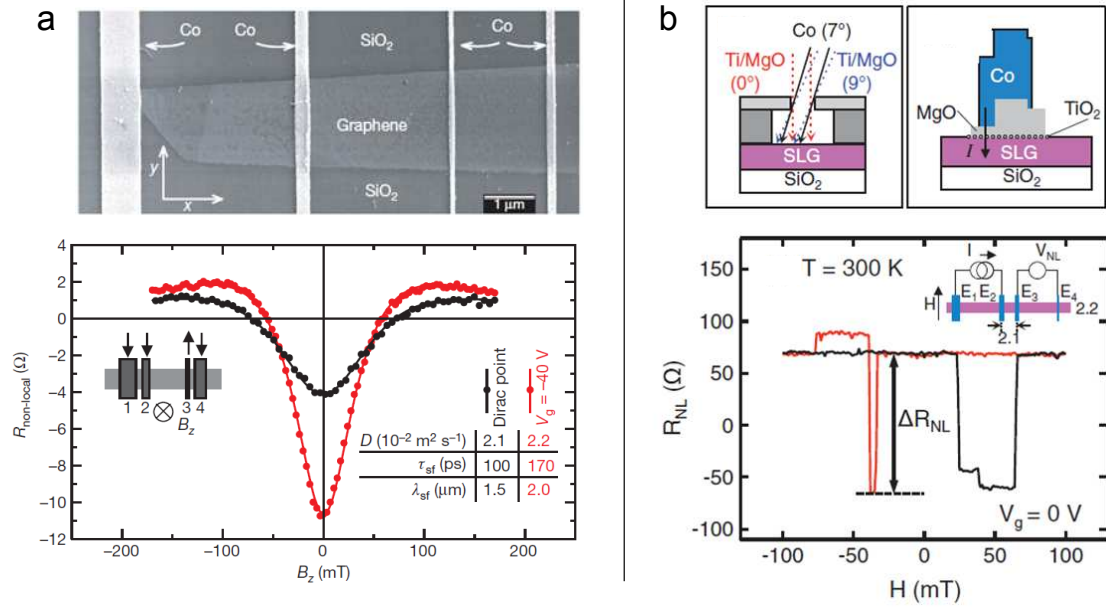


$\omega_L = g\mu_b B/\hbar$. With the injector and detector in P or AP alignment, the magnitude of the non-local voltage would decrease with applied magnetic field as the spins “arriving” at the detector precess away from the aligned direction. For a 1-D channel, the R_{NL} vs. B_{\perp} curve can be fit to the following to obtain the relaxation parameters [156]:

$$R_{NL} \propto \int \frac{1}{\sqrt{4\pi Dt}} \exp\left[-\frac{L^2}{4Dt}\right] \cos(g\mu_B B_{\perp}/\hbar) \exp(-t/\tau_s) dt.$$

Ref. [152] provides an excellent review of nonlocal spin injection/detection measurements and the spin Hall effect. It is with this type of non-local resistance measurement that Refs. [33], [146] and [147] (Fig. 5.3) determined the spin transport characteristics of graphene, experimentally obtaining τ_s of up to ~ 500 ps and λ_{sf} up to ~ 1 μm .

Figure 5.3: a) From Tombros *et al.* [33]. Top: SEM image of the graphene device with Co electrodes. Bottom: Hanle precession at two different gate voltages. b) From Han *et al.* [146]. Top: Fabrication and device design scheme. Bottom: Non-local magneto-resistance for field applied parallel to FM easy axis. The abrupt changes in R_{NL} correspond to the switching of each FM electrode.

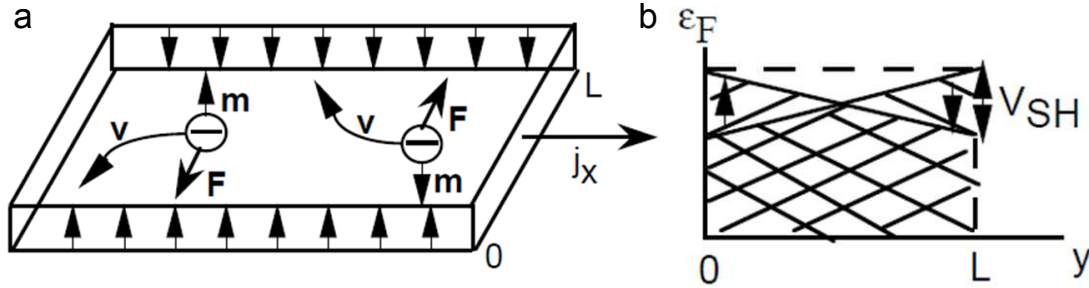


5.3 Spin Hall effect

In this work, we propose to use the spin Hall effect (SHE) to inject spin current into graphene. The SHE was first described by Dyakonov and Perel in 1971 for semiconductors, and further developed with a proposal of experimental realization by Hirsch in 1999 [157, 158]. As shown in Fig. 5.4, in a material with spin-orbit coupling, the scattering of electrons is spin-dependent, such that a charge current J_c (denoted J_x in the figure) generates a pure spin current J_s in a perpendicular direction. The spin moment $\hat{\sigma}$ and the spin current direction are also perpendicular:

$$\vec{J}_s \propto \vec{J}_c \times \hat{\sigma}.$$

Figure 5.4: Both figures are from J. E. Hirsch [157]. a) Generation of spin accumulation by a charge current J_x in a spin Hall material. Spin(\mathbf{m})-dependent scattering (\mathbf{F}) causes opposite net drift velocity in the transverse direction (\mathbf{v}) for each spin. b) The spin imbalance in the transverse direction induces an opposite gradient in the chemical potential for opposite spin directions. The difference between the chemical potential of up- and down- spin carriers is the spin Hall voltage.



The generated spin current density $(\hbar/2)J_s/e$ is related to the charge current density by the spin Hall angle, θ_{SH} : $J_s = \theta_{SH}J_c$. The reverse is also true, which is the inverse spin Hall effect (ISHE) — a spin current generates a charge current in a direction perpendicular to the spin and to the spin current direction. The conversion rate is the same spin Hall angle, $J_c = \theta_{SH}J_s$, in accordance with Onsager's relation. Both intrinsic and extrinsic mechanisms have been proposed for the SHE. In intrinsic SHE, the crystal structure of the material leads to spin splitting in the band structure [159, 160]. Extrinsic SHE arises from spin-dependent scattering off impurities because of spin-orbit coupling [157, 158].

The first experiments to demonstrate the SHE were optical measurements of spin accumulation at the edges of semiconductor channels by Kerr rotation [161, 162]. Electrical detection of the inverse spin Hall voltage was achieved in a diffusive metal (Al) by injecting a diffusive pure spin current from a ferromagnetic electrode through a tunnel barrier [163]. Interestingly, much about the SHE is currently still under debate, including the primary mechanism and

the value of the spin Hall angle [164–168]. Recent work by Luqiao Liu from the Buhrman group has directly addressed the latter “controversy” in the case of Pt, a material that has been intensely studied [169–171]. Liu *et al.* showed by analyzing the shape of spin-torque ferromagnetic resonance curves that in Pt the spin Hall angle is at least 0.06, and the spin current generated can induce precession of the magnetic moment in an adjacent layer [167, 172]. Soon after, they quantified the spin Hall angle of β -Ta to be 0.12 to 0.15, which makes this material very promising for potential applications [173]. This series of recent work on the spin Hall effect has sparked interest within our group in understanding it and exploring its application in other device geometries, which leads us to the topic of this chapter — spin injection into graphene by the spin Hall effect. We chose to work with Pt instead of Ta because of oxidation issues with Ta, which would complicate the fabrication process with graphene.

Shunting corrections

When attempting to inject spin current from a spin Hall material (say, Pt) into an adjacent material (say, Cu) by passing charge current through the spin Hall material, it is important to consider the distribution of the current between the two layers. In the case of Cu and Pt, as explained in Ref. [168] (a review of SHE measurements in Pt), the conductivity of Cu is an order of magnitude higher than that of Pt, so for layers of comparable thickness, most of the current flows through Cu where it generates no spin current. Furthermore, the contribution of the charge current to the spin current injected into the adjacent layer decays away from the interface with a length scale of λ_{sf} (typically a few nanometers in materials with significant SHE), so it is the current density near the interface

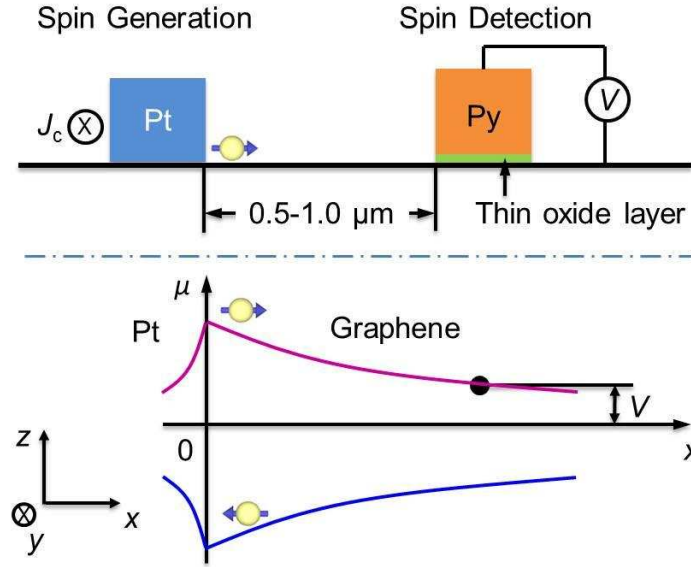
in the SH material that matters. Refs. [174] and [166] introduced procedures to correct for this shunting effect, and the adequacy of this correction is discussed in Ref. [168].

For the ISHE, one also has to consider a shunting effect that would decrease the signal (the potential difference due to charge accumulation generated by a spin current). The spin imbalance and therefore the spin current decays exponentially away from the source, with a length scale of λ_{sf} . In Pt, Ref. [168] argues that λ_{sf} is on the order of a few nanometers. If the thickness of Pt is greater than λ_{sf} , the ISHE potential will be reduced by the backflow of current in the portion of the material where there is zero spin current, by a factor that can be roughly approximated by the ratio of the spin-current-generating area to the whole cross-sectional area. For this reason, to maximize the ISHE signal, one ought to keep the Pt cross-sectional dimensions (thickness and width) as close to λ_{sf} as fabrication processes allow.

5.4 Device geometry

In our device geometry shown in Fig. 5.5, a Pt wire is in direct contact with the graphene, while a ferromagnetic (FM) detector electrode is coupled to the graphene through a thin oxide layer. A charge current driven through the Pt wire in the longitudinal direction generates spin current in perpendicular directions. Because of the lower density of states in graphene, most of the spin current generated by the SHE is not transmitted into the graphene but instead builds up a spin-dependent chemical potential at the interface, which generates a backflow of spin current (shown in the bottom half of Fig. 5.5). The total spin

Figure 5.5: Top half: Device schematic showing the direction of the charge current J_c in the Pt wire and the detection of a voltage on a ferromagnetic electrode in close proximity. Bottom half: The corresponding chemical potential



current for up-electrons is the sum of the spin Hall-generated component and the diffusive component:

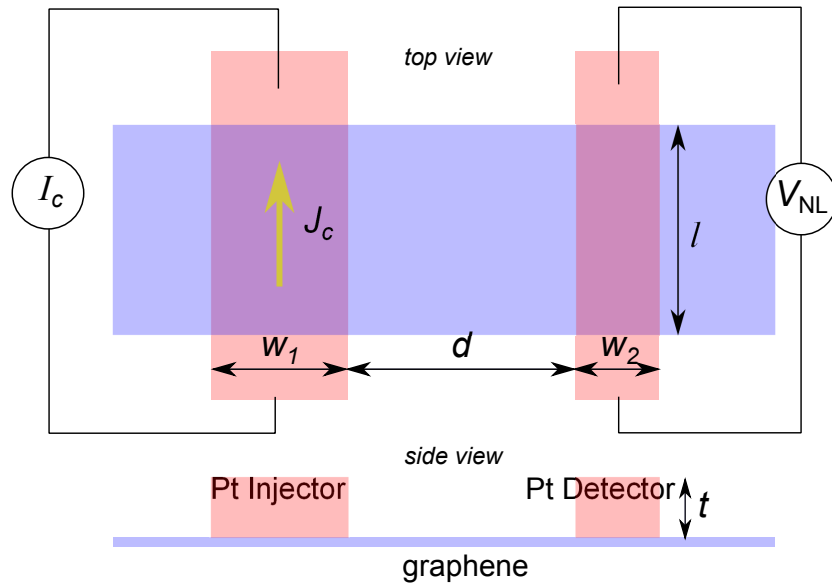
$$J_{\uparrow, \text{total}} = J_{\uparrow, \text{SHE}} - \frac{\sigma_i}{e} \frac{d\mu_{\uparrow}}{dx}$$

where σ_i is the conductivity of the material in question. The chemical potential in graphene must match that of Pt at the interface, so the chemical potentials for spin-up and spin-down electrons are split in graphene as well. This represents a spin imbalance in the graphene that decreases away from the interface with a decay length of λ_{sf} . At the FM permalloy ($\text{Py} = \text{Ni}_{80}\text{Fe}_{20}$) detector placed 0.5–1.0 μm away from the Pt wire, a spin voltage will be detected, $V_{\text{NL}} \propto \Delta\mu_s \vec{M} \cdot \hat{\sigma}$, where \vec{M} is the magnetization of the detector electrode, $\Delta\mu_s = \mu_{\uparrow} - \mu_{\downarrow}$, and $\hat{\sigma}$ is the direction of the spin imbalance at the detector [153]. Consequently, the standard Hanle precession geometry would require that the easy axis of the defined FM electrodes be perpendicular to the Pt wire (presumably the direction

of the spin, as illustrated in Fig. 5.5). While not impossible, it is much easier to fabricate parallel Pt and Py wires, so we have chosen to define them in a parallel geometry and therefore expect the V_{NL} vs B_{\perp} curve to be the asymmetric analogue to the standard Hanle symmetric peak shape [153].

With a simple 1-D drift-diffusion model and continuous boundary conditions at the interfaces, we calculated an estimate for the expected V_{NL} to be on the order of $10 \mu\text{V}$, assuming the following device parameters: $\lambda_{\text{sf}}^{\text{Pt}} = 5 \text{ nm}$, $\lambda_{\text{sf}}^{\text{gr}} = 2 \mu\text{m}$, $\sigma_{\text{Pt}} = 2 \times 10^6 (\Omega\text{m})^{-1}$, $\sigma_{\text{gr}} = 2 \times 10^{-3} (\Omega)^{-1}$, $\theta_{\text{SH}} = 0.07$, $J_c = 4 \times 10^{11} \text{ A/m}^2$, separation of Pt and FM electrodes $d = 500 \text{ nm}$, and a detection efficiency of 30% for the FM tunnel contact.

Figure 5.6: Drawing of the device geometry for detection of spin current by the ISHE, showing the top and side views. Calculations described in the text were done assuming the following: $d = 200 \text{ nm}$, $t = 5 \text{ nm}$, $l = 4 \mu\text{m}$, $w_1 = 70 \text{ nm}$, $w_2 = 25 \text{ nm}$, and the same material parameters as described for the FM detection scheme calculation.



Another geometry that we have considered using is simply two parallel Pt wires (Fig. 5.6), one as the “injector” as above, and the other as a detector, by the ISHE. The signal (voltage across the detector wire) is limited by: maximum

current density through the injection wire ($\sim 10^{11}$ A/m²), the thickness of evaporated Pt required for continuity (~ 5 nm), and the minimum size we can define by e-beam lithography for lift-off (~ 25 nm). Assuming the parameters in the caption of Fig. 5.6, with a simple 1-D drift-diffusion model calculation taking into account the shunting effect on the detector side, we calculated for maximum current density an expected signal of 4 μ V. The difficulty in measuring this signal arises mainly from a large background voltage from finite current flow through the detector wire driven by the voltage applied across the injector. The signal to background ratio is expected to be as low as 1/10000. Therefore, we have focused on detection by FM electrodes.

5.5 Device Fabrication

5.5.1 Graphene growth and processing

We grew single layer graphene on copper foils using the First Nano Furnace. The recipe that we use has not been optimized but the Raman spectra on the resulting graphene (Fig. 5.7) indicates predominantly single-layer graphene with decent quality. After a one-hour anneal in H₂ gas (0.01-0.02 L/min) at 1000 °C, methane gas is flowed at 6 sccm for 20 minutes in the growth step at the same temperature. The cool-down occurs over about an hour in H₂ gas with an Ar purge at the end. We spin PMMA (typically 495K A4) on the graphene-covered foil as a support layer and etch away the copper in ferric chloride. We transfer the PMMA/graphene membrane through at least 6 baths of high purity (chemical grade or Milli-Q) water to wash off the etchant (Transene CE-100). The

Figure 5.7: Raman spectra of transferred CVD graphene on SiO₂/Si substrate. Note the significant change upon further rinsing of the graphene before the transfer. Inset shows an optical image for a growth in which the bilayer areas were particularly prominent.

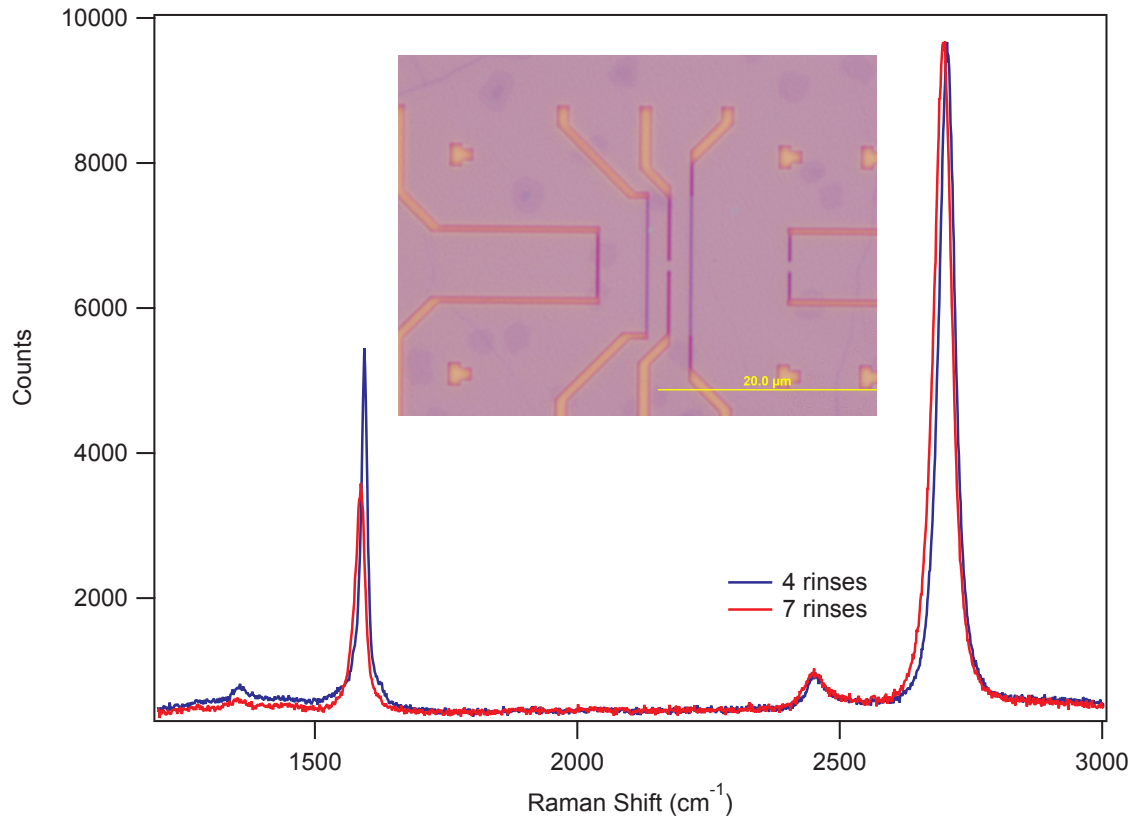
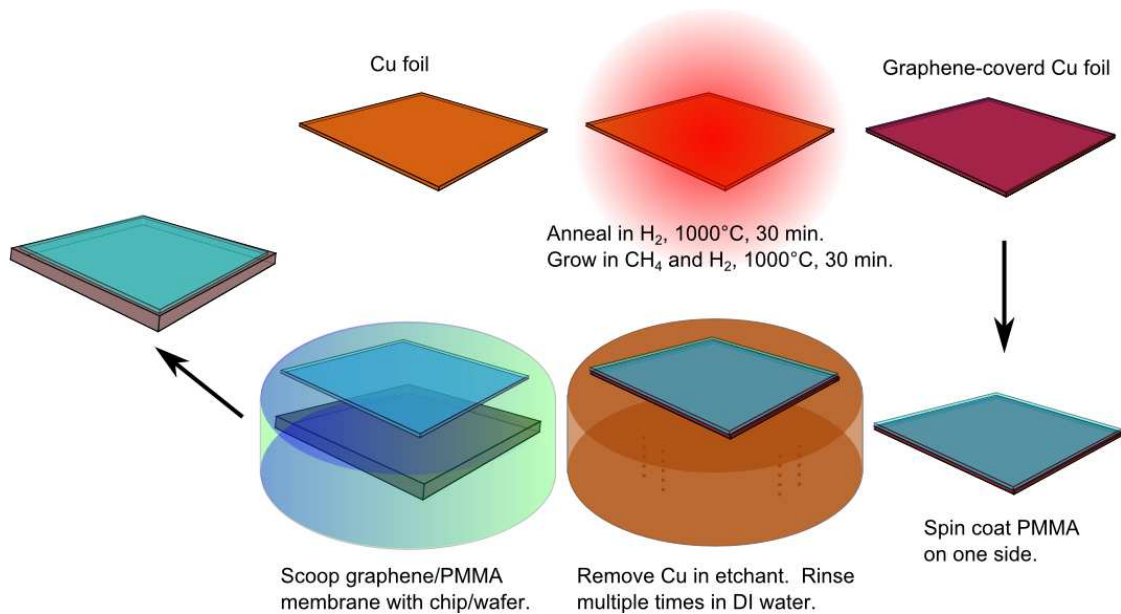


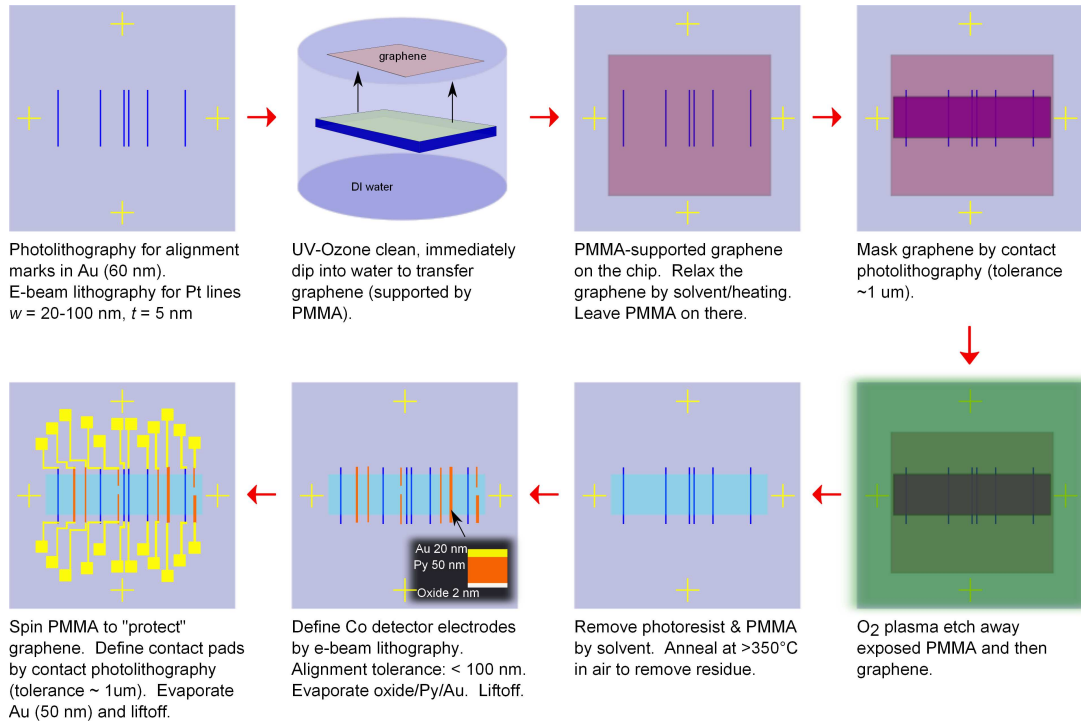
Figure 5.8: Graphene growth and transfer process steps.



PMMA membrane floating on water is then ready for transfer to a substrate. For optimal optical contrast for few-layer graphene, we use silicon substrates with 300 nm silicon oxide for all of the fabrication described in this thesis.

5.5.2 Lithography steps

Figure 5.9: Outline of steps in the fabrication process.



Alignment marks were put down with the ASML stepper and Au evaporation/liftoff over an entire 4-inch wafer. We then use the JEOL6300 with both global and chip alignment marks to define 20-100 nm wires in PMMA 950K (or 495K) A4 resist. The design width for the thinnest wires is 4 nm, but with a dose of about $2700 \mu\text{C}/\text{cm}^2$ and using the 5th lens, the features come out to be at least 20 nm. We evaporated Pt using the CNF evaporator because the Sharon evaporator places the source too close to the sample and, without cool-

ing, the evaporated samples came out with cracked resist. We did not have any issues with the CNF evaporator although the purity of the Pt is questionable. We found that 5 nm of Pt is sufficient to give a continuous film. On the other hand, we notice some of the thinnest wires (~20 nm) are sometimes not continuous, indicating that the dosage was just marginally sufficient. In our early rounds of fabrication, we cleaned the surface of the Pt wires with an O₂ plasma clean before transferring graphene. The resulting contact resistance was on the order of 10 kΩ. It was found that ozone cleaning (60°C, 20-30 min) of the Pt surface results in much lower contact resistance between Pt and graphene (~1 kΩ). The graphene transfer is performed within an hour of the ozone clean. The water is allowed to naturally evaporate. I “relax” the membrane by heating up the chip to 160 °C, then remove the PMMA in 1:1 dichloromethane and acetone. Others prefer to use a drop of anisole for the graphene relaxation and that may indeed be a superior method.

The next step is to pattern the graphene into micron-scale strips. Because photoresist tends to leave residue that is difficult to remove while keeping the graphene intact, we protect the graphene by spinning on a thin layer of PMMA first. After the photoresist (Shipley 1813) is exposed (ABM) and developed, we use the YES asher at 500 W, 80°C, to etch away the PMMA as well as the graphene in the exposed regions. It takes about 6–7 minutes for this process to etch through 200 nm of PMMA. We had originally used the Oxford 80 for this purpose, but found that a continuous 2 min etch resulted in a large amount of residue that was practically impossible to remove. We have been advised that the residue may be avoided by running the tool in 30 s intervals with a cool-down period in between. The remaining PMMA/photoresist double-layer is then removed by soaking in 1165.

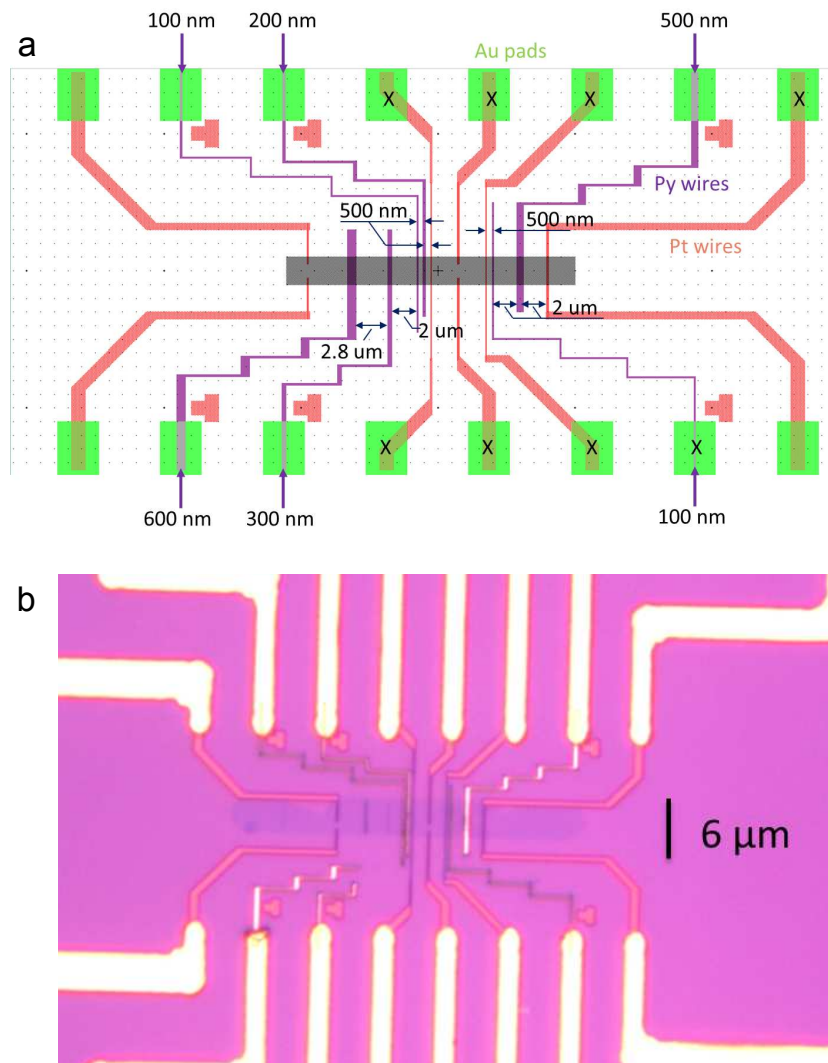
For devices with magnetic electrodes, a second e-beam step, using the same exposure sequence and the same alignment marks, is done to define Py or Co electrodes. This deposition required particular care in the resist recipe. We imaged the resist profile of the PMMA/copolymer bilayer to find a dose and development process that would give sufficient undercut to allow us to do angle evaporation to isolate the magnet from graphene with an oxide layer without shorting at the edges. This procedure was described in more detail in Chapter 2. We use the Sharon evaporator for this deposition because we follow the recipe of Ref. [146] and use an oxidized Ti seeding layer (nominally 0.5 nm) before the evaporation of 2 nm of Al_2O_3 . The process gas valve on the Sharon is used to let in ~ 10 mTorr of O_2 before pumping down again for the Al_2O_3 evaporation. After 40-60 nm of Py *or* Co, 10 nm of Au is deposited as a capping layer. In our experience the Co electrodes are almost always well-isolated from graphene (resistance of $> M\Omega$), but Py electrodes tend to form low-resistance contacts (10 k Ω), even with fairly thick oxide layers (total of 4 nm).

Finally, another contact lithography step is performed to define contact pads, aligning to marks in Pt (first e-beam). For measurements on the projected-field magnet probe station, the pads have minimal space in between to allow for convenient usage of the DC probes (Cascade Microtech). About 100 nm of Au is sufficient.

5.6 Results to-date

At the moment we are tackling the issue of fabricating devices with good tunnel barriers. We have found that Co electrodes on top of (nominally) 0.5 nm

Figure 5.10: a) Design of the device, showing the layout of Pt and Py electrodes and Au contacts. The important width and separation dimensions are labeled. X's mark the pads to which we wire-bonded for PPMS measurements. b) An optical image of a device. Notice that some of the FM electrodes peeled off during processing.

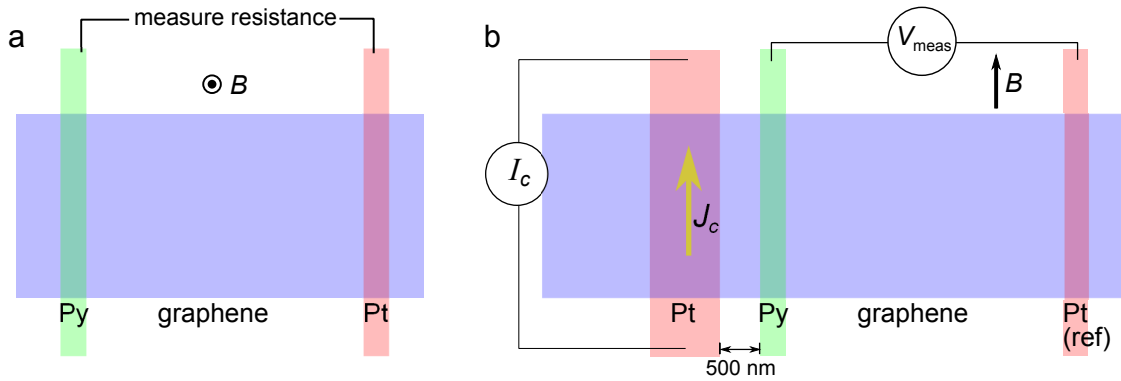


of oxidized titanium and 0.6 nm of Al_2O_3 yields low-bias resistances on the order of $\text{M}\Omega$. This is significantly higher than what has been reported, which may be both an advantage (high efficiency in polarization) and disadvantage (maximum charge current injection may be small). In a previous Pt/Py device with low tunnel barrier resistance ($\sim 10 \text{ k}\Omega$), we performed low- and room-temperature measurements of local and non-local resistance as a function of magnetic field. Although we did not see spin Hall related signals (not surprising given the low resistance of our “tunnel” contacts), I discuss the data here briefly since the knowledge may influence our later measurements (either as a signal of interest or as a background annoyance). Specifically, at low temperatures, we observe features consistent with weak localization and field-dependent low-frequency noise from the device. Our un-gated Hall measurement translates to a carrier density of $1.4 \times 10^{13} \text{ cm}^{-2}$. All measurements described in this section were done with lock-ins at low frequencies ($< 100 \text{ Hz}$), with the sample in the PPMS (Quantum Design) system. The design and an optical image of a device are shown in Fig. 5.10.

Figure 5.11a shows the configuration for a magneto-resistance measurement through a FM Py electrode and a Pt electrode connected by graphene, with the field applied perpendicular to the graphene plane. The data for different temperatures are shown in Fig. 5.12. The resistance measured here appears to be a sum of at least three components: a sharp peak visible at low temperatures (4 K and 30 K) of width 20–30 mT, a broader peak that has a weak temperature dependence of width 100–300 mT, and a broad parabolic field dependence that extends to high field. The first is consistent with a resistance peak from weak localization (WL), which is expected as the phase coherence length in graphene, l_ϕ , has been measured to be on the order of $1 \mu\text{m}$ [175, 176], and our electrodes

are separated by about 500 nm. The amplitude of the WL peak is known to be suppressed in graphene due to ripples which have the effect of a random magnetic field [175]. The broader peak appears to originate from the magnetoresistance of the Py electrode itself, which we measured separately in isolated wires deposited at the same time. The parabolic field dependence is not noticeably temperature dependent, indicating that it is not related to interference effects, and can be explained by classical theory for semiconductors with two types of carriers (here electrons and holes) [177].

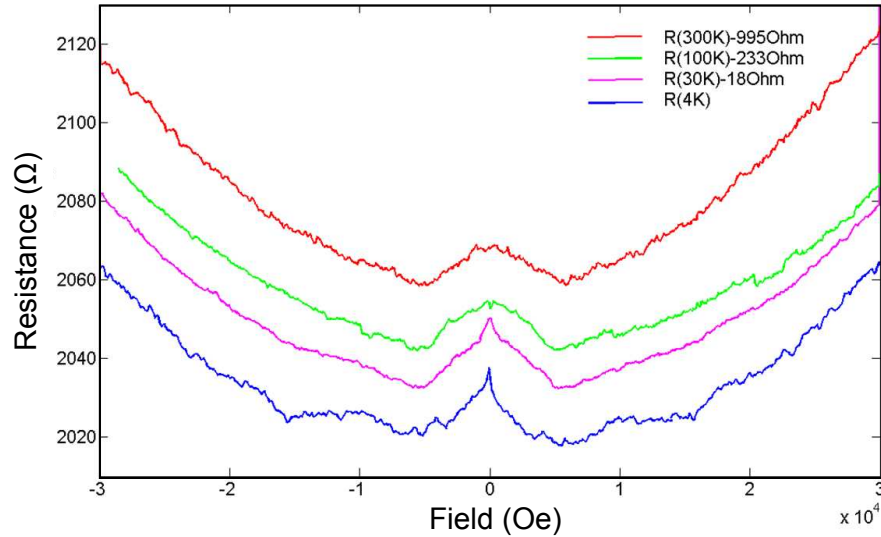
Figure 5.11: a,b) Measurement configurations for the data shown in Figs. 5.12 and 5.13, respectively. (a) is a “local” resistance measurement. (b) is a non-local voltage measurement.



The data in Fig. 5.13 corresponds to the non-local measurement configuration shown in Fig. 5.11b. The oscillations seen in the three lower V_{NL} vs. field curves are oscillations in *time*, at about 0.2–0.3 Hz; the field is being swept at 100 Oe/s in a direction parallel to the Pt and Py longitudinal axis. As the data shown is the output of a lock-in, it indicates some low-frequency noise that is interfering with the lock-in detection at 23 Hz, with a time constant of 500 ms. Unfortunately, we did not obtain a power spectrum at the low frequency range before the device died.

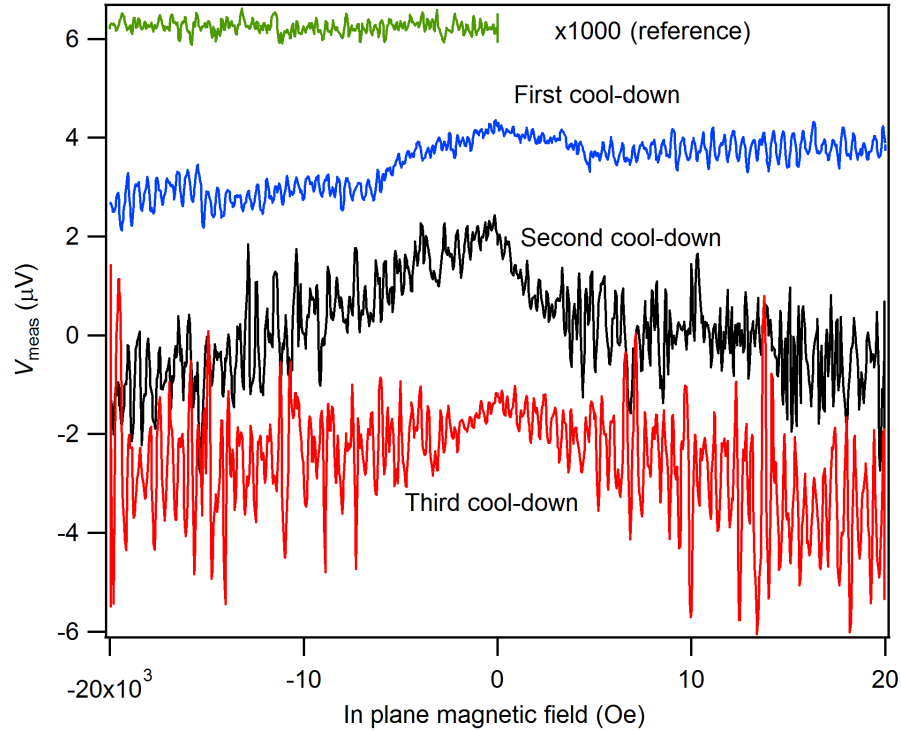
At first this curious signal was assumed to be from noise in the external cir-

Figure 5.12: Resistance *vs.* magnetic field (out-of-plane) data from the measurement configuration in Fig. 5.11, for decreasing temperature, from top to bottom. The traces have been offset by the resistance values in the legend for clarity.



cuit, but comparing to other “control” measurements performed with the same circuit, not across a graphene section, such as the top trace, we see that the oscillations appear to be related to the device in some way. Furthermore, the amplitude of the oscillations are field-dependent and increase with the number of thermal cycles experienced (with unintended exposure to condensation each time). It seems that the device may be picking up some low-frequency noise from the external circuit and either the pick-up or the noise itself is field-dependent. The effect of condensation (increased impurities) resembles that seen for $1/f$ noise (also known as flicker noise) in graphene which has been observed to increase with water adsorption [178, 179]. As far as I know, the magnetic field dependence of flicker noise has not been reported or explained, except in a brief section in the thesis of Morozov [180], an author in Ref. [178], where an order of magnitude increase of the noise amplitude with applying 2 T was observed near the Dirac point. Away from the Dirac point, the effect of

Figure 5.13: Non-local voltage measurement as a function of field for the configuration shown in Fig. 5.11b, for the same device, on successive cool-downs, including a vent to air in between. The oscillations seen in the traces are *in time*, as the field is swept at 100 Oe/s. The top trace is the measured voltage $\times 1000$ for clarity, across a continuous Pt wire, for comparison. All traces measured at 4 K, and have been offset for clarity. $J_c = 2.2 \mu\text{A}$.



the magnetic field is weaker. This data illustrate the importance of keeping the graphene as pristine as possible for SHE measurements, else resorting to measuring with the lock-in at a higher frequency.

Finally, the last feature I would like to point out is the broad peak in Fig. 5.13 at zero-field, extending to 400 mT. This feature has a sharp temperature dependence and is almost completely absent at 30 K. The field scale of this feature is the same as that for the magnetoresistance of an isolated Py wire with the same geometry. Recalling that this is a non-local voltage measurement, with-

out further measurements available, my current hypothesis is that this feature is related to the so-called giant non-locality in graphene which has a sharp temperature dependence [181]. Abanin *et al.* observed at high fields, near the Dirac point, large non-local signals microns away from the current path, on the order of hundreds of ohms. If the carriers in graphene have long range character, the magnetoresistance of the Py can conceivably have a strong influence on the spatial potential profile.

5.7 Next steps

The above has been a very preliminary discussion of some features observed in our devices thus far. We have are working to implement our latest FM fabrication technique on SHE devices, which will hopefully allow us to measure signals from spin injection. It will also be interesting to further investigate the use of graphene as a magnetic tunnel barrier.

APPENDIX A

JEOL6300 SCRIPT FOR BREAK-JUNCTION FABRICATION

```
//////////////////////////////////////;
//      EST120111 write job deck          //;
//      JEOL 6300 4th lens                 //;
//      ellipses                           //;
//////////////////////////////////////;

JOB/W ,4,4 ; 4 inch

GLMPOS P=(-31800,-2400), Q =(31800,2400)
; use outer set of marks at chipCoord=(+/-2400,+/-2400)
GLMP 3.0, 30.0, 0, 0
; mark dimensions 3 um wide, 60 um long crosses

PATH CALD
; for 4th lens -- aligned or virtual marks use CALD;
heimap use CALHD
; for 5th lens -- CAL or MINI01 (skips DISTBE)

ARRAY (-24000,3,18000)/(24000,4,12000)
; do local alignment once for every 6 dies
; 3 x 4 x 3 x 2 = 72 dies in this job
      CHMPOS M1=(-1800,2400),M2=(13800,2400),M3=(13800,-8400),M4=(-1800,-8400)
      ASSIGN A(1)-> ((*,*))
AEND

; this is a dose test on one side of the wafer
ARRAY (0,1,0)/(-30000,1,0)
      CHMPOS M1=(-1800,2400),M2=(1800,2400),M3=(1800,-2400),M4=(-1800,-2400)
      ASSIGN A(2) -> ((*,*))
AEND

1:  ARRAY (0,3,6000)/(0,2,6000)
      ASSIGN P(1)-> ((*,*),SHOT01)
      AEND
2:  ARRAY (-1150,2,2300)/(1500,5,750)
      ASSIGN P(2)-> ((1,1),SHOT02)
      ASSIGN P(2)-> ((2,1),SHOT03)
      ASSIGN P(2)-> ((1,2),SHOT04)
      ASSIGN P(2)-> ((2,2),SHOT05)
      ASSIGN P(2)-> ((1,3),SHOT06)
      ASSIGN P(2)-> ((2,3),SHOT07)
      ASSIGN P(2)-> ((1,4),SHOT08)
      ASSIGN P(2)-> ((2,4),SHOT09)
      ASSIGN P(2)-> ((1,5),SHOT10)
      ASSIGN P(2)-> ((2,5),SHOT11)
      AEND
PEND
```

```

;-----;
;   Layer Definition   ;
;-----;

LAYER 1
P(1) 'write111128_ellipse.v30'
P(2) 'write120118_test.v30'
SHOT01:      MODULAT ((1,0))
SHOT02: MODULAT ((1,20))
SHOT03:      MODULAT ((1,40))
SHOT04:      MODULAT ((1,60))
SHOT05:      MODULAT ((1,80))
SHOT06:      MODULAT ((1,100))
SHOT07:      MODULAT ((1,120))
SHOT08:      MODULAT ((1,140))
SHOT09:      MODULAT ((1,160))
SHOT10:      MODULAT ((1,180))
SHOT11:      MODULAT ((1,200))

STDCUR 1.0

END

;----- SDF file -----;

#3
; shelf number
JDF 'write120118', 1 ; jdf file name, layer number
EOS 3,'est27_1nA_Ap60'; 4th lens, condition file name
LBC ON
SHOT A,8 ; shot pitch
RESIST 1300,1300 ; area dose (uC/cm^2)
GLMDET S ; semiauto
CHMDET S
CHIPAL 4 ; use 4 marks
HSWITCH OFF,ON
OFFSET (-1852.5,342.2) ; calculate during calibration

END 3

```

BIBLIOGRAPHY

- [1] A. Aviram and M. Ratner, "Molecular rectifiers," *Chemical Physics Letters*, vol. 29, pp. 277–283, 1974.
- [2] D. J. Wold and C. D. Frisbie, "Fabrication and characterization of metal-molecule-metal junctions by conducting probe atomic force microscopy," *Journal of the American Chemical Society*, vol. 123, no. 23, pp. 5549–5556, 2001. PMID: 11389638.
- [3] J. J. Parks, A. R. Champagne, T. A. Costi, W. W. Shum, A. N. Pasupathy, E. Neuscamman, S. Flores-Torres, P. S. Cornaglia, A. A. Aligia, C. A. Balseiro, G. K.-L. Chan, H. D. Abruña, and D. C. Ralph, "Mechanical control of spin states in spin-1 molecules and the underscreened Kondo effect," *Science*, vol. 328, no. 5984, pp. 1370–1373, 2010.
- [4] S. W. Wu, N. Ogawa, and W. Ho, "Atomic-scale coupling of photons to single-molecule junctions," *Science*, vol. 312, no. 5778, pp. 1362–1365, 2006.
- [5] J. Repp, G. Meyer, S. M. Stojković, A. Gourdon, and C. Joachim, "Molecules on insulating films: Scanning-tunneling microscopy imaging of individual molecular orbitals," *Physical Review Letters*, vol. 94, p. 026803, Jan 2005.
- [6] B. C. Stipe, M. A. Rezaei, and W. Ho, "Single-molecule vibrational spectroscopy and microscopy," *Science*, vol. 280, no. 5370, pp. 1732–1735, 1998.
- [7] A. J. Heinrich, J. A. Gupta, C. P. Lutz, and D. M. Eigler, "Single-atom spin-flip spectroscopy," *Science*, vol. 306, no. 5695, pp. 466–469, 2004.
- [8] L. Gross, F. Mohn, N. Moll, P. Liljeroth, and G. Meyer, "The chemical structure of a molecule resolved by atomic force microscopy," *Science*, vol. 325, no. 5944, pp. 1110–1114, 2009.
- [9] G. Leatherman, E. N. Durantini, D. Gust, T. A. Moore, A. L. Moore, S. Stone, Z. Zhou, P. Rez, Y. Z. Liu, and S. M. Lindsay, "Carotene as a molecular wire: conducting atomic force microscopy," *The Journal of Physical Chemistry B*, vol. 103, no. 20, pp. 4006–4010, 1999.
- [10] S. J. Tans, A. R. M. Verschueren, and C. Dekker, "Room-temperature transistor based on a single carbon nanotube," *Nature*, vol. 393, pp. 49–52, May 1998.

- [11] H. Park, J. Park, A. K. L. Lim, E. H. Anderson, A. P. Alivisatos, and P. L. McEuen, "Nanomechanical oscillations in a single-C₆₀ transistor," *Nature*, vol. 407, pp. 57–60, 2000.
- [12] J. Park, A. Pasupathy, J. Goldsmith, C. Chang, Y. Yaish, J. Petta, M. Rinkoski, J. Sethna, H. Abruña, P. McEuen, and D. Ralph, "Coulomb blockade and the Kondo effect in single-atom transistors," *Nature*, vol. 417, p. 722, June 2002.
- [13] X. D. Cui, A. Primak, X. Zarate, J. Tomfohr, O. F. Sankey, A. L. Moore, T. A. Moore, D. Gust, G. Harris, and S. M. Lindsay, "Reproducible measurement of single-molecule conductivity," *Science*, vol. 294, no. 5542, pp. 571–574, 2001.
- [14] G. K. Ramachandran, J. K. Tomfohr, J. Li, O. F. Sankey, X. Zarate, A. Primak, Y. Terazono, T. A. Moore, A. L. Moore, D. Gust, L. A. Nagahara, and S. M. Lindsay, "Electron transport properties of a carotene molecule in a metal(single molecule)metal junction," *The Journal of Physical Chemistry B*, vol. 107, no. 25, pp. 6162–6169, 2003.
- [15] R. Smit, Y. Noat, C. Untiedt, N. D. Lang, M. C. van Hemert, and J. M. van Ruitenbeek, "Measurement of the conductance of a hydrogen molecule," *Nature*, vol. 419, no. 6910, pp. 906–909, 2002.
- [16] J. van Ruitenbeek, E. Scheer, and H. Weber, "Contacting individual molecules using mechanically controllable break junctions," in *Introducing Molecular Electronics* (G. Cuniberti, G. Fagas, and K. Richter, eds.), pp. 253–274, Springer Lecture Notes in Physics, 2005.
- [17] B. Xu and N. J. Tao, "Measurement of single-molecule resistance by repeated formation of molecular junctions," *Science*, vol. 301, pp. 1221–1223, Aug. 2003.
- [18] M. Frei, S. V. Aradhya, M. Koentopp, M. S. Hybertsen, and L. Venkataraman, "Mechanics and chemistry: Single molecule bond rupture forces correlate with molecular backbone structure," *Nano Letters*, vol. 11, no. 4, pp. 1518–1523, 2011.
- [19] J. R. Widawsky, M. Kamenetska, J. Klare, C. Nuckolls, M. L. Steigerwald, M. S. Hybertsen, and L. Venkataraman, "Measurement of voltage-dependent electronic transport across amine-linked single-molecular-wire junctions," *Nanotechnology*, vol. 20, no. 43, p. 434009, 2009.

- [20] J. R. Widawsky, P. Darancet, J. B. Neaton, and L. Venkataraman, "Simultaneous determination of conductance and thermopower of single molecule junctions," *Nano Letters*, vol. 12, no. 1, pp. 354–358, 2012.
- [21] L. Venkataraman, J. E. Klare, I. W. Tam, C. Nuckolls, M. S. Hybertsen, and M. L. Steigerwald, "Single-molecule circuits with well-defined molecular conductance," *Nano Letters*, vol. 6, pp. 458–462, Mar. 2006.
- [22] "The 2007 nobel prize in physics - press release." Nobelprize.org., Aug 2012. http://www.nobelprize.org/nobel_prizes/physics/laureates/2007/press.html.
- [23] G. Binasch, P. Grünberg, F. Saurenbach, and W. Zinn, "Enhanced magnetoresistance in layered magnetic structures with antiferromagnetic inter-layer exchange," *Physical Review B*, vol. 39, pp. 4828–4830, Mar 1989.
- [24] M. N. Baibich, J. M. Broto, A. Fert, F. N. Van Dau, F. Petroff, P. Etienne, G. Creuzet, A. Friederich, and J. Chazelas, "Giant magnetoresistance of (001)Fe/(001)Cr magnetic superlattices," *Physical Review Letters*, vol. 61, pp. 2472–2475, Nov 1988.
- [25] S. Datta and B. Das, "Electronic analog of the electro-optic modulator," *Applied Physics Letters*, vol. 56, no. 7, pp. 665–667, 1990.
- [26] L. Thomas, F. Lioni, R. Ballou, D. Gatteschi, R. Sessoli, and B. Barbara, "Macroscopic quantum tunnelling of magnetization in a single crystal of nanomagnets," *Nature*, vol. 383, pp. 145–147, Sept. 1996.
- [27] W. Wernsdorfer and R. Sessoli, "Quantum phase interference and parity effects in magnetic molecular clusters," *Science*, vol. 284, no. 5411, pp. 133–135, 1999.
- [28] M. N. Leuenberger and D. Loss, "Quantum computing in molecular magnets," *Nature*, vol. 410, pp. 789–793, 2001.
- [29] A. Ardavan, O. Rival, J. J. L. Morton, S. J. Blundell, A. M. Tyryshkin, G. A. Timco, and R. E. P. Winpenny, "Will spin-relaxation times in molecular magnets permit quantum information processing?," *Physical Review Letters*, vol. 98, p. 057201, Jan 2007.
- [30] A. R. Rocha, V. M. Garcia-suarez, S. W. Bailey, C. J. Lambert, J. Ferrer,

- and S. Sanvito, "Towards molecular spintronics," *Nature Materials*, vol. 4, pp. 335–339, Apr. 2005.
- [31] L. Bogani and W. Wernsdorfer, "Molecular spintronics using single-molecule magnets," *Nature Materials*, vol. 7, no. 3, pp. 179–186, 2008.
- [32] D. Huertas-Hernando, F. Guinea, and A. Brataas, "Spin-orbit coupling in curved graphene, fullerenes, nanotubes, and nanotube caps," *Physical Review B*, vol. 74, p. 155426, Oct 2006.
- [33] N. Tombros, C. Jozsa, M. Popinciuc, H. T. Jonkman, and B. J. van Wees, "Electronic spin transport and spin precession in single graphene layers at room temperature," *Nature*, vol. 448, pp. 571–575, 2007.
- [34] F. Kuemmeth, S. Ilani, D. C. Ralph, and P. L. McEuen, "Coupling of spin and orbital motion of electrons in carbon nanotubes," *Nature*, pp. 448–452, 2008.
- [35] M. A. Kastner, "The single electron transistor and artificial atoms," *Annals of Physics*, vol. 9, no. 11–12, pp. 885–894, 2000.
- [36] S. Datta, *Electronic Transport in Mesoscopic Systems*. Cambridge University Press, 1997.
- [37] D. K. Ferry and S. M. Goodnick, *Transport in Nanostructures*. Cambridge University Press, 1997.
- [38] J. Grose, *Electron Transport in Single-Molecule Transistors Based on High-Spin Molecules*. PhD thesis, Cornell University, 2007.
- [39] A. Pasupathy, *Electron Transport in Molecular Transistors*. PhD thesis, Cornell University, 2004.
- [40] T. A. Fulton and G. J. Dolan, "Observation of single-electron charging effects in small tunnel junctions," *Physical Review Letters*, vol. 59, pp. 109–112, Jul 1987.
- [41] D. Goldhaber-Gordon, H. Shtrikman, D. Mahalu, D. Abusch-Magder, U. Meirav, and M. A. Kastner, "Kondo effect in a single-electron transistor," *Nature*, vol. 391, pp. 156–159, Jan. 1998.

- [42] R. C. Ashoori, "Electrons in artificial atoms," *Nature*, vol. 379, pp. 413–419, 1996.
- [43] K. I. Bolotin, F. Kuemmeth, A. N. Pasupathy, and D. C. Ralph, "Metal-nanoparticle single-electron transistors fabricated using electromigration," *Applied Physics Letters*, vol. 84, no. 16, pp. 3154–3156, 2004.
- [44] S. De Franceschi, S. Sasaki, J. M. Elzerman, W. G. van der Wiel, S. Tarucha, and L. P. Kouwenhoven, "Electron cotunneling in a semiconductor quantum dot," *Physical Review Letters*, vol. 86, pp. 878–881, Jan 2001.
- [45] N. Roch, R. Vincent, F. Elste, W. Harneit, W. Wernsdorfer, C. Timm, and F. Balestro, "Cotunneling through a magnetic single-molecule transistor based on N@C₆₀," *Physical Review B*, vol. 83, p. 081407, Feb 2011.
- [46] J. Kondo and A. C. Hewson, "Kondo effect," *Scholarpedia*, vol. 4, no. 3, p. 7529, 2009.
- [47] J. Kondo, "Resistance minimum in dilute magnetic alloys," *Progress of Theoretical Physics*, vol. 32, no. 1, pp. 37–49, 1964.
- [48] A. N. Pasupathy, R. C. Bialczak, J. Martinek, J. E. Grose, L. A. K. Donev, P. L. McEuen, and D. C. Ralph, "The Kondo effect in the presence of ferromagnetism," *Science*, vol. 306, no. 5693, pp. 86–89, 2004.
- [49] J. J. Parks, A. R. Champagne, G. R. Hutchison, S. Flores-Torres, H. D. Abruña, and D. C. Ralph, "Tuning the Kondo effect with a mechanically controllable break junction," *Physical Review Letters*, vol. 99, p. 026601, Jul 2007.
- [50] J. Parks, *Mechanical Control of the Kondo Effect and Spin States*. PhD thesis, Cornell University, 2009.
- [51] F. Kuemmeth, *Spin states and spin-orbit coupling in nanostructures*. PhD thesis, Cornell University, 2008.
- [52] Y. Cui, M. T. Björk, J. A. Liddle, C. Sönnichsen, B. Boussert, and A. P. Alivisatos, "Integration of colloidal nanocrystals into lithographically patterned devices," *Nano Letters*, vol. 4, no. 6, pp. 1093–1098, 2004.
- [53] A. Bezryadin, C. Dekker, and G. Schmid, "Electrostatic trapping of single

conducting nanoparticles between nanoelectrodes," *Applied Physics Letters*, vol. 71, no. 9, pp. 1273–1275, 1997.

- [54] T. Taychatanapat, K. I. Bolotin, F. Kuemmeth, and D. C. Ralph, "Imaging electromigration during the formation of break junctions," *Nano Letters*, vol. 7, pp. 652–656, Mar. 2007.
- [55] J. Grose, E. Tam, C. Timm, M. Scheloske, B. Ulgut, J. Parks, H. D. Abruña, W. Harneit, and D. C. Ralph, "Tunnelling spectra of individual magnetic endofullerene molecules," *Nature Materials*, vol. 7, pp. 884–889, Nov. 2008.
- [56] W. Wernsdorfer, M. Murugesu, and G. Christou, "Resonant tunneling in truly axial symmetry Mn_{12} single-molecule magnets: Sharp crossover between thermally assisted and pure quantum tunneling," *Physical Review Letters*, vol. 96, p. 057208, Feb 2006.
- [57] M.-H. Jo, J. E. Grose, K. Baheti, M. M. Deshmukh, J. J. Sokol, E. M. Rumberger, D. N. Hendrickson, J. R. Long, H. Park, and D. C. Ralph, "Signatures of molecular magnetism in single-molecule transport spectroscopy," *Nano Letters*, vol. 6, no. 9, pp. 2014–2020, 2006.
- [58] H. B. Heersche, Z. de Groot, J. A. Folk, H. S. J. van der Zant, C. Romeike, M. R. Wegewijs, L. Zobbi, D. Barreca, E. Tondello, and A. Cornia, "Electron transport through single Mn_{12} molecular magnets," *Physical Review Letters*, vol. 96, p. 206801, May 2006.
- [59] A. R. Champagne, A. N. Pasupathy, and D. C. Ralph, "Mechanically adjustable and electrically gated single-molecule transistors," *Nano Letters*, vol. 5, no. 2, pp. 305–308, 2005.
- [60] C. Joachim, J. K. Gimzewski, R. R. Schlittler, and C. Chavy, "Electronic transparency of a single C_{60} molecule," *Physical Review Letters*, vol. 74, pp. 2102–2105, Mar 1995.
- [61] P. Jakes, K.-P. Dinse, C. Meyer, W. Harneit, and A. Weidinger, "Purification and optical spectroscopy of $N@C_{60}$," *Physical Chemistry Chemical Physics*, vol. 5, pp. 4080–4083, 2003.
- [62] S. Modesti, S. Cerasari, and P. Rudolf, "Determination of charge states of C_{60} adsorbed on metal surfaces," *Physical Review Letters*, vol. 71, pp. 2469–2472, Oct 1993.

- [63] N. Swami, H. He, and B. E. Koel, "Polymerization and decomposition of C_{60} on Pt(111) surfaces," *Physical Review B*, vol. 59, pp. 8283–8291, Mar 1999.
- [64] P. Bhyrappa, P. Paul, J. Stinchcombe, P. D. W. Boyd, and C. A. Reed, "Synthesis and electronic characterization of discrete buckminsterfulleride salts: C_{60}^{2-} and C_{60}^{3-} ," *Journal of the American Chemical Society*, vol. 115, no. 23, pp. 11004–11005, 1993.
- [65] C. A. Reed and R. D. Bolskar, "Discrete fulleride anions and fullerenium cations," *Chemical Reviews*, vol. 100, no. 3, pp. 1075–1120, 2000.
- [66] F. Elste and C. Timm, "Theory for transport through a single magnetic molecule: Endohedral $N@C_{60}$," *Physical Review B*, vol. 71, p. 155403, Apr 2005.
- [67] L. Udvardi, "Surface effects on the electronic structure of solid C_{60} ," in *Electronic Properties of Novel Materials — Molecular Nanostructures* (H. Kuzmany, J. Fink., M. Mehring, and S. Roth, eds.), pp. 187–180, AIP, 2000.
- [68] R. Heid, L. Pintschovius, and J. M. Godard, "Eigenvectors of internal vibrations of C_{60} : Theory and experiment," *Physical Review B*, vol. 56, pp. 5925–5936, Sep 1997.
- [69] M. M. Deshmukh, S. Kleff, S. Guéron, E. Bonet, A. N. Pasupathy, J. von Delft, and D. C. Ralph, "Magnetic anisotropy variations and nonequilibrium tunneling in a cobalt nanoparticle," *Physical Review Letters*, vol. 87, p. 226801, Nov 2001.
- [70] T. Fujisawa, D. G. Austing, Y. Tokura, Y. Hirayama, and S. Tarucha, "Nonequilibrium transport through a vertical quantum dot in the absence of spin-flip energy relaxation," *Physical Review Letters*, vol. 88, p. 236802, May 2002.
- [71] N. Roch, S. Florens, V. Bouchiat, W. Wernsdorfer, and F. Balestro, "Quantum phase transition in a single-molecule quantum dot," *Nature*, vol. 453, pp. 633–637, May 2008.
- [72] R. Vincent, S. Klyatskaya, M. Ruben, W. Wernsdorfer, and F. Balestro, "Electronic read-out of a single nuclear spin using a molecular spin transistor," *Nature*, vol. 488, pp. 357–360, 2012.

- [73] X. Zhou, Z. Chen, S. Liu, S. Jin, L. Liu, H. Zhang, Z. Xie, Y. Jiang, and B. Mao, "Single molecule conductance of dipyridines with conjugated ethene and nonconjugated ethane bridging group," *The Journal of Physical Chemistry C*, vol. 112, pp. 3935–3940, Mar. 2008.
- [74] A. I. Yanson, G. R. Bollinger, H. E. van den Brom, N. Agrait, and J. M. van Ruitenbeek, "Formation and manipulation of a metallic wire of single gold atoms," *Nature*, vol. 395, pp. 783–785, Oct. 1998.
- [75] N. Agrait, A. Yeyati, and J. van Ruitenbeek, "Quantum properties of atomic-sized conductors," *Physics Reports*, vol. 377, no. 8, pp. 81–279, 2003.
- [76] R. Landauer, "Electrical resistance of disordered one-dimensional lattices," *Philosophical Magazine*, vol. 21, pp. 863–867, 1970.
- [77] B. J. van Wees, H. van Houten, C. W. J. Beenakker, J. G. Williamson, L. P. Kouwenhoven, D. van der Marel, and C. T. Foxon, "Quantized conductance of point contacts in a two-dimensional electron gas," *Physical Review Letters*, vol. 60, pp. 848–850, Feb 1988.
- [78] D. A. Wharam, T. J. Thornton, R. Newbury, M. Pepper, H. Ahmed, J. E. F. Frost, D. G. Hasko, D. C. Peacock, D. A. Ritchie, and G. A. C. Jones, "One-dimensional transport and the quantisation of the ballistic resistance," *Journal of Physics C: Solid State Physics*, vol. 21, no. 8, p. L209, 1988.
- [79] H. Ohnishi, Y. Kondo, and K. Takayanagi, "Quantized conductance through individual rows of suspended gold atoms," *Nature*, vol. 395, pp. 780–783, 1998.
- [80] H. E. van den Brom and J. M. van Ruitenbeek, "Shot noise suppression in metallic quantum point contacts," in *Statistical and Dynamical Aspects of Mesoscopic Systems* (D. Reguera, G. Platero, L. L. Bonilla, and J. M. Rubí, eds.), pp. 114–122, Springer-Verlag, 2000.
- [81] R. Parameswaran, J. R. Widawsky, H. Vázquez, Y. S. Park, B. M. Boardman, C. Nuckolls, M. L. Steigerwald, M. S. Hybertsen, and L. Venkataraman, "Reliable formation of single molecule junctions with air-stable diphenylphosphine linkers," *The Journal of Physical Chemistry Letters*, vol. 1, no. 14, pp. 2114–2119, 2010.
- [82] Y. S. Park, A. C. Whalley, M. Kamenetska, M. L. Steigerwald, M. S. Hybertsen, C. Nuckolls, and L. Venkataraman, "Contact chemistry and single-molecule conductance: a comparison of phosphines, methyl sulfides, and

amines," *Journal of the American Chemical Society*, vol. 129, pp. 15768–15769, Dec. 2007.

- [83] S. Y. Quek, M. Kamenetska, M. L. Steigerwald, H. J. Choi, S. G. Louie, M. S. Hybertsen, J. B. Neaton, and L. Venkataraman, "Mechanically controlled binary conductance switching of a single-molecule junction," *Nat Nano*, vol. 4, pp. 230–234, Apr. 2009.
- [84] M. Kamenetska, M. Koentopp, A. C. Whalley, Y. S. Park, M. L. Steigerwald, C. Nuckolls, M. S. Hybertsen, and L. Venkataraman, "Formation and evolution of single-molecule junctions," *Physical Review Letters*, vol. 102, p. 126803, Mar. 2009.
- [85] C. Vericat, M. E. Vela, G. Benitez, P. Carro, and R. C. Salvarezza, "Self-assembled monolayers of thiols and dithiols on gold: new challenges for a well-known system," *Chem. Soc. Rev.*, vol. 39, pp. 1805–1834, 2010.
- [86] H. Hakkinen, "The gold-sulfur interface at the nanoscale," *Nature Chemistry*, vol. 4, pp. 443–455, June 2012.
- [87] Z. Huang, F. Chen, R. D'agosta, P. A. Bennett, M. Di Ventra, and N. Tao, "Local ionic and electron heating in single-molecule junctions," *Nature Nanotechnology*, vol. 2, pp. 698–703, Nov. 2007.
- [88] I. S. Kristensen, D. J. Mowbray, K. S. Thygesen, and K. W. Jacobsen, "Comparative study of anchoring groups for molecular electronics: structure and conductance of Au-S-Au and Au-NH₂-Au junctions," *Journal of Physics: Condensed Matter*, vol. 20, no. 37, p. 374101, 2008.
- [89] S. Y. Quek, L. Venkataraman, H. J. Choi, S. G. Louie, M. S. Hybertsen, and J. B. Neaton, "Amine-gold linked single-molecule circuits: experiment and theory," *Nano Letters*, vol. 7, no. 11, pp. 3477–3482, 2007.
- [90] F. Evers, F. Weigend, and M. Koentopp, "Conductance of molecular wires and transport calculations based on density-functional theory," *Physical Review B*, vol. 69, p. 235411, June 2004.
- [91] K. S. Thygesen, "Impact of exchange-correlation effects on the *IV* characteristics of a molecular junction," *Physical Review Letters*, vol. 100, p. 166804, Apr 2008.
- [92] M. Koentopp, K. Burke, and F. Evers, "Zero-Bias molecular electronics:

Exchange-Correlation corrections to Landauer's formula," *Physical Review B*, vol. 73, p. 121403, Mar. 2006.

- [93] S. K. Nielsen, M. Brandbyge, K. Hansen, K. Stokbro, J. M. van Ruitenbeek, and F. Besenbacher, "Current-voltage curves of atomic-sized transition metal contacts: An explanation of why Au is ohmic and Pt is not," *Physical Review Letters*, vol. 89, p. 066804, Jul 2002.
- [94] C. Toher, A. Filippetti, S. Sanvito, and K. Burke, "Self-interaction errors in density-functional calculations of electronic transport," *Physical Review Letters*, vol. 95, no. 14, p. 146402, 2005.
- [95] P. Delaney and J. C. Greer, "Correlated electron transport in molecular electronics," *Physical Review Letters*, vol. 93, p. 036805, July 2004.
- [96] M. S. Hybertsen and S. G. Louie, "Electron correlation in semiconductors and insulators: Band gaps and quasiparticle energies," *Physical Review B*, vol. 34, pp. 5390–5413, Oct 1986.
- [97] J. B. Neaton, M. S. Hybertsen, and S. G. Louie, "Renormalization of molecular electronic levels at metal-molecule interfaces," *Physical Review Letters*, vol. 97, p. 216405, Nov 2006.
- [98] M. Strange, C. Rostgaard, H. Häkkinen, and K. S. Thygesen, "Self-consistent GW calculations of electronic transport in thiol- and amine-linked molecular junctions," *Physical Review B*, vol. 83, p. 115108, Mar 2011.
- [99] X. Wang, C. D. Spataru, M. S. Hybertsen, and A. J. Millis, "Electronic correlation in nanoscale junctions: Comparison of the GW approximation to a numerically exact solution of the single-impurity Anderson model," *Physical Review B*, vol. 77, p. 045119, Jan 2008.
- [100] F. Flores, J. Ortega, and H. Vazquez, "Modelling energy level alignment at organic interfaces and density functional theory," *Physical Chemistry Chemical Physics*, vol. 11, pp. 8658–8675, 2009.
- [101] S. Y. Quek, H. J. Choi, S. G. Louie, and J. B. Neaton, "Length dependence of conductance in aromatic single-molecule junctions," *Nano Letters*, vol. 9, no. 11, pp. 3949–3953, 2009. PMID: 19751067.
- [102] L. Venkataraman, Y. S. Park, A. C. Whalley, C. Nuckolls, M. S. Hybert-

- sen, and M. L. Steigerwald, "Electronics and chemistry: varying single-molecule junction conductance using chemical substituents," *Nano Letters*, vol. 7, pp. 502–506, Feb. 2007.
- [103] L. Venkataraman, J. E. Klare, C. Nuckolls, M. S. Hybertsen, and M. L. Steigerwald, "Dependence of single-molecule junction conductance on molecular conformation," *Nature*, vol. 442, no. 7105, pp. 904–907, 2006.
- [104] K. Hansen, E. Laegsgaard, I. Stensgaard, and F. Besenbacher, "Quantized conductance in relays," *Physical Review B*, vol. 56, no. 4, pp. 2208–2220, 1997.
- [105] M. Kamenetska, S. Y. Quek, A. C. Whalley, M. L. Steigerwald, H. J. Choi, S. G. Louie, C. Nuckolls, M. S. Hybertsen, J. B. Neaton, and L. Venkataraman, "Conductance and geometry of pyridine-linked single-molecule junctions," *Journal of the American Chemical Society*, vol. 132, pp. 6817–6821, May 2010.
- [106] M. Irie, "Diarylethenes for memories and switches," *Chemical Reviews*, vol. 100, pp. 1685–1716, May 2000.
- [107] A. Staykov, J. Areephong, W. R. Browne, B. L. Feringa, and K. Yoshizawa, "Electrochemical and photochemical cyclization and cycloreversion of diarylethenes and diarylethene-capped sexithiophene wires," *ACS Nano*, vol. 5, pp. 1165–1178, Feb. 2011.
- [108] S. Jan van der Molen and P. Liljeroth, "Charge transport through molecular switches," *Journal of Physics: Condensed Matter*, vol. 22, p. 133001, Apr. 2010.
- [109] E. S. Tam, J. J. Parks, W. W. Shum, Y.-W. Zhong, M. B. Santiago-Berríos, X. Zheng, W. Yang, G. K.-L. Chan, H. D. Abruña, and D. C. Ralph, "Single-molecule conductance of pyridine-terminated dithienylethene switch molecules," *ACS Nano*, vol. 5, no. 6, pp. 5115–5123, 2011.
- [110] D. Dulić, S. J. van der Molen, T. Kudernac, H. T. Jonkman, J. J. D. de Jong, T. N. Bowden, J. van Esch, B. L. Feringa, and B. J. van Wees, "One-way optoelectronic switching of photochromic molecules on gold," *Physical Review Letters*, vol. 91, p. 207402, Nov. 2003.
- [111] S. J. van der Molen, J. Liao, T. Kudernac, J. S. Agustsson, L. Bernard, M. Calame, B. J. van Wees, B. L. Feringa, and C. Schönenberger, "Light-

controlled conductance switching of ordered metal-molecule-metal devices," *Nano Letters*, vol. 9, pp. 76–80, Jan. 2009.

- [112] J. He, F. Chen, P. A. Liddell, J. Andréasson, S. D. Straight, D. Gust, T. A. Moore, A. L. Moore, J. Li, O. F. Sankey, and S. M. Lindsay, "Switching of a photochromic molecule on gold electrodes: single-molecule measurements," *Nanotechnology*, vol. 16, pp. 695–702, June 2005.
- [113] N. Katsonis, T. Kudernac, M. Walko, S. vanderMolen, B. vanWees, and B. Feringa, "Reversible conductance switching of single diarylethenes on a gold surface," *Advanced Materials*, vol. 18, no. 11, pp. 1397–1400, 2006.
- [114] A. C. Whalley, M. L. Steigerwald, X. Guo, and C. Nuckolls, "Reversible switching in molecular electronic devices," *Journal of the American Chemical Society*, vol. 129, pp. 12590–12591, Oct. 2007.
- [115] K. Matsuda, H. Yamaguchi, T. Sakano, M. Ikeda, N. Tanifuji, and M. Irie, "Conductance photoswitching of diarylethene-gold nanoparticle network induced by photochromic reaction," *The Journal of Physical Chemistry C*, vol. 112, pp. 17005–17010, Oct. 2008.
- [116] T. Kudernac, S. J. v. d. Molen, B. J. v. Wees, and B. L. Feringa, "Uni- and bi-directional light-induced switching of diarylethenes on gold nanoparticles," *Chemical Communications*, no. 34, pp. 3597–3599, 2006.
- [117] J. Li, G. Speyer, and O. F. Sankey, "Conduction switching of photochromic molecules," *Physical Review Letters*, vol. 93, p. 248302, Dec. 2004.
- [118] M. Kondo, T. Tada, and K. Yoshizawa, "A theoretical measurement of the quantum transport through an optical molecular switch," *Chemical Physics Letters*, vol. 412, pp. 55–59, Aug. 2005.
- [119] A. Odell, A. Delin, B. Johansson, I. Rungger, and S. Sanvito, "Investigation of the conducting properties of a photoswitching dithienylethene molecule," *ACS Nano*, vol. 4, pp. 2635–2642, May 2010.
- [120] M. Zhuang and M. Ernzerhof, "Mechanism of a molecular electronic photoswitch," *Physical Review B*, vol. 72, no. 7, p. 073104, 2005.
- [121] H. Tian and S. Yang, "Recent progresses on diarylethene based photochromic switches," *Chemical Society Reviews*, vol. 33, no. 2, pp. 85–97, 2004.

- [122] R. J. Nichols, W. Haiss, S. J. Higgins, E. Leary, S. Martin, and D. Bethell, "The experimental determination of the conductance of single molecules," *Physical Chemistry Chemical Physics*, vol. 12, no. 12, p. 2801, 2010.
- [123] H. Basch, R. Cohen, and M. A. Ratner, "Interface geometry and molecular junction conductance: geometric fluctuation and stochastic switching," *Nano Letters*, vol. 5, no. 9, pp. 1668–1675, 2005.
- [124] M. Strange, O. Lopez-Acevedo, and H. Häkkinen, "Oligomeric goldthiolate units define the properties of the molecular junction between gold and benzene dithiols," *The Journal of Physical Chemistry Letters*, vol. 1, pp. 1528–1532, May 2010.
- [125] J. Ulrich, D. Esrail, W. Pontius, L. Venkataraman, D. Millar, and L. H. Doerr, "Variability of conductance in molecular junctions," *The Journal of Physical Chemistry B*, vol. 110, pp. 2462–2466, Feb. 2006.
- [126] M. T. González, S. Wu, R. Huber, S. J. van der Molen, C. Schönenberger, and M. Calame, "Electrical conductance of molecular junctions by a robust statistical analysis," *Nano Letters*, vol. 6, pp. 2238–2242, Oct. 2006.
- [127] J. M. Soler, E. Artacho, J. D. Gale, A. García, J. Junquera, P. Ordejón, and D. Sánchez-Portal, "The SIESTA method for ab initio order-N materials simulation," *Journal of Physics: Condensed Matter*, vol. 14, p. 2745, Mar. 2002.
- [128] S. Ke, H. U. Baranger, and W. Yang, "Electron transport through molecules: self-consistent and non-self-consistent approaches," *Physical Review B*, vol. 70, no. 8, p. 085410, 2004.
- [129] M. Di Ventra, S. T. Pantelides, and N. D. Lang, "First-principles calculation of transport properties of a molecular device," *Physical Review Letters*, vol. 84, p. 979, Jan. 2000.
- [130] S. Ke, H. U. Baranger, and W. Yang, "Role of the exchange-correlation potential in ab initio electron transport calculations," *The Journal of Chemical Physics*, vol. 126, no. 20, p. 201102, 2007.
- [131] N. Sai, M. Zwolak, G. Vignale, and M. Di Ventra, "Dynamical corrections to the DFT-LDA electron conductance in nanoscale systems," *Physical Review Letters*, vol. 94, p. 186810, May 2005.

- [132] Z.-L. Cheng, R. Skouta, H. Vazquez, J. R. Widawsky, S. Schneebeli, W. Chen, M. S. Hybertsen, R. Breslow, and L. Venkataraman, "In situ formation of highly conducting covalent AuC contacts for single-molecule junctions," *Nature Nanotechnology*, vol. 6, pp. 353–357, Jun 2011.
- [133] K. S. Novoselov, A. K. Geim, S. V. Morozov, D. Jiang, M. I. Katsnelson, I. V. Grigorieva, S. V. Dubonos, and A. A. Firsov, "Two-dimensional gas of massless Dirac fermions in graphene," *Nature*, vol. 438, pp. 197–200, Nov. 2005.
- [134] Y. Zhang, Y.-W. Tan, H. L. Stormer, and P. Kim, "Experimental observation of the quantum Hall effect and Berry's phase in graphene," *Nature*, vol. 438, pp. 201–204, Nov. 2005.
- [135] A. K. Geim and K. S. Novoselov, "The rise of graphene," *Nature Materials*, vol. 6, pp. 183–191, Mar. 2007.
- [136] K. S. Novoselov, A. K. Geim, S. V. Morozov, D. Jiang, Y. Zhang, S. V. Dubonos, I. V. Grigorieva, and A. A. Firsov, "Electric field effect in atomically thin carbon films," *Science*, vol. 306, no. 5696, pp. 666–669, 2004.
- [137] K. S. Novoselov, D. Jiang, F. Schedin, T. J. Booth, V. V. Khotkevich, S. V. Morozov, and A. K. Geim, "Two-dimensional atomic crystals," *Proceedings of the National Academy of Sciences of the United States of America*, vol. 102, no. 30, pp. 10451–10453, 2005.
- [138] A. K. Geim, "Graphene: Status and prospects," *Science*, vol. 324, no. 5934, pp. 1530–1534, 2009.
- [139] A. H. Castro Neto, F. Guinea, N. M. R. Peres, K. S. Novoselov, and A. K. Geim, "The electronic properties of graphene," *Reviews of Modern Physics*, vol. 81, pp. 109–162, Jan 2009.
- [140] S. Das Sarma, S. Adam, E. H. Hwang, and E. Rossi, "Electronic transport in two-dimensional graphene," *Rev. Mod. Phys.*, vol. 83, pp. 407–470, May 2011.
- [141] P. Avouris, "Graphene: Electronic and photonic properties and devices," *Nano Letters*, vol. 10, no. 11, pp. 4285–4294, 2010.
- [142] I. Zutic, J. Fabian, and S. Das Sarma, "Spintronics: Fundamentals and applications," *Reviews of Modern Physics*, vol. 76, pp. 323–410, 2004.

- [143] D. Pesin and A. H. MacDonald, "Spintronics and pseudospintronics in graphene and topological insulators," *Nature Materials*, vol. 11, pp. 409–416, 2012.
- [144] M. Gmitra, S. Konschuh, C. Ertler, C. Ambrosch-Draxl, and J. Fabian, "Band-structure topologies of graphene: Spin-orbit coupling effects from first principles," *Physical Review B*, vol. 80, p. 235431, Dec 2009.
- [145] D. Huertas-Hernando, F. Guinea, and A. Brataas, "Spin-orbit-mediated spin relaxation in graphene," *Physical Review Letters*, vol. 103, p. 146801, Sep 2009.
- [146] W. Han, K. Pi, K. M. McCreary, Y. Li, J. J. I. Wong, A. G. Swartz, and R. K. Kawakami, "Tunneling spin injection into single layer graphene," *Physical Review Letters*, vol. 105, p. 167202, Oct. 2010.
- [147] A. Avsar, T.-Y. Yang, S. Bae, J. Balakrishnan, F. Volmer, M. Jaiswal, Z. Yi, S. R. Ali, G. Güntherodt, B. H. Hong, B. Beschoten, and B. Özyilmaz, "Toward wafer scale fabrication of graphene based spin valve devices," *Nano Letters*, vol. 11, no. 6, pp. 2363–2368, 2011.
- [148] B. Dlubak, M.-B. Martin, C. Deranlot, B. Servet, S. Xavier, R. Mattana, M. Sprinkle, C. Berger, W. A. De Heer, F. Petroff, A. Anane, P. Seneor, and A. Fert, "Highly efficient spin transport in epitaxial graphene on SiC," *Nature Physics*, vol. 8, pp. 557–561, July 2012.
- [149] R. J. Elliott, "Theory of the effect of spin-orbit coupling on magnetic resonance in some semiconductors," *Phys. Rev.*, vol. 96, pp. 266–279, Oct 1954.
- [150] M. I. Dyakonov and V. I. Perel, "Spin relaxation of conduction electrons in noncentrosymmetric semiconductors.," *Sov. Phys. Solid State*, vol. 13, pp. 3023–3026, 1971.
- [151] W. Han and R. K. Kawakami, "Spin relaxation in single-layer and bilayer graphene," *Physical Review Letters*, vol. 107, p. 047207, Jul 2011.
- [152] S. O. Valenzuela, "Nonlocal electronic spin detection, spin accumulation and the spin Hall effect," *International Journal of Modern Physics B*, vol. 23, no. 11, pp. 2413–2438, 2009.
- [153] M. Johnson and R. H. Silsbee, "Coupling of electronic charge and spin at

- a ferromagnetic-paramagnetic metal interface," *Physical Review B*, vol. 37, pp. 5312–5325, Apr 1988.
- [154] E. I. Rashba, "Theory of electrical spin injection: Tunnel contacts as a solution of the conductivity mismatch problem," *Physical Review B*, vol. 62, pp. R16267–R16270, Dec 2000.
- [155] A. Fert and H. Jaffrès, "Conditions for efficient spin injection from a ferromagnetic metal into a semiconductor," *Physical Review B*, vol. 64, p. 184420, Oct 2001.
- [156] K. Pi, W. Han, K. M. McCreary, A. G. Swartz, Y. Li, and R. K. Kawakami, "Manipulation of spin transport in graphene by surface chemical doping," *Physical Review Letters*, vol. 104, p. 187201, May 2010.
- [157] J. E. Hirsch, "Spin Hall effect," *Physical Review Letters*, vol. 83, p. 1834, Oct. 1999.
- [158] M. Dyakonov and V. Perel, "Current-induced spin orientation of electrons in semiconductors," *Physics Letters A*, vol. 35, no. 6, pp. 459 – 460, 1971.
- [159] S. Murakami, "Intrinsic spin Hall effect," in *Advances in Solid State Physics* (B. Kramer, ed.), vol. 45 of *Advances in Solid State Physics*, pp. 197–209, Springer Berlin / Heidelberg, 2006.
- [160] J. Sinova, D. Culcer, Q. Niu, N. A. Sinitsyn, T. Jungwirth, and A. H. MacDonald, "Universal intrinsic spin Hall effect," *Physical Review Letters*, vol. 92, p. 126603, Mar 2004.
- [161] V. Sih, R. C. Myers, Y. K. Kato, W. H. Lau, A. C. Gossard, and D. D. Awschalom, "Spatial imaging of the spin Hall effect and current-induced polarization in two-dimensional electron gases," *Nature Physics*, vol. 1, pp. 31–35, 2005.
- [162] Y. K. Kato, R. C. Myers, A. C. Gossard, and D. D. Awschalom, "Observation of the spin Hall effect in semiconductors," *Science*, vol. 306, no. 5703, pp. 1910–1913, 2004.
- [163] S. O. Valenzuela and M. Tinkham, "Direct electronic measurement of the spin Hall effect," *Nature*, vol. 442, pp. 176–179, 2006.
- [164] S. Lowitzer, M. Gradhand, D. Ködderitzsch, D. V. Fedorov, I. Mertig, and

- H. Ebert, "Extrinsic and intrinsic contributions to the spin Hall effect of alloys," *Physical Review Letters*, vol. 106, p. 056601, Feb 2011.
- [165] G. Y. Guo, S. Murakami, T.-W. Chen, and N. Nagaosa, "Intrinsic spin hall effect in platinum: First-principles calculations," *Physical Review Letters*, vol. 100, p. 096401, Mar 2008.
- [166] M. Morota, Y. Niimi, K. Ohnishi, D. H. Wei, T. Tanaka, H. Kontani, T. Kimura, and Y. Otani, "Indication of intrinsic spin Hall effect in 4d and 5d transition metals," *Physical Review B*, vol. 83, p. 174405, May 2011.
- [167] L. Liu, O. J. Lee, T. J. Gudmundsen, D. C. Ralph, and R. A. Buhrman, "Magnetic switching by spin torque from the spin Hall effect." arXiv:1110.6846, 2011.
- [168] L. Liu, R. A. Buhrman, and D. C. Ralph, "Review and Analysis of Measurements of the Spin Hall Effect in Platinum," *ArXiv e-prints*, Nov. 2011.
- [169] K. Ando, S. Takahashi, K. Harii, K. Sasage, J. Ieda, S. Maekawa, and E. Saitoh, "Electric manipulation of spin relaxation using the spin hall effect," *Physical Review Letters*, vol. 101, p. 036601, Jul 2008.
- [170] T. Kimura, Y. Otani, T. Sato, S. Takahashi, and S. Maekawa, "Room-temperature reversible spin Hall effect," *Physical Review Letters*, vol. 98, p. 156601, Apr 2007.
- [171] O. Mosendz, J. E. Pearson, F. Y. Fradin, G. E. W. Bauer, S. D. Bader, and A. Hoffmann, "Quantifying spin Hall angles from spin pumping: Experiments and theory," *Physical Review Letters*, vol. 104, p. 046601, Jan 2010.
- [172] L. Liu, T. Moriyama, D. C. Ralph, and R. A. Buhrman, "Spin-torque ferromagnetic resonance induced by the spin Hall effect," *Physical Review Letters*, vol. 106, p. 036601, Jan 2011.
- [173] L. Liu, C.-F. Pai, Y. Li, H. W. Tseng, D. C. Ralph, and R. A. Buhrman, "Spin-torque switching with the giant spin Hall effect of tantalum," *Science*, vol. 336, no. 6081, pp. 555–558, 2012.
- [174] Y. Niimi, M. Morota, D. H. Wei, C. Deranlot, M. Basletic, A. Hamzic, A. Fert, and Y. Otani, "Extrinsic spin Hall effect induced by iridium impurities in copper," *Physical Review Letters*, vol. 106, p. 126601, Mar 2011.

- [175] S. V. Morozov, K. S. Novoselov, M. I. Katsnelson, F. Schedin, L. A. Ponomarenko, D. Jiang, and A. K. Geim, "Strong suppression of weak localization in graphene," *Physical Review Letters*, vol. 97, p. 016801, Jul 2006.
- [176] Y.-F. Chen, M.-H. Bae, C. Chialvo, T. Dirks, A. Bezryadin, and N. Mason, "Magnetoresistance in single-layer graphene: weak localization and universal conductance fluctuation studies," *Journal of Physics: Condensed Matter*, vol. 22, no. 20, p. 205301, 2010.
- [177] C. Beenakker and H. van Houten, "Quantum transport in semiconductor nanostructures," in *Semiconductor Heterostructures and Nanostructures* (H. Ehrenreich and D. Turnbull, eds.), vol. 44 of *Solid State Physics*, pp. 1 – 228, Academic Press, 1991.
- [178] A. A. Kaverzin, A. S. Mayorov, A. Shytov, and D. W. Horsell, "Impurities as a source of $1/f$ noise in graphene," *Physical Review B*, vol. 85, p. 075435, Feb 2012.
- [179] G. Xu, C. M. Torres, Y. Zhang, F. Liu, E. B. Song, M. Wang, Y. Zhou, C. Zeng, and K. L. Wang, "Effect of spatial charge inhomogeneity on $1/f$ noise behavior in graphene," *Nano Letters*, vol. 10, no. 9, pp. 3312–3317, 2010.
- [180] A. Mayorov, "Tunnelling and noise in gaas and graphene nanostructures," Master's thesis, University of Exeter, 2008.
- [181] D. A. Abanin, S. V. Morozov, L. A. Ponomarenko, R. V. Gorbachev, A. S. Mayorov, M. I. Katsnelson, K. Watanabe, T. Taniguchi, K. S. Novoselov, L. S. Levitov, and A. K. Geim, "Giant nonlocality near the dirac point in graphene," *Science*, vol. 332, no. 6027, pp. 328–330, 2011.